

Observation of $b \rightarrow d\gamma$ decays and determination of

$$|V_{td}/V_{ts}|$$

Debabrata Mohapatra

Dissertation submitted to the Faculty of the
Virginia Polytechnic Institute and State University
in partial fulfilment of the requirements of the degree of
Doctor of Philosophy in Physics

Leo Pilonen, chair

John Ficenec

Tetsuro Mizutani

Mark Pitt

John Simonetti

Blacksburg, Virginia

CKM matrix elements, rare B decays, radiative B decays

June 19, 2006

Observation of $b \rightarrow d\gamma$ decays and determination of $|V_{td}/V_{ts}|$

Debabrata Mohapatra

Abstract

The flavor changing neutral current process $b \rightarrow d\gamma$ is a sensitive probe to the Standard Model of elementary particle physics. Using a sample of 386×10^6 B meson pairs accumulated by the Belle detector at the KEKB e^+e^- collider, we measure the branching fractions for the exclusive modes $B^- \rightarrow \rho^-\gamma$, $\bar{B}^0 \rightarrow \rho^0\gamma$ and $\bar{B}^0 \rightarrow \omega\gamma$ as follows:

$$\mathcal{B}(B^- \rightarrow \rho^-\gamma) = 0.55^{+0.42+0.09}_{-0.36-0.08}$$

$$\mathcal{B}(\bar{B}^0 \rightarrow \rho^0\gamma) = 1.25^{+0.37+0.07}_{-0.33-0.06}$$

$$\mathcal{B}(\bar{B}^0 \rightarrow \omega\gamma) = 0.56^{+0.34+0.05}_{-0.27-0.10}$$

where the first error on each value is statistical and the second is systematic. Assuming that these three modes are related by isospin conservation rules, we find the combined branching fraction

$$\mathcal{B}(\bar{B} \rightarrow (\rho, \omega)\gamma) = 1.32^{+0.34+0.10}_{-0.31-0.09}.$$

This result is used to determine the ratio of CKM matrix elements,

$$|V_{td}/V_{ts}| = 0.199^{+0.026+0.018}_{-0.025-0.015}.$$

Acknowledgments

I am thankful to all members of Belle Collaboration and KEKB for their cooperation. It was a pleasure to meet and work with all the talented and interesting individuals in the KLM and DCPV groups. The analysis presented in this thesis builds on, and incorporates the work and guidance of many. Among them are Mikihiro Nakao, Nishida Shohei, H.W Kim, Bruce Yabsley, Tom Browder, Steve Olsen, Karim Trabelsi, Alan Schwartz, Alex Bondar, J. Haba, Masako Iwasaki, F. Ronga, Y. Sakai, K. Abe, Gobinda Majumder, Osamu Tajima and Paoti Chang.

I thank my advisor, Professor Leo Piilonen, for his kind and patience guidance. He gave me a solid foundation in the experimental physics as well as providing me with an opportunity to participate in a cutting edge high energy physics experiment.

I would like to express deep gratitude to Professor Mikihiro Nakao, who took care my research work at High Energy Accelerator Organization (KEK).

During my KEK years, I enjoyed friendship with Manmohan, Tapas, Asish, Sanjay, Seema, Kazi, Jan, Tagir, Alexy, Nick, Tim, Nitesh and Garima. I would like to thank Belle secretaries Chihiro Imai, Miyuki Hatogai and Atsuko Naka for their support during my long stay at KEK.

My friend Chris deserves special mention for her support during my years at Virginia Tech. Finally, I thank my parents for their love and support, and Manpreet for her patience, love and understanding.

Contents

Abstract	ii
Acknowledgements	iii
Contents	iv
List of Figures	vii
List of Tables	x
1 Introduction	1
1.1 Flavor Physics	1
1.2 Radiative B decays	3
2 The Belle Experiment	5
2.1 The $\Upsilon(4S)$	5
2.2 History of the Belle experiment	7
2.3 The KEKB Accelerator	9
2.4 The Belle Detector	11
2.4.1 Beam Pipe	14
2.4.2 Extreme Forward Calorimeter (EFC)	15
2.4.3 Silicon Vertex Detector (SVD)	16

2.4.4	Central Drift Chamber (CDC)	22
2.4.5	Aerogel Čerenkov Counter (ACC)	23
2.4.6	Time of Flight Scintillator (TOF)	27
2.4.7	Electromagnetic Calorimeter (ECL)	29
2.4.8	Solenoid Magnet	32
2.4.9	K_L and Muon Detector (KLM)	33
2.5	Trigger and Data Acquisition	35
2.5.1	The Level-1 (L1) trigger	37
2.5.2	Level-3 (L3) and Level-4 (L4) Triggers	39
2.5.3	Data Acquisition (DAQ)	40
2.5.4	Data Processing	42
2.6	Software	43
2.6.1	Monte Carlo Generation	44
3	Signal Reconstruction and Background Suppression	46
3.1	Overview of the analysis	46
3.1.1	Data set	47
3.1.2	Hadronic event selection	47
3.1.3	Photon Reconstruction	48
3.1.4	Neutral pion reconstruction	48
3.1.5	Charged pion reconstruction	49
3.1.6	Reconstruction of ρ , ω and K^*	50
3.1.7	Reconstruction of B candidate	50
3.2	Background	52
3.2.1	Continuum Background	52

3.2.2	$\bar{B} \rightarrow \bar{K}^*\gamma$ Background	60
3.2.3	Other $B \rightarrow X_s\gamma$ background	62
3.2.4	$B \rightarrow V\pi^0$ and $B \rightarrow V\eta$	62
3.2.5	Other Rare B Decays	62
3.2.6	Generic B Decays	63
3.2.7	Other $b \rightarrow d\gamma$ Component	63
3.2.8	Off-timing Bhabha Overlaid with Another Event	64
3.3	Analysis Optimization	64
4	Fit Results and Systematic Errors	69
4.1	Signal Modeling	69
4.2	Signal Efficiency	70
4.3	Fitting	72
4.3.1	Fit parameters	73
4.4	Results	75
4.4.1	Fit results	75
4.4.2	Systematic errors	77
4.4.3	Significance calculation	78
4.4.4	Plots for mass and helicity angle	80
5	Physics Results and Conclusion	96
5.1	Extraction of $ V_{td}/V_{ts} $	96
5.2	Conclusion	98
A	Isospin Violation	99
A.0.1	Significance of the Isospin Violation	99

A.0.2	Probability of the Isospin Violation from Toy MC Study	100
A.0.3	Possible Bias in the Fitting Code	101

List of Figures

1.1	CKM Unitarity triangle.	3
1.2	(a) Loop diagram for $b \rightarrow d\gamma$ and (b) annihilation diagram.	4
2.1	e^+e^- total cross section	6
2.2	KEKB luminosity history.	9
2.3	KEKB e^+e^- collider configuration.	10
2.4	Cut away view of the Belle detector	13
2.5	Side view of the Belle detector	14
2.6	Configuration of beam pipe	15
2.7	EFC configuration	16
2.8	EFC rates and the beam current during beam injection	17
2.9	Configuration of SVD1	18
2.10	Double-sided silicon-strip detector from the SVD	19
2.11	Impact parameter resolution of charged tracks with associated SVD hits.	20
2.12	Sideview of the SVD2 geometry.	21
2.13	Frontview of the SVD2: A typical hadronic hit.	21
2.14	Configuration of CDC.	24

2.15	CDC cell structure.	24
2.16	CDC p_t resolution	25
2.17	dE/dx distribution versus momentum.	26
2.18	Alignment of ACC.	27
2.19	Schematic drawing for typical ACC module	28
2.20	Hadron mass distributions calculated from TOF measurements	30
2.21	TOF Configuration.	31
2.22	ECL configuration	32
2.23	Mechanical structure of the ECL counter.	33
2.24	Energy (left) and position (right) resolutions of the ECL.	34
2.25	Superconducting coil.	35
2.26	The barrel and end-cap RPC.	36
2.27	An overview of the Belle trigger system.	40
2.28	Belle level one (L1) trigger.	41
2.29	Belle data acquisition system.	42
3.1	Distributions for (a) E_γ^* , (b) $\cos\theta_\gamma$ and (c) E_9/E_{25}	49
3.2	Distributions for invariant masses of ρ^- , ρ^0 and ω mesons	51
3.3	Distributions for beam constraint mass (M_{bc}) and Energy difference (ΔE).	51
3.4	Distributions for Event-shape, $\cos\theta_B$, vertex separation Δz and Likelihood Ratio	59
3.5	Quality of B flavor tag	59
3.6	Distributions for M_{bc} and ΔE for continuum background	60
3.7	Distributions for ΔE and K_π for $K^*\gamma$ background	61
4.1	Fit results for $\overline{B}^0 \rightarrow \overline{K}^{*0}\gamma$	83

4.2	Fit results for $B^+ \rightarrow K^{*+}\gamma$	84
4.3	Projection to the signal slice of the individual fit results for the $B^- \rightarrow \rho^- \gamma$, $\bar{B}^0 \rightarrow \rho^0 \gamma$ and $\bar{B}^0 \rightarrow \omega \gamma$ modes	88
4.4	Projection to the fit region of the individual fit results for the $B^- \rightarrow \rho^- \gamma$, $\bar{B}^0 \rightarrow \rho^0 \gamma$ and $\bar{B}^0 \rightarrow \omega \gamma$ modes	89
4.5	Projection to the signal slice of the simultaneous fit results to the five modes.	90
4.6	Fit likelihood distribution	94
4.7	Mass and helicity angle distributions for the individual fit results to the $B^- \rightarrow \rho^- \gamma$, $\bar{B}^0 \rightarrow \rho^0 \gamma$ and $\bar{B}^0 \rightarrow \omega \gamma$ modes.	95
5.1	Limits on $\bar{\rho}$ and $\bar{\eta}$	97
A.1	Toy MC distribution of the fit results for the branching fraction (upper) and error (lower).	103
A.2	Toy MC distribution of the simultaneous fit results for the samples selected from the individual fit results.	104
A.3	Contours of equal probability points that are away from the nominal value (0, 0) by 0.5, 1, 1.5, 2 and 2.5σ . Note that the PAW contour of 2σ does not somehow directly go through the measured (β, γ) point (red point).	104

List of Tables

2.1	Experiment numbers and integrated luminosity.	8
2.2	Main parameters of KEKB.	12
2.3	Polar angle coverage of the Belle detector.	13
2.4	Number of detectors in each half ladder of the SVD.	22
2.5	Geometrical configuration of the ECL.	30
2.6	Examples of event classification.	43
3.1	Summary of the MC samples for signal and background.	66
3.2	Requirement on \mathcal{R} for each $q \cdot r$ bin.	67
3.3	Summary of particle selection criteria.	68
4.1	MC signal ΔE shape parameters.	81
4.2	Summary of the signal shape parameters.	82
4.3	Summary of efficiency systematic errors.	85
4.4	Summary of corrections on the particle identification efficiencies and total efficiencies including the systematic errors in Table 4.3.	85
4.5	Signal yields in the wide region (Numbers in the parenthesis are for the signal box) from the individual fits and the simultaneous fit.	86

4.6	Signal yields, efficiency, branching fraction and significance.	87
4.7	Fitting systematic errors on ΔE and M_{bc} signal modeling.	91
4.8	Fitting systematic errors on B backgrounds.	92
4.9	Fitting systematic errors on efficiencies and the total systematic errors. . .	93
4.10	Significance calculations.	94
A.1	Summary of the toy MC results.	103

Chapter 1

Introduction

The Standard Model (SM) is the current theory of fundamental particles and their interactions. These fundamental particles are categorized into three generations of spin-1/2 fermions, and the interactions between them are mediated by spin-1 bosons. The SM has been successful in explaining physical phenomena such as strong, electromagnetic and weak interactions, but not gravity. All experimental results to date are consistent with the SM. But, as we all suspect, the SM is not the complete and final theory: it contains many ad hoc numbers (such as fermion masses) and puzzling phenomena (such as the presence of only left-handed weak interactions). Thus, we expect to see and we look for—evidence of new physics beyond the Standard Model.

1.1 Flavor Physics

In the Standard Model, the complex phases of the 3×3 Kobayashi-Maskawa (KM) quark mixing matrix are the source of CP violation at the electroweak scale and have their origin in the quark mass matrix of the Yukawa sector of the theory. The study of CP violation

and measurements of the KM matrix elements, including the complex phases, are very important for the development of a more fundamental understanding of nature.

In the KM model, CP violation is attributed to complex phases in the quark mixing matrix

$$\begin{pmatrix} V_{ud} & V_{us} & V_{ub} \\ V_{cd} & V_{cs} & V_{cb} \\ V_{td} & V_{ts} & V_{tb} \end{pmatrix}. \quad (1.1)$$

The nontrivial complex phases are typically assigned to the furthest off-diagonal elements V_{ub} and V_{td} . Unitarity of the KM matrix implies that $\sum_i V_{ij}^* V_{ik} = \delta_{jk}$ and $\sum_j V_{ij}^* V_{kj} = \delta_{ik}$, which gives the following relation involving V_{ub} and V_{td} :

$$V_{td}V_{tb}^* + V_{cd}V_{cb}^* + V_{ud}V_{ub}^* = 0. \quad (1.2)$$

This expression implies that the three terms form a closed triangle in the complex plane, as shown in Fig. 1.1. The three internal angles of this so-called ‘‘unitarity triangle’’ are defined as

$$\phi_1 \equiv \arg\left(\frac{V_{cd}V_{cb}^*}{V_{td}V_{tb}^*}\right), \quad \phi_2 \equiv \arg\left(\frac{V_{ud}V_{ub}^*}{V_{td}V_{tb}^*}\right), \quad \phi_3 \equiv \arg\left(\frac{V_{cd}V_{cb}^*}{V_{ud}V_{ub}^*}\right). \quad (1.3)$$

Wolfenstein suggested a rather convenient approximate parameterization of the KM matrix [2],

$$\begin{pmatrix} 1 - \lambda^2/2 & \lambda & \lambda^3 A(\rho - i\eta) \\ -\lambda & 1 - \lambda^2/2 & \lambda^2 A \\ \lambda^3 A(1 - \rho - i\eta) & -\lambda^2 A & 1 \end{pmatrix}, \quad (1.4)$$

where there are four parameters, λ , A , ρ , and η , that have to be obtained from experiment. Of the four, λ and A are relatively well determined; less is known about ρ and η .

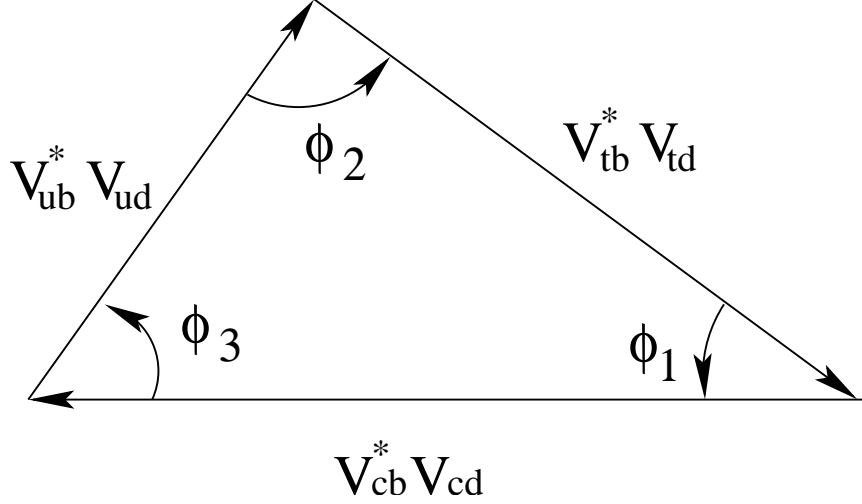


Figure 1.1: CKM Unitarity triangle.

1.2 Radiative B decays

The radiative transitions $b \rightarrow s\gamma$ and $b \rightarrow d\gamma$ are among the most valuable probes of flavour physics. The Cabibbo-favoured $b \rightarrow s\gamma$ modes belong to the small number of rare decays that are experimentally accessible at present. The $b \rightarrow d\gamma$ process, which proceeds via a loop diagram (Fig. 1.2(a)) in the SM, is suppressed with respect to $b \rightarrow s\gamma$ by the KM factor [1] $|V_{td}/V_{ts}|^2 \sim 0.04$, with large uncertainty due to the lack of precise knowledge of $|V_{td}|$. The corresponding exclusive modes $\bar{B} \rightarrow \rho\gamma$ and $\bar{B}^0 \rightarrow \omega\gamma$ are presumably the easiest modes to search for; no evidence for these decays has been previously reported [5, 6].

The predicted branching fractions are $(0.9-2.7) \times 10^{-6}$ [8, 9, 11] based on the measured rate for the $b \rightarrow s\gamma$ process $\bar{B} \rightarrow \bar{K}^*\gamma$ and the $|V_{td}/V_{ts}|^2$ factor with corrections due to form factors, $SU(3)$ breaking effects, and, for the B^- decay, inclusion of an annihilation diagram

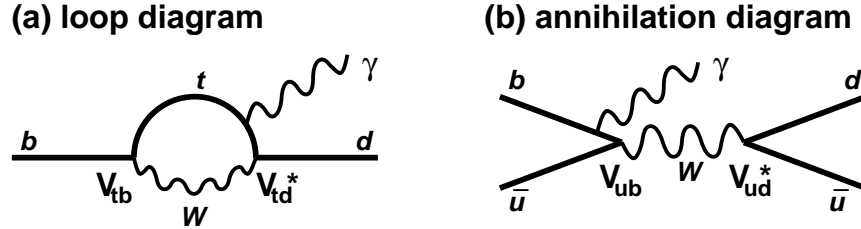


Figure 1.2: (a) Loop diagram for $b \rightarrow d\gamma$ and (b) annihilation diagram.

(Fig. 1.2(b)).

Measurement of these exclusive branching fractions allows one to determine the value of $|V_{td}/V_{ts}|$ in the context of the SM and to search for physics beyond the SM [14].

If one assumes the $|V_{td}|$ value from a fit to the unitarity triangle, one can use the decay to search for new physics effects in the branching fraction, in direct and time-dependent CP violation and in isospin asymmetry. Although we know various $b \rightarrow s\gamma$ observables are in very good agreement with the SM, large new physics effects may show up in $b \rightarrow d\gamma$ in which both SM and new physics amplitudes and phases naturally differ from those of the $b \rightarrow s\gamma$ transition.

In this dissertation, we report the first observation of the $b \rightarrow d\gamma$ process using a sample of $(386 \pm 5) \times 10^6$ B meson pairs accumulated at the $\Upsilon(4S)$ resonance.

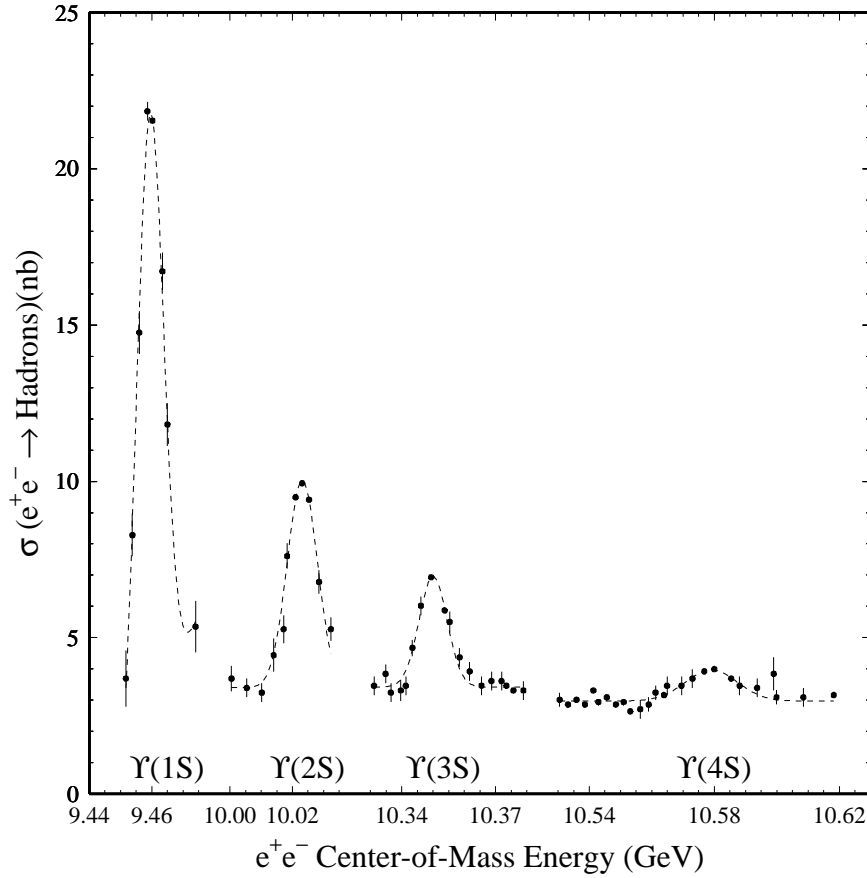
Chapter 2

The Belle Experiment

2.1 The $\Upsilon(4S)$

The Υ mesons are bound states of $b\bar{b}$ quarks with spin, parity and charge conjugation quantum numbers $J^{PC} = 1^{--}$. After the first observation of the $\Upsilon(1S)$ in proton-nucleon collisions by the CFS collaboration, the existence of the Υ meson was confirmed by experiments at CESR [17] and DORIS [18]. Fig. 2.1 shows the total e^+e^- annihilation cross section as a function of the CM energy in the region of the Υ resonances measured by CLEO [19].

The mass of the $\Upsilon(4S)$ meson is just above the threshold for decay into $B\bar{B}$ meson pairs, where B refers generically to a bound state of either $\bar{b}u$ or $\bar{b}d$ quarks. It decays about 96% of the time into such $B\bar{B}$ pairs [19]. The cross section of $\Upsilon(4S)$ production at its peak position is about 1/3 of that of total hadronic production ($e^+e^- \rightarrow q\bar{q}$ ($q = u, d, s, c$)), which is often referred to as “continuum”. Therefore, although KEKB is operating at the $\Upsilon(4S)$ resonance to produce $B\bar{B}$ pairs, it produces three times more $q\bar{q}$ events that constitute a major source of background to B physics. Due to the low invariant mass of the $q\bar{q}$ pair, the

Figure 2.1: e^+e^- total cross section

jets from these light quarks are produced with a significant boost factor. In contrast, the B and \bar{B} mesons from $\Upsilon(4S)$ decay are generated nearly at rest, and so have a more spherical event structure. We will use this difference later to suppress continuum events with so-called shape variables. In order to study the $q\bar{q}$ contribution cleanly, KEKB is sometimes operated at 60 MeV below the $\Upsilon(4S)$ resonance. The data taken at the $\Upsilon(4S)$ resonance and 60 MeV below are referred to as “on-resonance” and “off-resonance” respectively. Around 10% of data taken by Belle are off-resonance. The ratio of the branching fraction of $\Upsilon(4S)$ to $B^0\bar{B}^0$

and $B^+ B^-$ has also been measured by CLEO [19] and is:

$$\frac{\mathcal{B}(\Upsilon(4S) \rightarrow B^+ B^-)}{\mathcal{B}(\Upsilon(4S) \rightarrow B^0 \bar{B}^0)} = 1.04 \pm 0.07 \pm 0.04, \quad (2.1)$$

which is consistent with equal production rates for charged and neutral $B\bar{B}$ pairs. Here we follow the Particle Data Group (PDG) convention, which assumes an equal production rate [3].

2.2 History of the Belle experiment

The Belle experiment started at KEK in Tsukuba, Japan, in 1994. The construction of KEKB was completed in 1998. After half a year of KEKB commissioning, the Belle detector was installed in the beam line in May 1999. Physics runs started in June 1999. Physics runs are divided into “experiments.” The period and accumulated luminosity for each experiment upto April 2005 are listed in Table 2.1. The accumulated luminosity and peak luminosity of KEKB are shown in Fig. 2.2; as you can see, the daily measures (top three graphs) continue to rise, indicating continuous improvement in the operation of the accelerator. In May 2005, KEKB achieved the world record of the peak luminosity of $15.81 \times 10^{33} \text{ cm}^{-2}\text{s}^{-1}$ and up to June 12, 2006, KEKB accumulated a record integrated luminosity of 612 fb^{-1} . Today, about 1 fb^{-1} of data is taken every day.

The main physics goal of Belle is to study CP violation in the B meson system. Additionally, Belle has made significant achievements in charm, τ , and two photon physics, as well as non- CP aspects of B physics.

Table 2.1: Experiment numbers and integrated luminosity.

ExpNo	Integrated luminosity (fb ⁻¹)			
	On resonance	Continuum	Energy scan	Total
3	0.02	0.002	0.009	0.03
5	0.24	0.019	—	0.26
7	5.86	0.589	0.084	6.53
9	4.38	—	—	4.38
11	8.32	1.216	0.124	9.66
13	10.8	1.209	0.065	12.1
15	12.8	1.412	—	14.2
17	12.1	0.848	—	12.9
19	29.1	3.645	—	32.7
21	4.41	—	—	4.41
23	6.30	1.449	—	7.75
25	25.9	1.675	—	27.8
27	25.6	3.755	—	29.4
29	—	—	—	—
31	18.1	2.425	—	20.5
33	17.7	2.734	—	20.4
35	16.8	1.959	—	18.7
37	62.6	6.091	—	68.7
39	50.3	—	—	50.3
41	64.9	—	—	64.9
Total	376.2	29.03	0.283	405.6

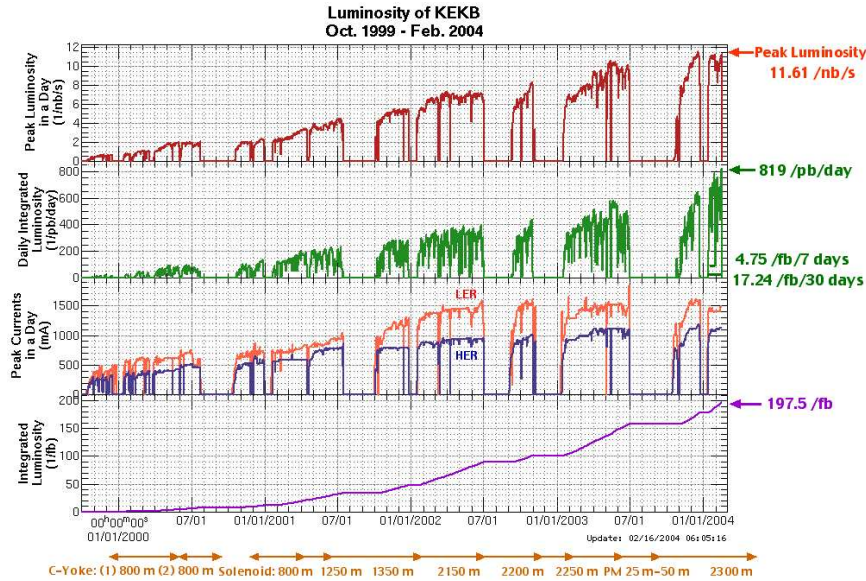
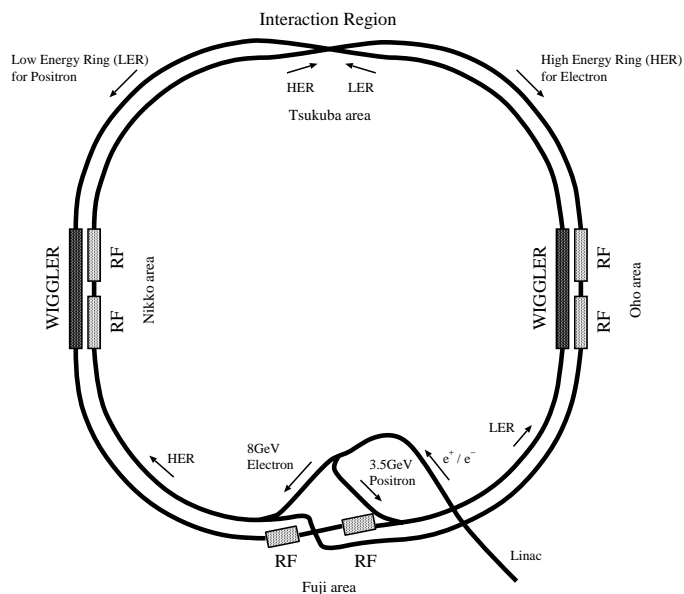


Figure 2.2: KEKB luminosity history.

2.3 The KEKB Accelerator

The KEKB colliding-beam accelerator provides the electron-positron collisions at the heart of the Belle detector. It consists of two storage rings of 3.012 km length each, one for the 8 GeV electrons (High Energy Ring, HER) and one for the 3.5 GeV positrons (Low Energy Ring, LER), that were constructed inside the tunnel of the decommissioned TRISTAN accelerator. The rings are positioned 11 m underground. Since the two beams have different energies, separate beam pipes are used. To ensure that the circumference of each ring is precisely the same, a second cross-over of the two beam pipes occurs in the Fuji area. The configuration of the KEKB storage ring is illustrated in Fig. 2.3. The electron and positron beams are created and accelerated to their final energy in the linear accelerator (Linac) and then injected into KEKB in the Fuji area. The two beams cross at the interaction point (IP)

Figure 2.3: KEKB e^+e^- collider configuration.

in the Tsukuba experimental hall at the center of the Belle detector [16]. At the IP, electrons and positrons collide with a finite crossing angle of ± 11 mrad. In order to compensate for the energy loss of the beams due to radiation as they circulate in KEKB, two kinds of RF cavities—normal conductive cavities called Accelerator Resonantly coupled with Energy Storage (ARES) and superconducting cavities (SCC)—are installed. The positron beam passes through wigglers that are installed in order to reduce the longitudinal damping time of the LER.

KEKB was designed to achieve a luminosity \mathcal{L} of $10^{34} \text{ cm}^{-2}\text{s}^{-1}$ based on the formula:

$$\mathcal{L} = \frac{1}{2er_e} \xi_y \left(\frac{\gamma I}{\beta_y^*} \right)_{\pm} = (2.2 \times 10^{-34}) \xi_y \left(\frac{IE}{\beta_y^*} \right)_{\pm}, \quad (2.2)$$

where e is the elementary electric charge, r_e is the classical electron radius, ξ_y is the vertical beam tune shift parameter, β_y^* is the vertical β function at the IP, γ is the Lorentz boost

factor, I is the beam current and E is the beam energy. The units of L , I , E and β_y^* are given in $\text{cm}^{-2}\text{s}^{-1}$, A, GeV and cm respectively. We assume that β_y^* and ξ_y are the same for both beams, because unequal parameters cause incomplete overlap of both the beams during the collision. This assumption requires $I_+E_+ = I_-E_-$, so the LER current is higher than the HER current. The design parameters of KEKB are listed in Table 2.2.

2.4 The Belle Detector

The Belle detector is a general purpose detector surrounding the interaction point (IP) to detect the particles from e^+e^- collisions. In order to study the B meson and other related physics at KEKB, the Belle detector consists of a beam pipe, Extreme Forward Calorimeter (EFC), Silicon Vertex Detector (SVD), Central Drift Chamber (CDC), Aerogel Čerenkov Counter (ACC), Time of Flight Counter (TOF), Electromagnetic Calorimeter (ECL), solenoid magnet, K_L and Muon detector (KLM), trigger and Data Acquisition system (DAQ), and off-line software and computing facilities. We define the right-handed coordinate system for Belle by aligning the z -axis with the positron beam and its positive direction opposite the motion of the positrons. The y -axis points upwards and the x -axis is perpendicular to both (pointing away from the center of the KEKB rings). The polar angle θ is measured relative to the positive z -axis. Due to the boost of the $\Upsilon(4S)$ resonances, the components of Belle are asymmetrical in z . This is apparent in Fig. 2.4 and 2.5, where the components are shifted towards the forward direction relative to interaction point (IP). The detector is divided into three regions: the barrel section, which is parallel to the beam axis, and the two endcaps, which extend radially from the beam axis at the forward and backward ends of the detector. The polar angle coverage of each of the three sections is shown in Table 2.3.

Table 2.2: Main parameters of KEKB.

Ring		LER	HER	Unit
Energy	E	3.5	8.0	GeV
Circumference	C	3016.26		m
Luminosity	\mathcal{L}	1×10^{34}		$\text{cm}^{-2}\text{s}^{-1}$
Crossing angle	θ_x	± 11		mrad
Tune shifts	ξ_x/ξ_y	0.039/0.052		m
Beta function at IP	β_x^*/β_y^*	0.33/0.01		
Beam current	I	2.6	1.1	A
Natural bunch length	σ_z	0.4		cm
Energy spread	σ_E	7.1×10^{-4}	6.7×10^{-4}	
Bunch spacing	s_B	0.59		m
Particle/bunch	N	3.3×10^{10}	1.4×10^{10}	
Emittance	ϵ_x/ϵ_y	$1.8 \times 10^{-8}/3.6 \times 10^{-10}$		m
Synchrotron tune	ν_s	0.01~0.02		
Betatron tune	ν_x/ν_y	45.52/45.08	47.52/46.08	
Momentum compaction factor	α_p	$1 \times 10^{-4} \sim 2 \times 10^{-4}$		
Energy loss/turn	U_0	0.81†/1.5‡	3.5	MeV
RF voltage	V_c	5~10	10~20	MV
RF frequency	f_{RF}	508.887		MHz
Harmonic number	h	5120		
Longitudinal damping time	τ_ϵ	43†/23‡	23	ms
Total beam power	P_b	2.7†/4.5‡	4.0	MW
Radiation power	P_{SR}	2.1†/4.0‡	3.8	MW
HOM power	P_{HOM}	0.57	0.15	MW
Bending radius	ρ	16.3	104.5	m
Length of bending	l_b	0.915	5.86	m

†: without wigglers, ‡ with wigglers.

Table 2.3: Polar angle coverage of the Belle detector.

Region	Polar angle coverage
Barrel	$34^\circ < \theta < 127^\circ$
Forward endcap	$17^\circ < \theta < 34^\circ$
Backward endcap	$127^\circ < \theta < 150^\circ$

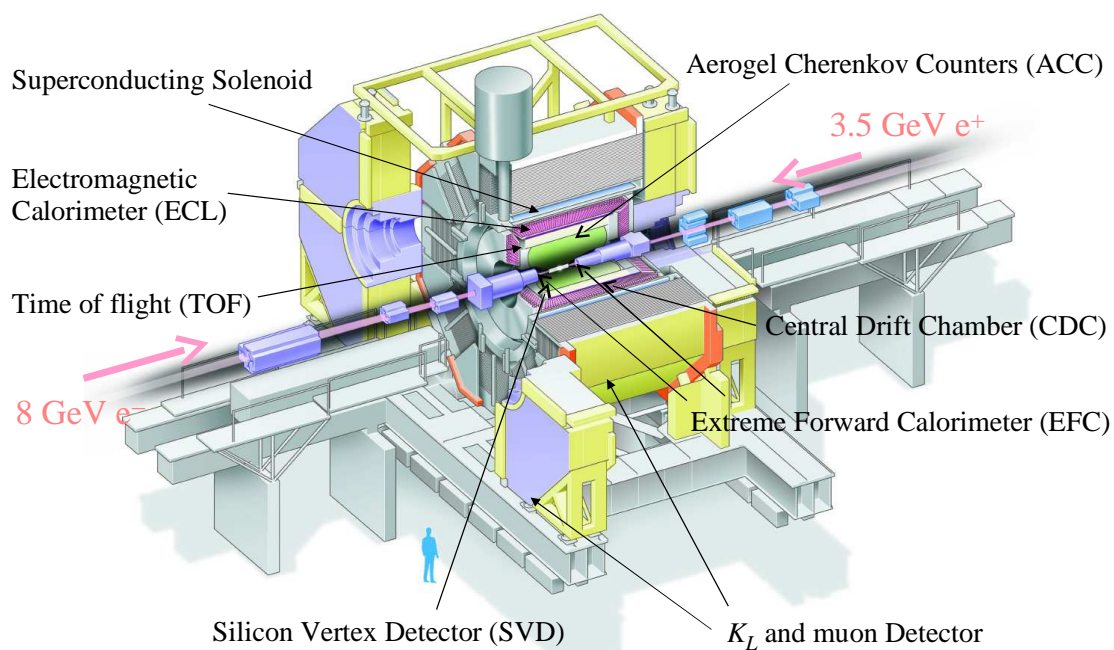


Figure 2.4: Cut away view of the Belle detector

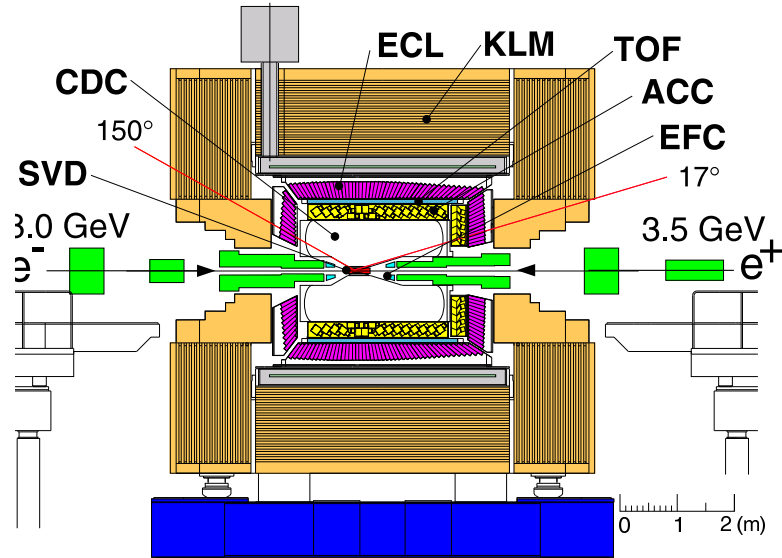


Figure 2.5: Side view of the Belle detector

Following is a brief description of the components of the Belle detector.

2.4.1 Beam Pipe

The beam pipe is designed to minimize multiple scattering and energy loss of charged particles between their production and their measurement in the SVD and CDC, since these effects degrade the vertex resolution. The beam pipe configuration is shown in Fig. 2.6. It consists of two beryllium cylinders, with radii 20.0 mm and 23.0 mm, and with 0.5 mm thickness for each. The 2.5 mm gap between cylinders is filled with helium gas for cooling. (The beam-pipe is heated by ohmic currents and high order mode losses in the material as the beam bunches circulate.) The outer beryllium cylinder is covered with a 20 μm thick gold film to absorb low energy X-rays from the HER. The total material thickness of the

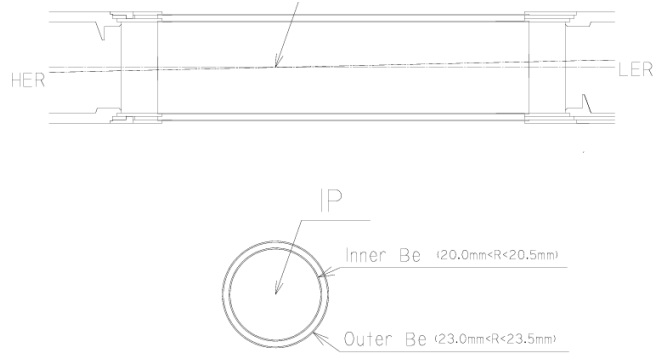


Figure 2.6: Configuration of beam pipe

beam pipe corresponds to 0.9% of a radiation length.

2.4.2 Extreme Forward Calorimeter (EFC)

The extreme forward calorimeter is designed to extend the polar angle coverage for the Belle detector. Photons and electrons are measured by the EFC in the extreme forward and backward area that is not covered by the ECL (see section 2.4.7). The EFC is placed around the beam pipe close to the IP, where a very high radiation level exists. The radiation-hard crystal bismuth germanate (BGO), $\text{Bi}_4\text{Ge}_3\text{O}_{12}$, is used as the scintillating material, and a photodiode is used to read out the signal. The EFC covers the polar angle range $6.4^\circ < \theta < 11.5^\circ$ for the forward detector and $163.3^\circ < \theta < 171.2^\circ$ for the backward detector. Both forward and backward detectors are segmented into 32 sections in ϕ and 5 in θ . Figure 2.7 shows the EFC configuration. The forward and backward crystals correspond to 12 and 11 radiation lengths respectively. The EFC is also used for online luminosity monitoring based on the rate of Bhabha scattering mechanism. Figure 2.8 shows the history of a typical beam fill in the early days of operation. The real Bhabha rate is

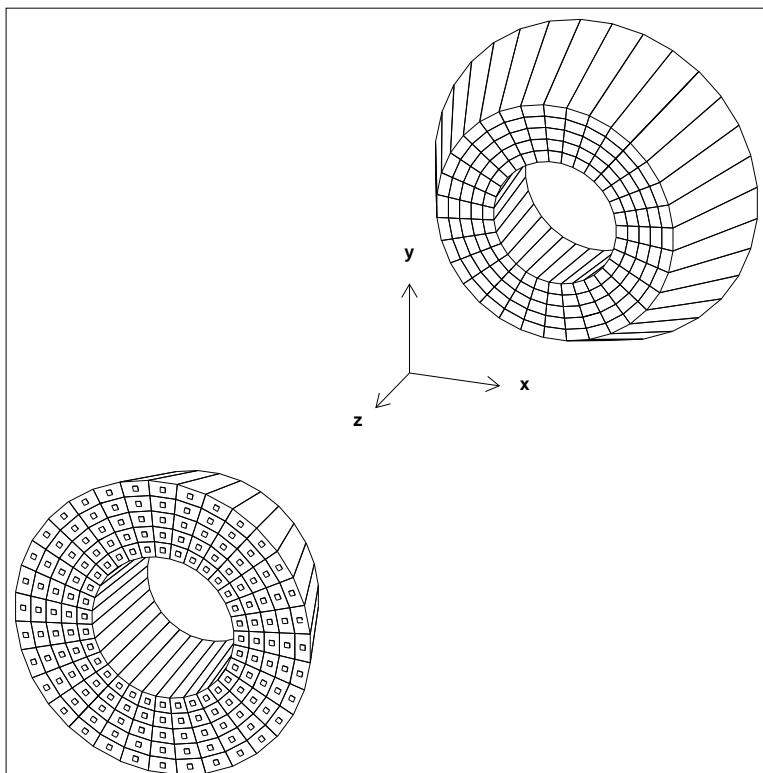


Figure 2.7: EFC configuration

calculated by subtracting the EFC fake rate ($< 10\%$) from the EFC raw Bhabha rate.

2.4.3 Silicon Vertex Detector (SVD)

The primary purpose of the SVD is to determine the z -axis position of the B meson decay vertex, which is essential for time-dependent CP analysis. Figure 2.9 shows the configuration of the original SVD in a side and end view perspective. It has three layers of double-sided silicon strip detectors (DSSD) and covers the region of $23^\circ < \theta < 139^\circ$, corresponding to 86% of the total solid angle. As shown in the end view, the three layers consist of 8, 10 and 14 full ladders respectively for the inner, middle and outer layers around the

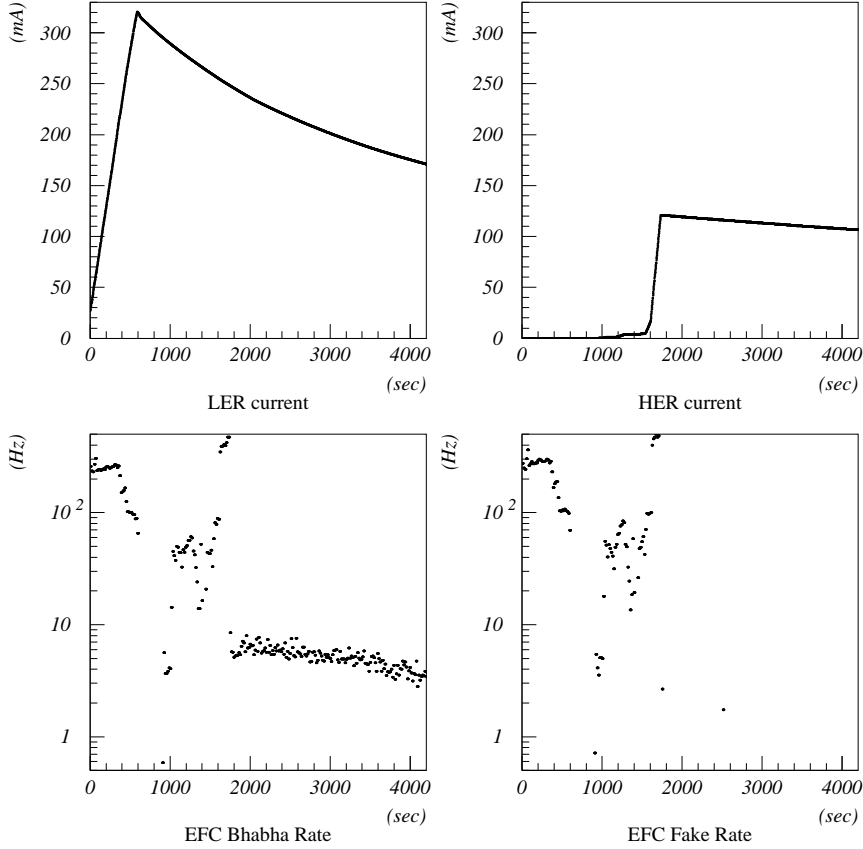


Figure 2.8: EFC rates and the beam current during beam injection

beam axis. Each full ladder is made of two half-ladders and each half-ladder contains one or two DSSDs which are supported by boron-nitride (BN) ribs sandwiched with carbon-fiber reinforced plastic (CFRP). In total, there are 32 ladders and 102 DSSDs. The DSSDs are essentially reverse-biased diode-strip detectors. They are produced by Hamamatsu Photonics and were originally designed for the DELPHI micro-vertex detector [20]. They are $300 \mu\text{m}$

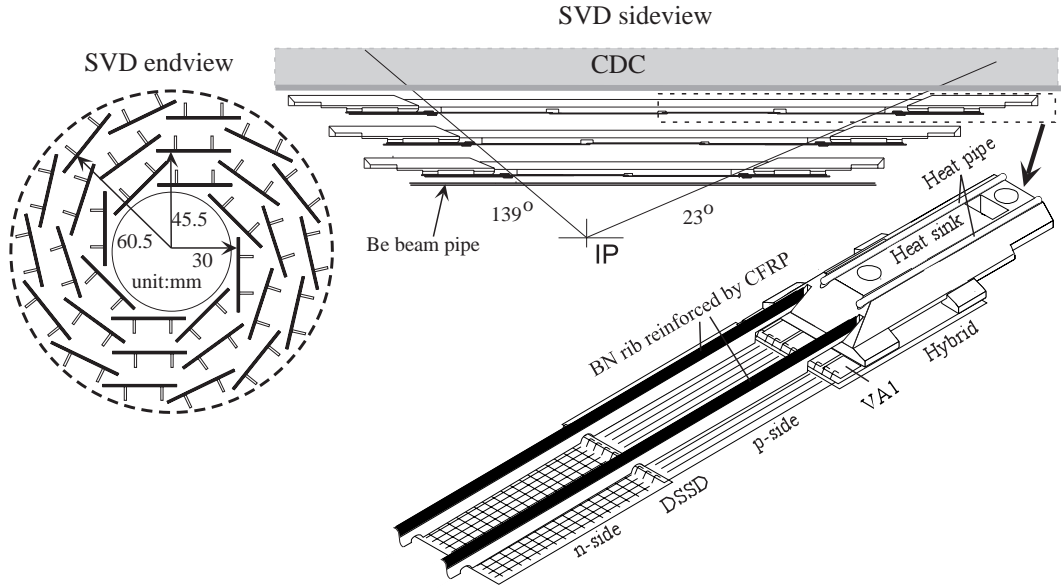


Figure 2.9: Configuration of SVD1

thick and have an area of $57.5 \times 33.5 \text{ mm}^2$. Each DSSD contains 1280 sense strips and 640 readout pads. One side is p doped silicon with p^+ readout strips parallel to the beam to measure ϕ . The other side has n^+ strips oriented perpendicular to the beam to measure the z coordinate. The p^+ and n^+ strips have pitches of $24 \mu\text{m}$ and $42 \mu\text{m}$, respectively. As shown in Fig. 2.10, a charged particle traversing a DSSD will create electron-hole pairs, which will drift to the appropriately biased side of the DSSD, where their charge is deposited and read out. The signals from the DSSDs are read out by VA1 chips [21] mounted on a ceramic hybrid. As the VA1 has 128 channels, five chips are mounted on each hybrid to read out all 640 pads on a DSSD. The VA1 chips are fabricated with a $1.2 \mu\text{m}$ CMOS process by Austrian Micro Systems and can tolerate radiation levels of up to 200 krad. Signals from the VA1 chips are digitized by flash analogue-to-digital converters (FADCs), which are located in the adjacent Belle electronics hut. Online digital signal processors in

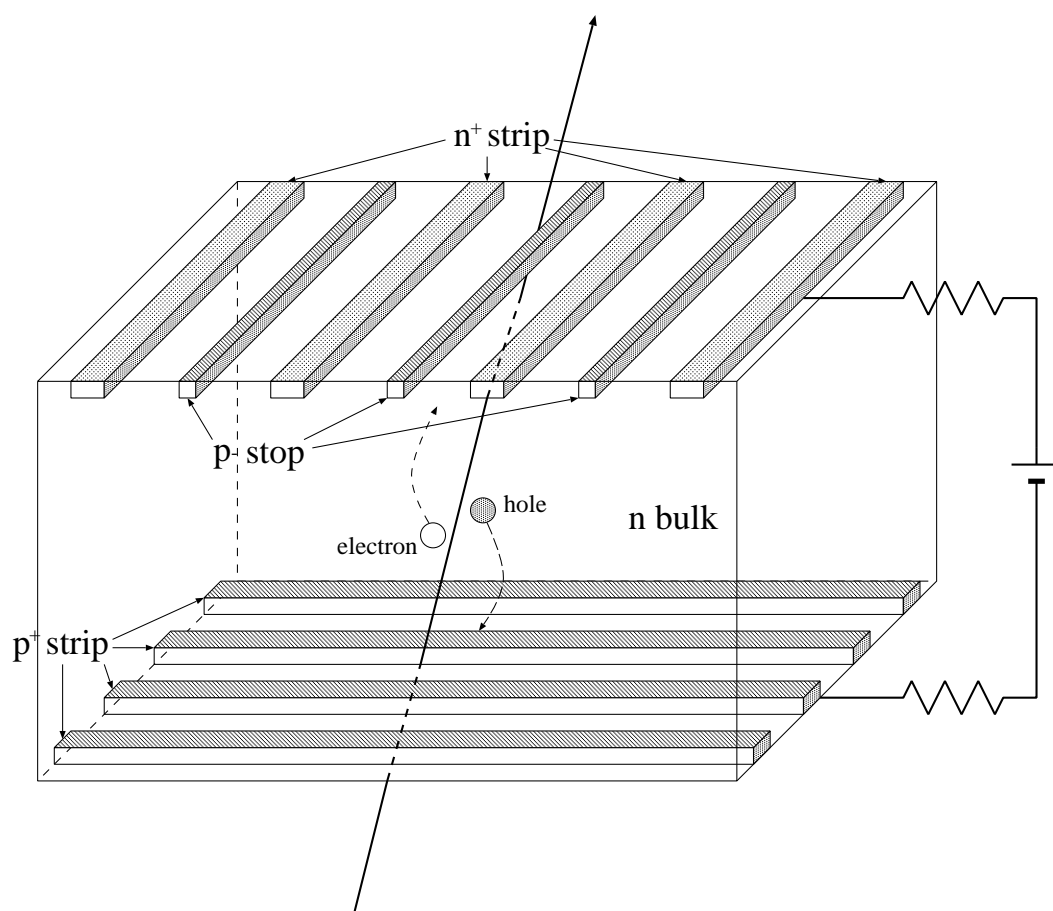


Figure 2.10: Double-sided silicon-strip detector from the SVD

the FADC modules perform common mode noise subtraction, data sparsification and data formatting. As mentioned before, the main purpose of the SVD is to determine the B meson decay vertex and to improve the charged tracking. For studies of time dependent CP asymmetries, the z -axis distance of the two B vertices for an $\Upsilon(4S)$ decay must be measured with the precision of about $100 \mu\text{m}$. As shown in Fig. 2.11, the momentum and angular dependences of the impact parameter (the closest approach of tracks to the IP)

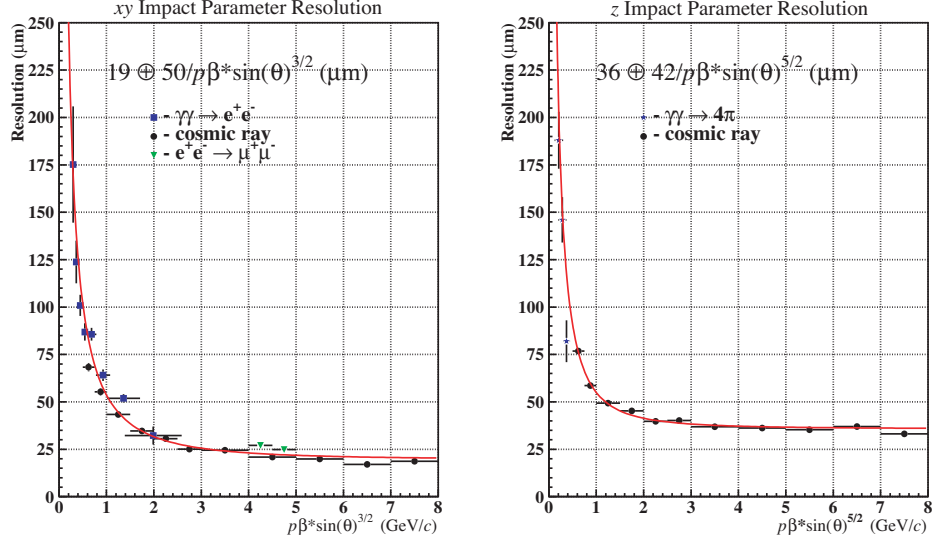


Figure 2.11: Impact parameter resolution of charged tracks with associated SVD hits.

resolution behave like:

$$\sigma_{xy} = 19 \oplus 50(p\beta \sin^{3/2} \theta)^{-1} \mu\text{m} \text{ and} \quad (2.3)$$

$$\sigma_z = 36 \oplus 42(p\beta \sin^{5/2} \theta)^{-1} \mu\text{m}, \quad (2.4)$$

where \oplus indicates a quadratic sum. The momentum p is given in units of GeV/c . The impact parameter resolution for a 1 GeV track is around $55 \mu\text{m}$. In summer 2004, the three-layer SVD1 was replaced with a four-layer SVD2. Several improvements were made. SVD2 has a larger angular acceptance of $17^\circ < \theta < 150^\circ$. The innermost layer is closer to the primary interaction point at a distance of 2 cm instead of 3 cm in SVD1. This is possible with a significantly smaller beam pipe. The fourth layer is accommodated by a redesign of inner region of the CDC (see section 2.4.4). The four layers of SVD2 contains 6, 12, 18 and 18 full ladders from inside to outside as shown in Fig. 2.12. Each half ladder consist of 1, 2 or 3 DSSDs. The DSSDs for SVD2 have 512 readout channels in both $r - z$

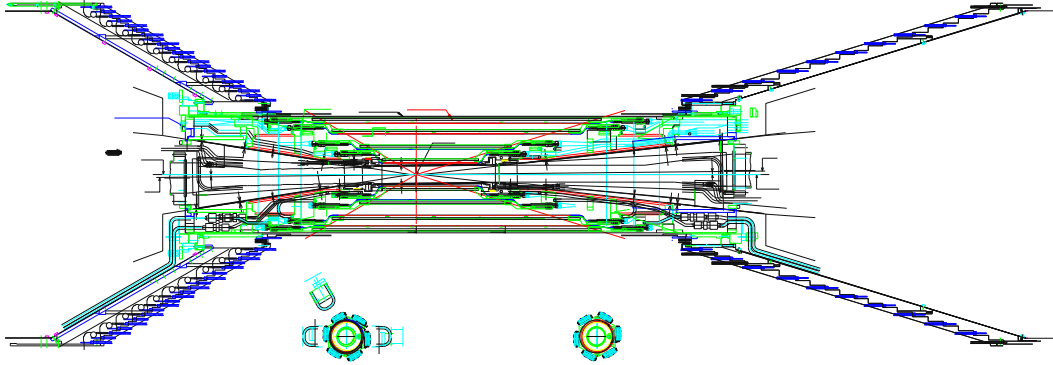


Figure 2.12: Sideview of the SVD2 geometry.

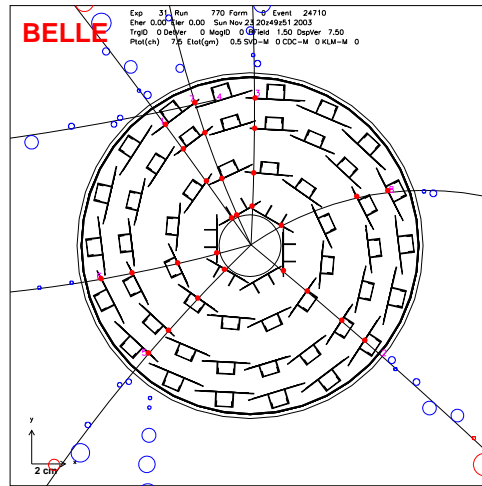


Figure 2.13: Frontview of the SVD2: A typical hadronic hit.

and $r - \phi$, or in total 110,592 readout channels. The number of DSSDs for each half ladder is displayed in Table 2.4. A hadronic event recorded by SVD2 is displayed in Fig. 2.13. For the SVD1, the limited radiation tolerance of the VA1 front-end readout chip was an important issue. It was replaced by a VA1TA chip [22], manufactured by IDEAS. It is implemented in a $0.25 \mu\text{m}$ CMOS process and is expected to have a stable performance up

Table 2.4: Number of detectors in each half ladder of the SVD.

number of DSSDs in	forward	/	backward	half ladder
Layer 1:	1		1	
Layer 2:	1		2	
Layer 3:	2		3	
Layer 4:	3		3	

to a radiation dose of at least 20 MRad [23]. More information on SVD1 and SVD2 can be found in Refs. [16, 24, 25].

2.4.4 Central Drift Chamber (CDC)

The main purpose of the CDC is to measure the momentum and the energy deposition of charged particles (dE/dx). The dE/dx information is used to provide information for particle identification (PID), i.e. identifying kaons, pions, protons and electrons. All components in Belle out to the ECL (described in section 2.4.7) are contained in a 1.5 T magnetic field supplied by a solenoid magnet (see section 2.4.8). The field is nearly uniform and directed in the positive z direction. When a charged particle moves through a magnetic field, it follows a helical path along the field direction. The helix can be decoupled into a circular motion in a plane, being defined by three parameters, and a motion in a straight line, being defined by two parameters. From these five independent parameters it is possible to determine the closest approach of the helix to the IP and the components of the particle's momentum parallel and perpendicular to the magnetic field. These momentum and impact parameter measurements are the primary purpose of the CDC. Figure 2.14 shows the CDC structure. The length of CDC is 2,400 mm, and the inner and outer radii are 83 and 874

mm, respectively. It covers the polar angle range from 17° to 150° . The CDC is a small cell drift chamber consisting of 50 anode sense wire layers and three cathode strip layers. The 50 anode layers consist of 32 axial wire layers and 18 small-angle stereo wire layers. The axial wires are parallel to the z direction and the crossing angles between the stereo wires and z -axis vary from 42.5 mrad to 72.1 mrad. There are 8,400 readout channels for the anode wires and 1792 channels for the cathode strips. The cell configuration is shown in Fig. 2.15. We obtain three-dimensional track information from the anode wires. As well as tracking, the CDC provides a vital component to the particle identification (PID) system. From the pulse height at the anode wires, a measure of the mean energy deposition due to ionization of the gas (dE/dx) can be obtained for a particle traversing the CDC. As the energy loss depends on the boost of the particle, for a given momentum, dE/dx will depend on particle species. A 50% helium-50% ethane mixed gas fills the chamber to minimize the multiple Coulomb scattering contribution. The pulse height and drift time of the ionization are measured to provide the information of energy deposit and the distance from the sensor-wire. The transverse momentum (p_t) resolution is shown in Fig. 2.16; the resolution is a function of p_t itself behaving like $(0.19p_t \oplus 0.30)\%$. The dE/dx resolution is 7.8% for pions from K_s decay and 6% for energetic electrons and muons. The scattering distribution for dE/dx is shown at Fig. 2.17. The separation between the different particles can clearly be seen. The separation between kaons and pions is of relevance for this analysis. The CDC is described in [16, 26] in more detail.

2.4.5 Aerogel Čerenkov Counter (ACC)

The aerogel Čerenkov counter is designed for K^\pm and π^\pm separation with momentum between 1.2 GeV/c and 3.5 GeV/c. The ACC detects the Čerenkov light emitted when a particle travels through a medium faster than the speed of light in that medium. Specif-

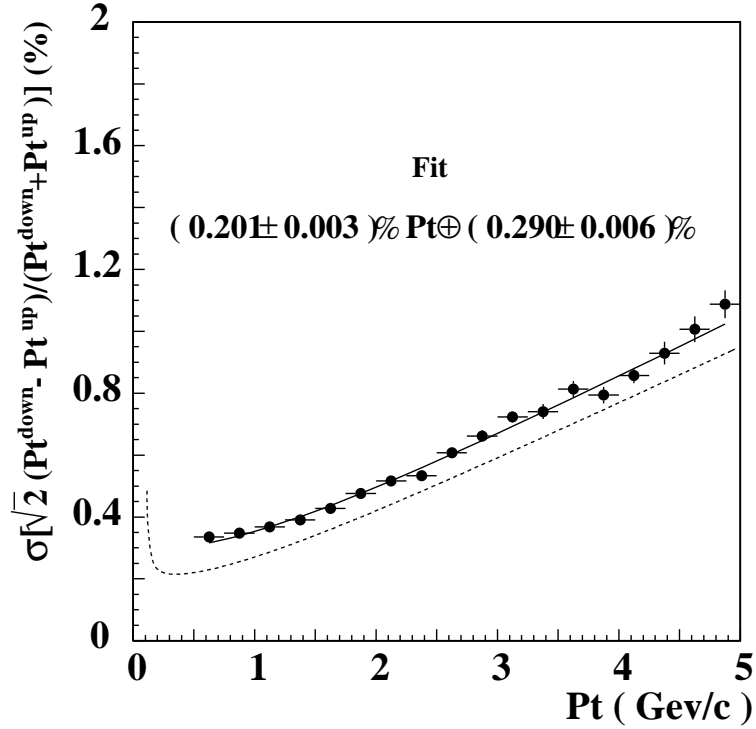


Figure 2.16: The CDC p_t resolution. The solid curve is the fitted result and the dotted curve is the ideal expectation for $\beta = 1$ charged track.

ically, for a medium of refractive index n , Čerenkov light is emitted if the velocity of the particle, β , satisfies:

$$n > 1/\beta = \sqrt{1 + (mc/p)^2}, \quad (2.5)$$

where m and p are the mass and momentum of the particle, respectively. Thus, depending on the refractive index of the medium, there will be a range of velocity for which pions emit Čerenkov radiation but kaons do not. The barrel ACC consists of 960 aerogel counter modules segmented into 60 cells in ϕ direction. The forward end-cap ACC consists of 228 modules that are arranged in 5 concentric layers. There are five different types of aerogel

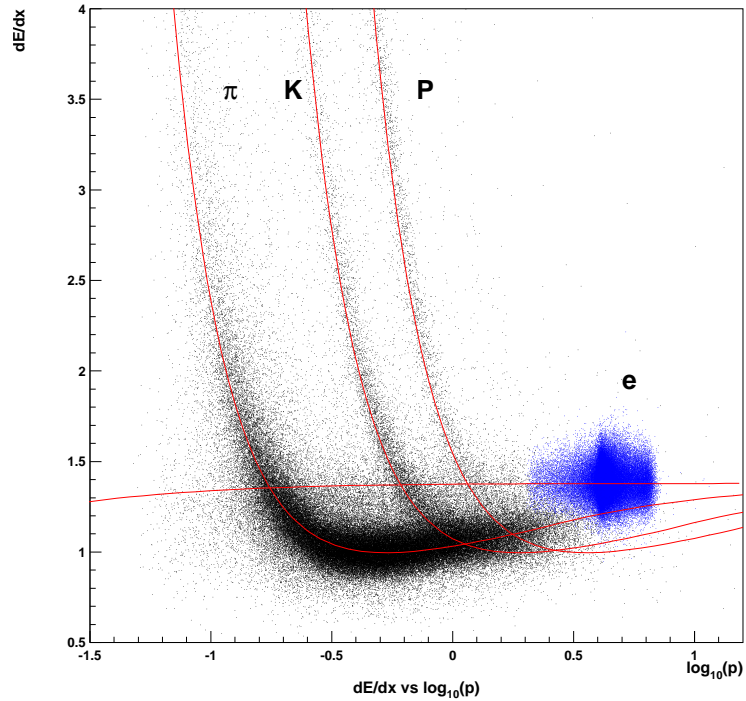


Figure 2.17: dE/dx distribution versus momentum.

with refractive indices of $n = 1.010, 1.013, 1.015, 1.020$ and 1.028 , arranged according to polar angle. The alignment is shown in Fig. 2.18. The typical counter module consists of silica aerogel filled in 0.2 mm-thick aluminum boxes and viewed with one or two fine mesh-type photomultiplier tubes (FM-PMTs). The FM-PMTs can be operated well in a 1.5T magnetic field. Figure 2.19 shows a schematic drawing of the ACC module. There are 1560 readout channels in the barrel part and 228 in end-cap. A more detailed description of the ACC can be found in Reference [27].

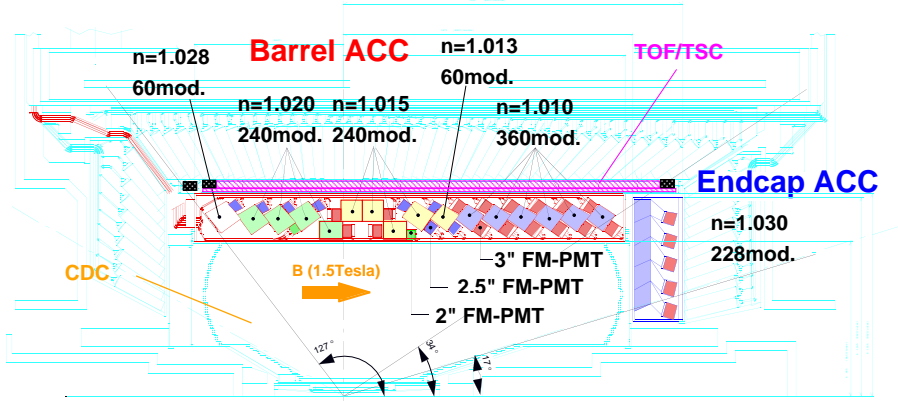


Figure 2.18: Alignment of ACC.

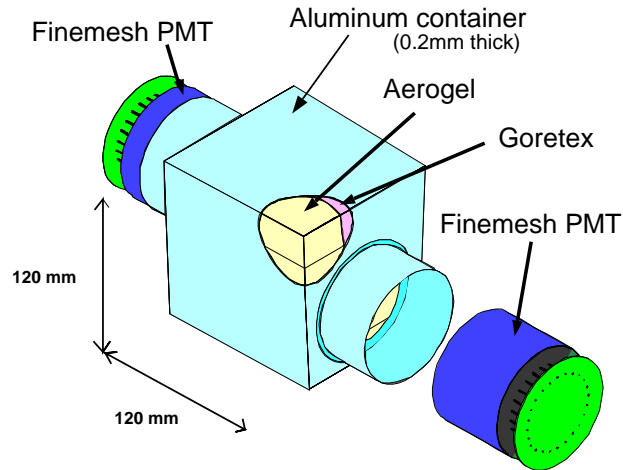
2.4.6 Time of Flight Scintillator (TOF)

The time of flight detector provides complementary information for the particle identification in the ACC in order to distinguish K^\pm and π^\pm mesons up to 1.2 GeV/c, where the K/π separation power for ACC and CDC is less effective. The TOF also provides fast timing signals for the trigger system, which requires a timing resolution of 100 ps. The flight time, T , for a particle of mass m to travel a length L is given by:

$$T = \frac{L}{c} \sqrt{1 + \left(\frac{mc}{p}\right)^2}. \quad (2.6)$$

The TOF measures the time elapsed between the collision at the IP and its passage through the TOF barrel. Thus a particle's mass can be calculated once its momentum is known. This enables particle species to be differentiated by their measured times-of-flight.

a) Barrel ACC Module



b) Endcap ACC Module

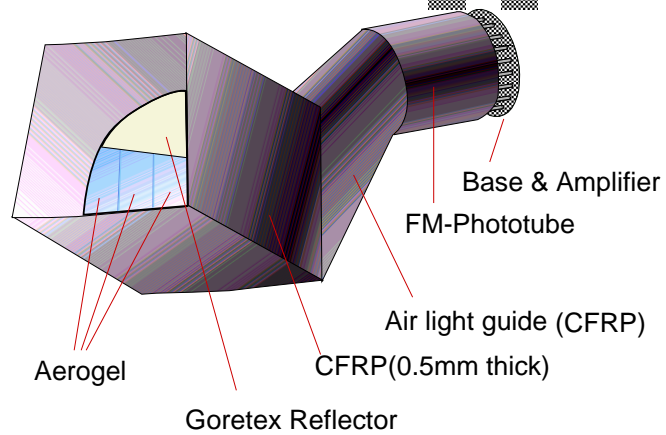


Figure 2.19: Schematic drawing for typical ACC module: (a) is the barrel ACC module and (b) is the forward end-cap module.

The mass distribution calculated from TOF measurements is shown in Fig. 2.20. Clear separation between kaons, pions and protons can be seen. The module TOF structure is shown in Fig. 2.21. TOF counters and TSCs are made of fast scintillators and FM-PMTs that are mounted directly to the scintillator. Two TOF counters (4 cm thick) and one TSC (0.5 cm thick) form one module. The TSC is used to produce trigger signals, taking a coincidence with the TOF counters to reduce the trigger hit rate. The TOF system consists of 64 TOF modules located in the barrel region just outside the ACC and covers the polar angle region $33^\circ < \theta < 121^\circ$. Each module is made up of two TOF counters, read out by two FM-PMTs attached at both ends, and one trigger scintillation counter (TSC), read out by one FM-PMT attached at the backward end. The time resolution of the TOF scintillators is $\sigma_t = 100$ ps. The TOF hit efficiency is 95% for single-end hits and 88% for both-end hits in $e^+e^- \rightarrow \mu^+\mu^-$ pair events. For more information on the TOF system, see Refs. [16, 28]. Information from the TOF combined with the ACC and the dE/dx measurement from the CDC give the Belle detector more than a 3σ separation between charged kaons and pions over the whole momentum range up to 3.5 GeV/c.

2.4.7 Electromagnetic Calorimeter (ECL)

The electromagnetic calorimeter (ECL) measures the energy and position of photons from π^0 decays and radiative B decays with high efficiency and good resolution for energy and position. The ECL is also used for electron identification. The ECL is composed of an array of tower-shaped CsI(Tl) crystals. Each crystal is arranged so that it points to the interaction point. (There is a small tilt angle so that photons do not pass through a gap between crystals without interacting.) Figure 2.22 and Table 2.5 shows the ECL configuration. The length of each crystal is 30 cm, which corresponds to 16.2 radiation lengths. Each crystal is read out by a pair of silicon PIN photodiodes. The energy resolution of the ECL is measured to

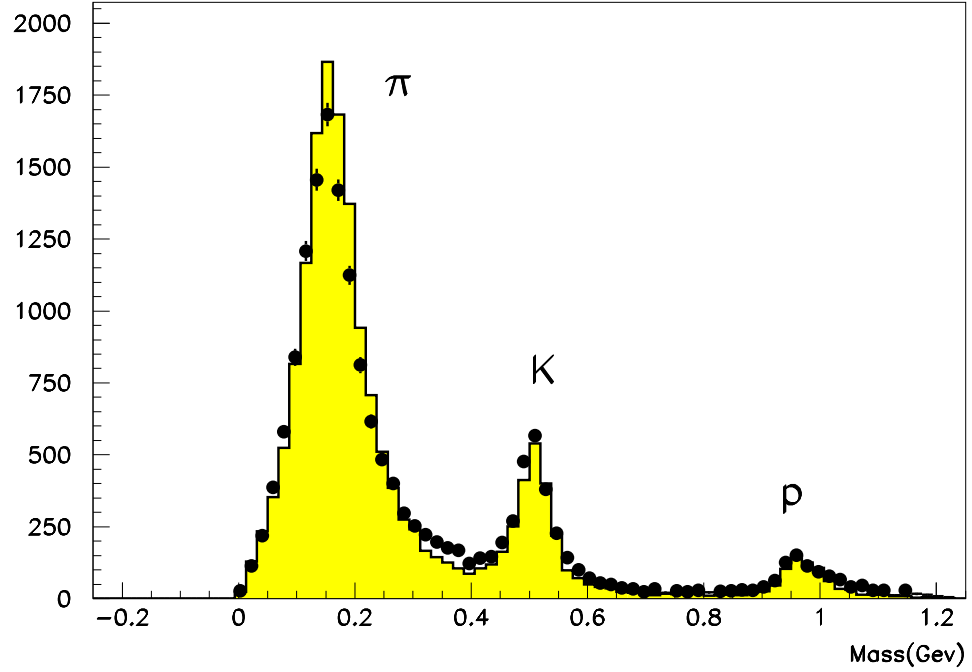


Figure 2.20: Hadron mass distributions calculated from TOF measurements for particles with momentum below 1.2 GeV/c. The points are from data, the shaded histogram is from Monte Carlo.

Table 2.5: Geometrical configuration of the ECL.

	θ coverage	θ seg.	ϕ seg.	#	Position
Forward endcap	$12.4^\circ < \theta < 31.4^\circ$	13	48 to 144	1152	$z = 196$ cm
Barrel	$32.2^\circ < \theta < 128.7^\circ$	46	144	6624	$r = 125$ cm
Backward endcap	$130.7^\circ < \theta < 155.1^\circ$	10	64 to 144	960	$z = 196$ cm
Total				8736	

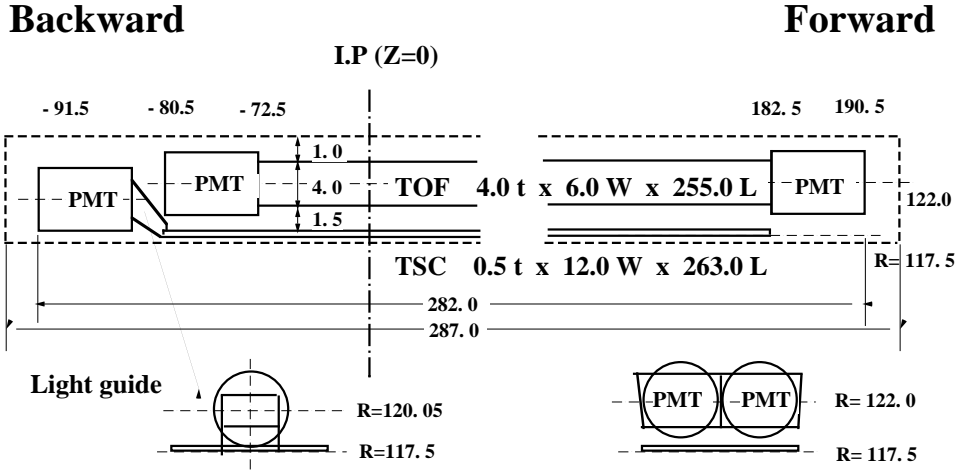


Figure 2.21: TOF Configuration.

be [29]:

$$\frac{\sigma_E}{E} = \frac{0.0066}{E} \oplus \frac{1.53}{E^{1/4}} \oplus 1.18(\%), \quad (2.7)$$

where the energy E is given in GeV. Here, the first term is from the contribution of the electronic noise, while the second term and part of the third term come from incomplete containment of the electromagnetic shower. The third term also includes systematic effects such as the uncertainty of the calibration of the light output from each crystals. The spatial resolution is found to be $0.27 \oplus 3.4/\sqrt{E} \oplus 1.8/E^{1/4}$ mm. The energy and position resolutions are shown in Fig. 2.24. In addition to the measurement of the energy of photons and electrons, the ECL plays an important role for electron identification: a charged track that points at an ECL cluster is identified as an electron (or positron) if the energy and momentum are consistent, among other criteria. The ECL also provides trigger information and online luminosity information [30]. The trigger system is described in section 2.5.

BELLE CsI ELECTROMAGNETIC CALORIMETER

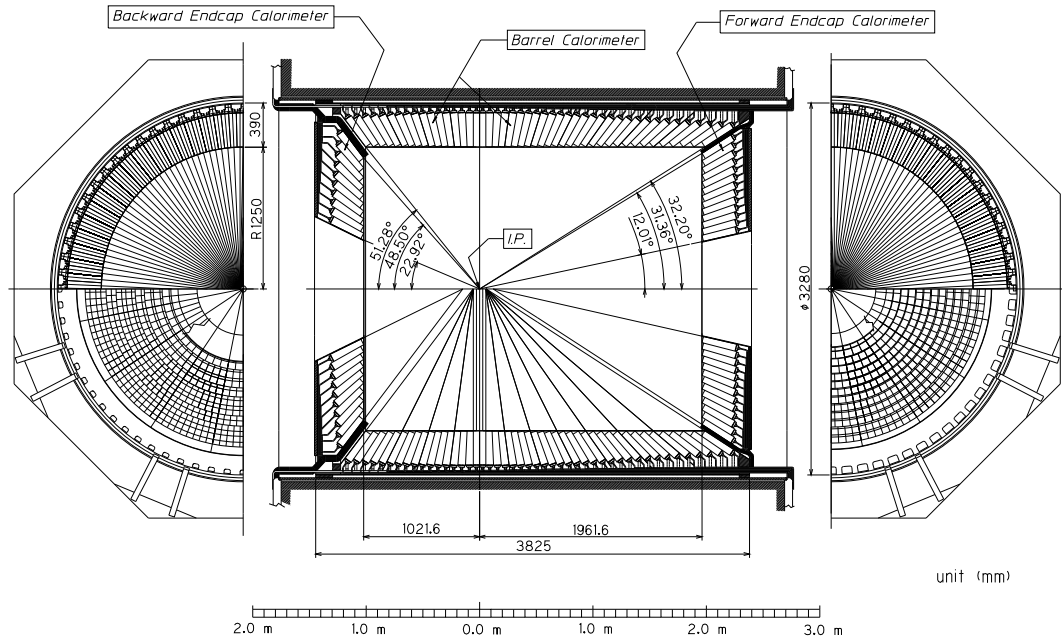


Figure 2.22: ECL configuration

2.4.8 Solenoid Magnet

The superconducting solenoid provides a 1.5 T magnetic field parallel to the beam pipe for charged particle momentum measurement. The superconducting coil consists of a single layer of niobium-titanium-copper alloy embedded in a high purity aluminum stabilizer. The coil is wound around the inner surface of an aluminum support cylinder of 3.4 m diameter and 4.4 m length. Indirect cooling is provided by a liquid helium circulation through a tube on the inner surface of the aluminum cylinder. The layout of the superconducting solenoid is shown in Fig. 2.25.

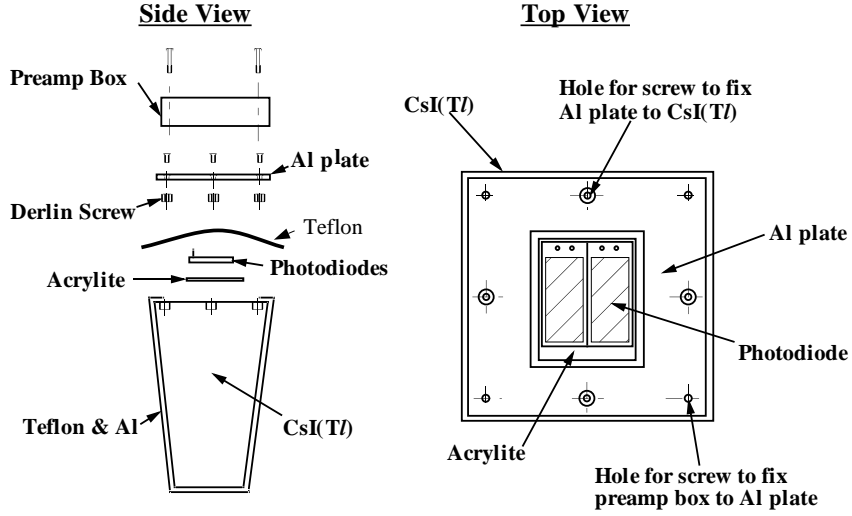


Figure 2.23: Mechanical structure of the ECL counter.

2.4.9 K_L and Muon Detector (KLM)

The K_L and muon detector (KLM) is designed for detection of K_L mesons and muons with momentum larger than 600 MeV/c. The detector is placed outside the solenoid and consists of 15 layers of Resistive Plate Counters (RPC) with 14 layers of 4.7 cm thick iron plates in the barrel region and 14 RPC layers in the endcap region. One RPC super-layer contains two RPC planes to provide θ and ϕ information. The iron plate is also used as return yoke for the magnetic field produced by the super conducting solenoid. The configuration of an RPC is shown in Fig. 2.26. The KLM covers the polar angle region of $20^\circ < \theta < 155^\circ$. Signals are read out from cathode strips in both θ and ϕ directions. There are 21,856 readout channels for the barrel detector and 16,126 for the two endcap detectors. The position resolution for K_L mesons is 30 mrad for both θ and ϕ and the time resolution is a few nanoseconds. All the material in the Belle detector up to the KLM corresponds to

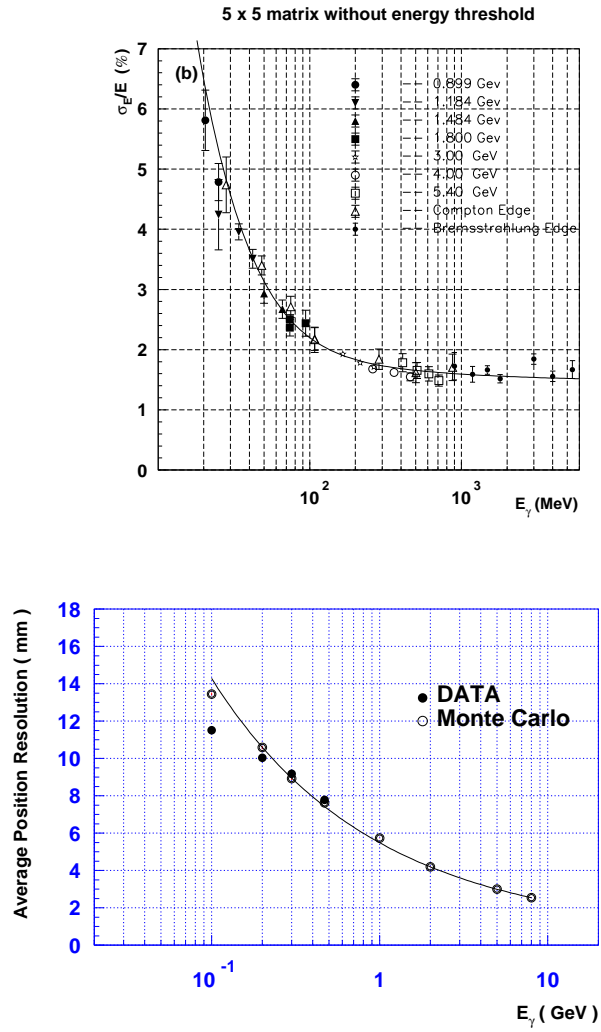


Figure 2.24: Energy (left) and position (right) resolutions of the ECL.

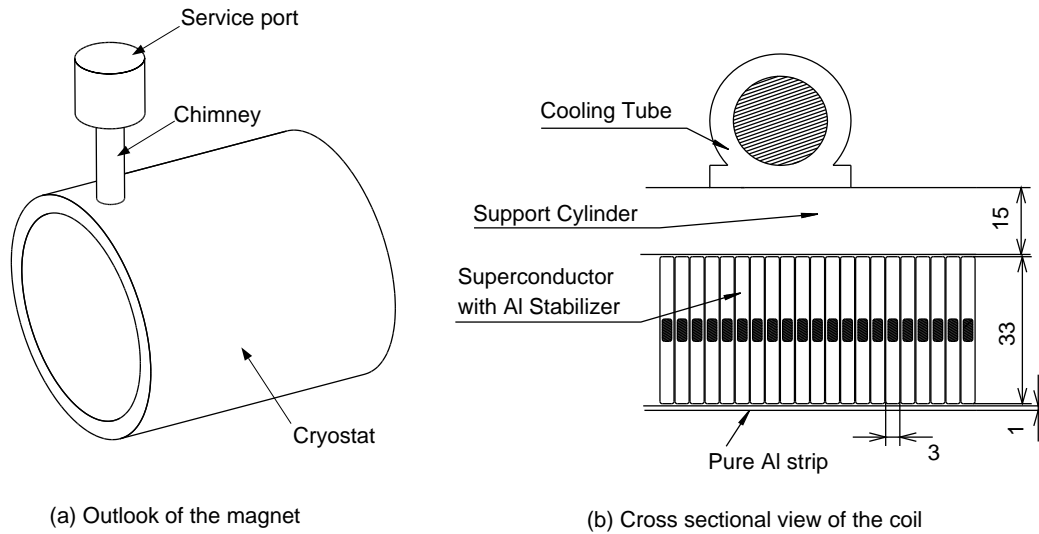


Figure 2.25: Superconducting coil.

about one hadronic interaction length for K_L mesons. The iron plates in the KLM provide a further 3.9 interaction lengths of material, which is necessary for detecting K_L mesons with high efficiency. When the K_L meson interacts with matter, it initiates a shower of hadrons, leaving a cluster of hits in the KLM that is not associated with a charged track. Muons can be discriminated from K_L mesons as they will have an associated charged track and a line of KLM hits rather than a shower pattern. For muons with a momentum of above 1 GeV/c or more, the KLM has a detection efficiency greater than 90% with a fake rate of about 2% (from non interacting pions and kaons).

2.5 Trigger and Data Acquisition

The role of the trigger is to decide when the various subsystems of the Belle detector should record an event. Once a particular particle collision satisfies the trigger criteria, data from

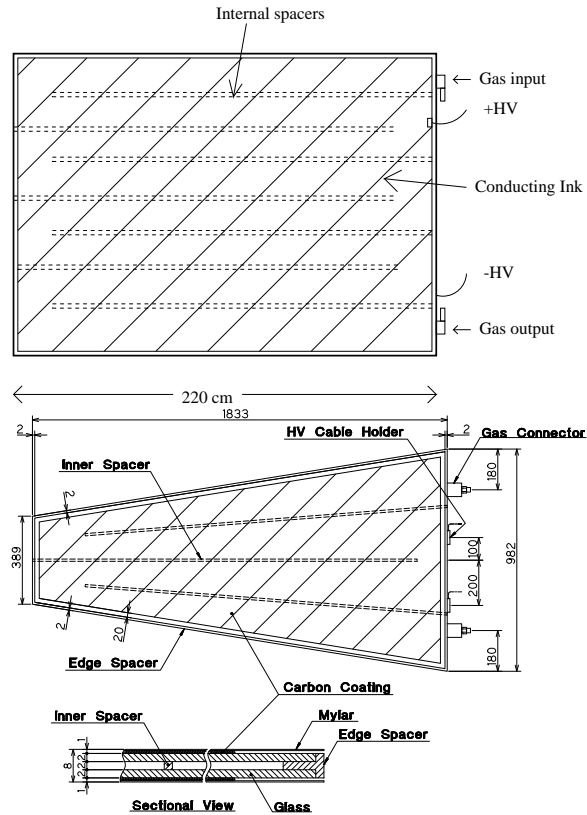


Figure 2.26: The barrel and end-cap RPC.

all the subsystems are read out and stored for possible use. The word *event* is used interchangeably to represent the physical particle collision or the stored data representing the collision. The decision to read out is based on criteria carefully chosen to remove background events while retaining events of interest at a high efficiency. Once an event is triggered, the data acquisition (DAQ) system transfers the raw data from the detector to the data storage system. The main sources of background events are undesirable interactions between the electron-positron beams, collisions of a beam particle with a residual gas molecule or with the beam-pipe, and synchrotron radiation from the beams. Events of interest are primar-

ily hadronic ($e^+e^- \rightarrow q\bar{q}$ or $e^+e^- \rightarrow \Upsilon(4S) \rightarrow B\bar{B}$) and QED events ($e^+e^- \rightarrow e^+e^-$ or $e^+e^- \rightarrow \mu^+\mu^-$ or $e^+e^- \rightarrow \tau^+\tau^-$), used for physics analyses as well as detector calibration and luminosity measurements. For this analysis only the hadronic events are of interest and thus the following discussion focuses on the hadronic trigger. Event rates for both physics and background events at the design luminosity of $10^{34} \text{ cm}^{-2}\text{s}^{-1}$ are about 100 Hz each; but to accommodate higher backgrounds, the trigger is designed to operate up to 500 Hz. Figure 2.27 shows an overview of the Belle trigger system. It consists of the level 1 hardware trigger, the level 3 software trigger implemented by an online computer farm and a level 4 trigger, which runs in the off-line Belle computing system and performs more elaborate background reduction based on full event reconstruction.

2.5.1 The Level-1 (L1) trigger

An overview of the level-1 trigger system is shown in Fig. 2.28. It consists of the sub-trigger system and the central trigger system called global decision logic (GDL) [31]. By design, all the subtrigger signals arrive at the GDL within $1.85 \mu\text{s}$ after the event occurs. The L1 final trigger signal is issued $2.2 \mu\text{s}$ after the event crossing. The timing of the trigger signals must be accurate since the trigger signal determines the readout timing. We determine the timing of the final trigger by the TOF trigger or, in its absence, the ECL trigger.

Sub-triggers

The GDL receives up to 48 subtrigger signals. As shown in Fig. 2.28, there are trigger signals from the CDC, TOF, ECL, KLM and EFC systems. Their trigger systems will only be mentioned very superficially here; for more information, see Ref. [35]. The CDC provides two types of triggers: the $r - \phi$ trigger and the z trigger [33]. The $r - \phi$ trigger is based on the signals from six axial super-layers, while the z trigger is formed by signals

from the cathode strips and z information inferred from the axial and stereo layers. The TOF produces trigger signals based on the hit multiplicity and back-to-back topology. The ECL trigger is based on trigger cells (TC) formed of 4×4 crystals combinations. It also provides triggers based on the $\theta - \phi$ segmentation, where the number of isolated cluster is calculated from the TC hit patterns. The KLM detects muons using four (two) layers in the barrel (endcap) parts and sends trigger signals to the GDL. The EFC provides two types of triggers: the EFC Bhabha trigger is based on the forward and backward coincidence, while the two photon trigger is based on a single hit. Another important subtrigger is the random trigger, which is useful to understand the background noise hits in the detector elements.

Global Decision Logic (GDL)

The GDL receives up to 48 subtrigger signals and aligns their timing by adding an appropriate delay to each channel. It then performs trigger logic operations to the subtrigger signals and generates 48 types of triggers. (Since exp. 21, the number of trigger types is increased to 64.) The GDL issues the final trigger $2.2 \mu\text{s}$ after the event's e^+e^- collision. For the hadronic trigger, the GDL has four main triggers:

- Two-track trigger: This requires the following information from the CDC: two tracks with $r - \phi$ and at least one track with z triggers and an open angle of at least 135° . This trigger also requires TOF hits and ECL clusters.
- Three-track triggers: This is similar to the two-track trigger, but with CDC $r - \phi$ information required for three or more tracks. Several different types of triggers are formed depending on the number of tracks, opening angle, TOF hits and ECL cluster hits.

- Isolated cluster counting trigger: This requires four or more isolated ECL clusters, which avoids Bhabha events.
- Total energy trigger: This requires that the analogue sum of energy deposited in the ECL be greater than 1 GeV. It is vetoed by the ECL Bhabha and cosmic triggers.
- Combined trigger: This is a combination of track trigger, energy and cluster trigger.

Each trigger provides 90% to 97% efficiency for $B\bar{B}$ events [34]. Because the track, energy and cluster triggers are almost independent, we expect more than 99% efficiency for $B\bar{B}$ events when using the overlap of these triggers. The trigger rate is correlated to the beam currents and the luminosity, but also depends on the beam background condition. In spite of the reduction of beam background and the modification of the trigger logic, the trigger rate gradually increases as the beam currents and the luminosity increases.

2.5.2 Level-3 (L3) and Level-4 (L4) Triggers

The aim of the level-3 trigger is to reduce the number of events to be stored. The L3 trigger first checks the L1 trigger information but passes some categories of events, such as Bhabha events and random trigger events. If an event does not belong to these categories, the L3 trigger performs a fast reconstruction and discards the event if it has no track with $|z| < 5$ cm at the IP. A large part of the beam background events are discarded by this procedure. The L3 software has been activated since Experiment 11 and results in a factor of two reduction of stored events while retaining an efficiency of more than 99% for hadronic and τ -pair events. The level-4 trigger filters events just before the full event reconstruction takes place [36]. The basic strategy of this trigger is to use a fast tracker to reconstruct tracks in order to reject tracks originating away from the IP. Events rejected by the L4 trigger still remain in the raw data. Thus the L3 trigger (and the L1 trigger) reduce the data size to

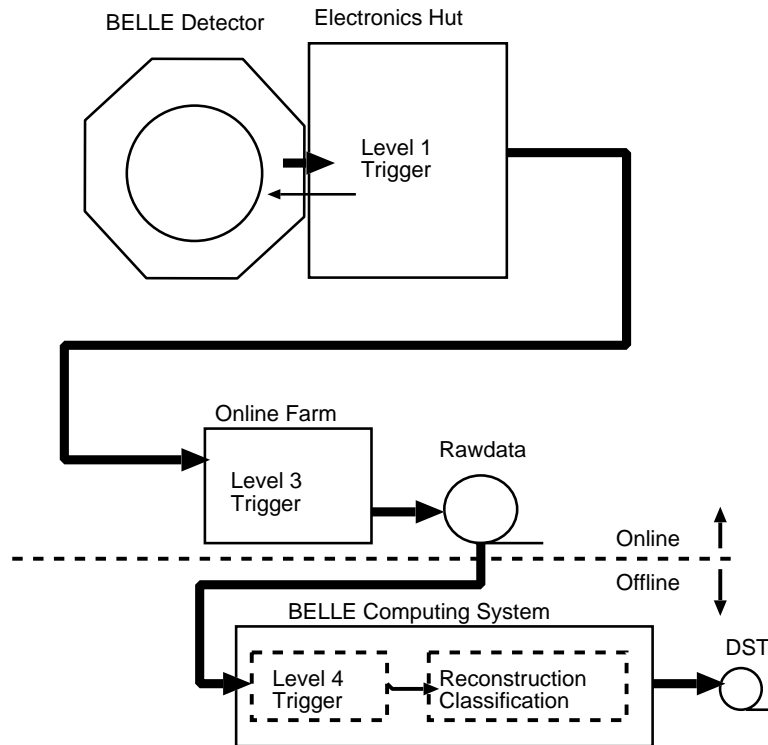


Figure 2.27: An overview of the Belle trigger system.

be recorded, while the L4 trigger reduces only the CPU time for DST production. The L4 trigger rejects about 78% of triggered events while keeping nearly 100% of B meson events.

2.5.3 Data Acquisition (DAQ)

The role of the DAQ system is to record events specified by the trigger up to its limit of 500 Hz, while keeping a dead-time fraction of the detector of less than 10%. To achieve this, a distributed-parallel system is used. The overview of the Belle data acquisition system [32] is shown in Fig. 2.29. The DAQ system is segmented into 7 subsystems to handle the data from each subdetector. The signals from most subdetectors go through a charge-to-time

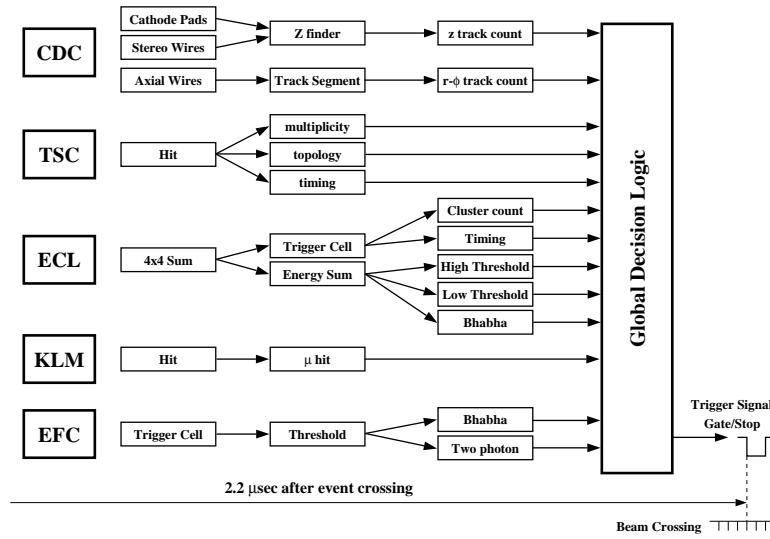


Figure 2.28: Belle level one (L1) trigger.

(Q-to-T) converter and are processed by a time-to-digital converter (TDC). The Q-to-T converter produces a pulse whose width is proportional to the input charge; the multihit TDC “digitize” the timings of the leading and trailing edges of this pulse. Only the SVD uses flash analogue-to-digital converters (FADCs) instead of TDCs. The KLM does not have a Q-to-T converter, since the pulse height does not provide useful information. The readout sequence starts when the sequence controller (SEQ), upon receiving a final trigger by the GDL, distributes a common stop signal to the TDCs. The data from each subdetector is combined into a single event by the event-builder, which converts “detector-by-detector” parallel data streams into “event-by-event” data. The output data of the event-builder is transferred through the level-3 trigger to the online computer farm. The quality of the data is monitored by the online data quality monitor (DQM) in the online farm. Finally, the data is sent via optical fiber to the mass storage system at the KEK computing center, where it is stored on tape. The typical size of a hadronic event is about 30 kB, which corresponds

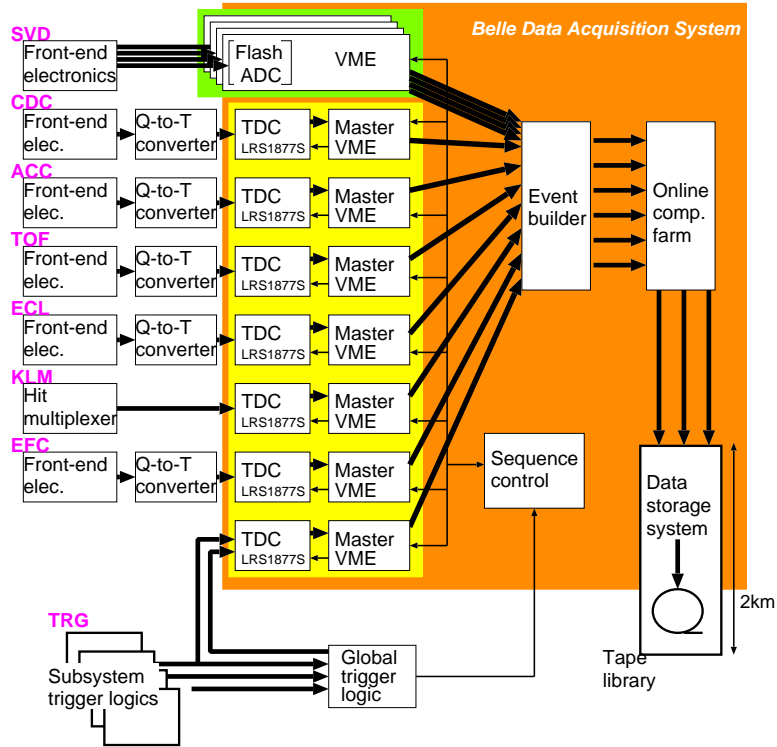


Figure 2.29: Belle data acquisition system.

to a maximum data transfer rate of 15 MB/s for a trigger rate of 500 Hz.

2.5.4 Data Processing

The events accepted by the L4 trigger are reconstructed and the information is stored on data summary tapes (DST). In this stage, raw data, which are direct logs of the data acquisition devices, are converted into physics objects of momentum 3-vector, closest approach to the IP and associated particle identification information. A basic summary of the reconstruction procedure is as follows. Charge tracks are reconstructed using signals from the CDC. They are extrapolated inwards to the SVD and outwards to the ACC, TOF, ECL

Table 2.6: Examples of event classification.

Category	Description
HadronB	general hadronic events
HadronC	tight general hadronic events (< 5 tracks)
Bhabha	Bhabha ($e^+e^- \rightarrow e^+e^-$) events
RadBhabha	radiative Bhabha ($e^+e^- \rightarrow e^+e^-\gamma$) events
GammaPair	$e^+e^- \rightarrow \gamma\gamma$ events
MuPair	$e^+e^- \rightarrow \mu^+\mu^-$ events
TauPair	$e^+e^- \rightarrow \tau^+\tau^-$ events
LowMulti	two photon events and others
Random	random triggered events

and KLM, where we look for associated signals. Hits in the ECL and KLM that have no associated track in the CDC will be deemed neutral particles (photons or K_L mesons). Four-vectors can then be assigned to the charged tracks and neutral particles and PID likelihoods are determined. Various other flags and variables are calculated and all the information is written to the DSTs. Events are then classified into several categories based on certain selection criteria and stored as skimmed data accordingly. Table 2.6 lists examples of the event classification. Most analyses, including this one, start from the HadronB sample.

2.6 Software

A large body of software has been developed by the Belle collaboration. As well as software to run the DAQ and data processing described above, software has been composed for

analyzing and simulating data. This is known as the Belle Analysis Framework (BASF). It consists of a main kernel, user interface and modules that can be dynamically loaded at run time. A typical user analysis can be written as a dynamically loaded module without having to worry about the interface with external software. BASF is also used for Monte Carlo (MC) generation, as described below.

2.6.1 Monte Carlo Generation

An important part of high energy physics data analysis is comparing the distributions of real data to expectations. Because of complexity of the detector response and various physics processes that may mimic the signal being studied, this comparison cannot be made using analytically derived distributions. Instead, the physics process and detector response are modelled using a Monte Carlo (MC) simulation. The real data distributions are then compared to the corresponding MC distributions that contains considerably more events (to reduce the statistical fluctuation of the simulated vs real data). This simulation is aware of the detailed geometry, response, and deficiencies of the entire Belle detector. It is used to study detector response of very rare types of events, enabling us to deduce ways to increase the sensitivity for such events. Producing MC data takes place in two stages. First, the underlying particle physics processes, from e^+e^- collision to the subsequent decays of very short-lived daughters, are generated. Then, the detector response to these particles is simulated. The first step uses the so called QQ generator [39] developed by the CLEO collaboration to study B meson decays created by the $\Upsilon(4S)$ resonance. It incorporates particle properties and event production rates compiled from many experiments in the form of world averages and also relevant information about the KEKB accelerator, such as electron and positron energies. For newer analyses, the modern EvtGen [40] package is used to generate the particle physics processes. It is thought to describe the angular

distributions of particles more accurately. Background continuum events are generated using the JETSET program [37] in which the subsequent hadronisation processes are based on the Lund string fragmentation model [38]. About three times the luminosity recorded in data is generated for the continuum events. The generated events, whether from QQ or EvtGen or JETSET, are then passed to a BASF module called GSIM. This module simulates the detector response; it is based on the CERN package GEANT3 [41] and simulates the interactions between the final state daughters and the detector response. The simulated data is then reconstructed in the same way as real data, with the final MDSTs containing the additional event generator information. Much effort is made to make the simulation as accurate as possible. Background hits are added by taking random trigger events and inserting their noise hits into the MC event. The varying size and position of the IP is incorporated as are evolutions in the subdetectors, such as appearance (or disappearance) of dead channels.

Chapter 3

Signal Reconstruction and Background Suppression

3.1 Overview of the analysis

In this analysis, we reconstruct the following five modes: $B^- \rightarrow \rho^- \gamma$, $\bar{B}^0 \rightarrow \rho^0 \gamma$, $\bar{B}^0 \rightarrow \omega \gamma$, $B^- \rightarrow K^{*-} \gamma$, and $\bar{B}^0 \rightarrow \bar{K}^{*0} \gamma$. Inclusion of charge conjugate modes is always implied. (The \bar{B}^0 and B^- mesons contain a b quark, while the B^0 and B^+ mesons contain a \bar{b} quark.) Intermediate states are reconstructed using the following decay channels: $\rho^- \rightarrow \pi^- \pi^0$, $\rho^0 \rightarrow \pi^+ \pi^-$, $\omega \rightarrow \pi^+ \pi^- \pi^0$, $K^{*-} \rightarrow K^- \pi^0$, $\bar{K}^{*0} \rightarrow K^- \pi^+$ and $\pi^0 \rightarrow \gamma \gamma$. Selection criteria for the particles that are used to reconstruct B meson candidates are determined by an optimization procedure using Monte Carlo (MC) events. The requirements are described in this section and are summarized in Table 3.3, and the optimization procedure is described in a later section 3.3.

3.1.1 Data set

This analysis is based on 357 fb^{-1} of data (≈ 386 million $B\bar{B}$ pairs) collected at the $\Upsilon(4S)$ resonance with the Belle detector.

The number of $B\bar{B}$ events ($N_{B\bar{B}}$) included in the data sample is estimated using the relation

$$N_{B\bar{B}} = N_{\text{on}} - \frac{\epsilon_{\text{on}}}{\epsilon_{\text{off}}} \frac{\mathcal{L}_{\text{on}}}{\mathcal{L}_{\text{off}}} N_{\text{off}} \quad (3.1)$$

where N_{on} (N_{off}), ϵ_{on} (ϵ_{off}), and \mathcal{L}_{on} (\mathcal{L}_{off}) are the number of events, the $q\bar{q}$ efficiency and the luminosity in on-resonance (off-resonance) data, respectively.

We use Monte Carlo (MC) simulation to study properties of signal and background events. The MC samples are itemized in Table 3.1.

3.1.2 Hadronic event selection

The hadronic events used in this analysis have three or more good charged tracks emerging from within a cylindrical region of radius 2.0 cm and length 10 cm centred on the e^+e^- interaction point and aligned with the positron beam axis (the z axis), and at least one ECL cluster of 0.1 GeV or more; the component along the z axis of the total center of mass (CM) momentum of all charged tracks and neutral ECL clusters must be below $0.5\sqrt{s}$ (where $\sqrt{s} = 10.58$ GeV); the sum E_{vis} (“visible energy”) of the charged track momenta and neutral cluster energies in the laboratory frame must exceed $0.2\sqrt{s}$; and the sum of the neutral cluster energies in the laboratory frame must lie between $0.1\sqrt{s}$ and $0.8\sqrt{s}$ with an average cluster energy of less than 1 GeV. We also require the heavy jet mass, which is defined as the larger of two invariant masses (calculated using the tracks in each of two hemispheres defined by the plane perpendicular to the event thrust axis), to exceed the

smaller of $1.8 \text{ GeV}/c^2$ and $0.25E_{\text{vis}}^*/c^2$ (where E_{vis}^* is the visible energy in the CM frame). The heavy jet mass is around $0.44E_{\text{vis}}^*/c^2$ for hadronic events but around $0.2E_{\text{vis}}^*/c^2$ for $e^+e^- \rightarrow \tau^+\tau^-$ pair events and around $0.1E_{\text{vis}}^*/c^2$ for QED events. We apply a selection of $M_{\text{jet}}c^2/E_{\text{vis}}^* > 0.25$. We do not reject events with $M_{\text{jet}} > 1.8 \text{ GeV}$ as the cut is slightly tight for $q\bar{q}$ events.

3.1.3 Photon Reconstruction

Photon candidates are reconstructed from isolated clusters in the ECL that have no corresponding charged track, and a shower shape that is consistent with that of a photon. A photon in the barrel region of the ECL ($33^\circ < \theta_\gamma < 128^\circ$ in the laboratory frame) with a CM energy in the range $1.8 \text{ GeV} < E_\gamma < 3.4 \text{ GeV}$ is selected as the primary photon candidate. For the primary photon, we sum the energy deposited in arrays of 3×3 and 5×5 ECL cells around the maximum energy cell; if their ratio is less than 0.95, the event is vetoed. To suppress backgrounds from $\pi^0 \rightarrow \gamma\gamma$ and $\eta \rightarrow \gamma\gamma$ decays, we veto the event based on a likelihood ratio $L_{\pi^0}/(L_{\pi^0} + L_\gamma)$ and $L_\eta/(L_\eta + L_\gamma)$. For each photon (γ_2) other than the primary photon (γ_1) in the event, the π^0 , η and primary photon likelihoods (L_{π^0} , L_η , L_γ) are calculated as a function of the invariant mass $m_{\gamma_1\gamma_2}$ and the energy of the second photon E_{γ_2} . For every such photon-pair combination, we require the likelihood ratios to satisfy $L_{\pi^0}/(L_{\pi^0} + L_\gamma) > 0.4$ and $L_\eta/(L_\eta + L_\gamma) > 0.5$; otherwise the event is neglected by this “ π^0/η veto.”

3.1.4 Neutral pion reconstruction

Neutral pions are formed from photon pairs (excluding the primary photon) with an invariant mass within $\pm 16 \text{ MeV}/c^2$ of the nominal π^0 mass, corresponding to a $\sim 3\sigma$ window, where σ is the π^0 mass resolution. The photon momenta are then recalculated by applying a

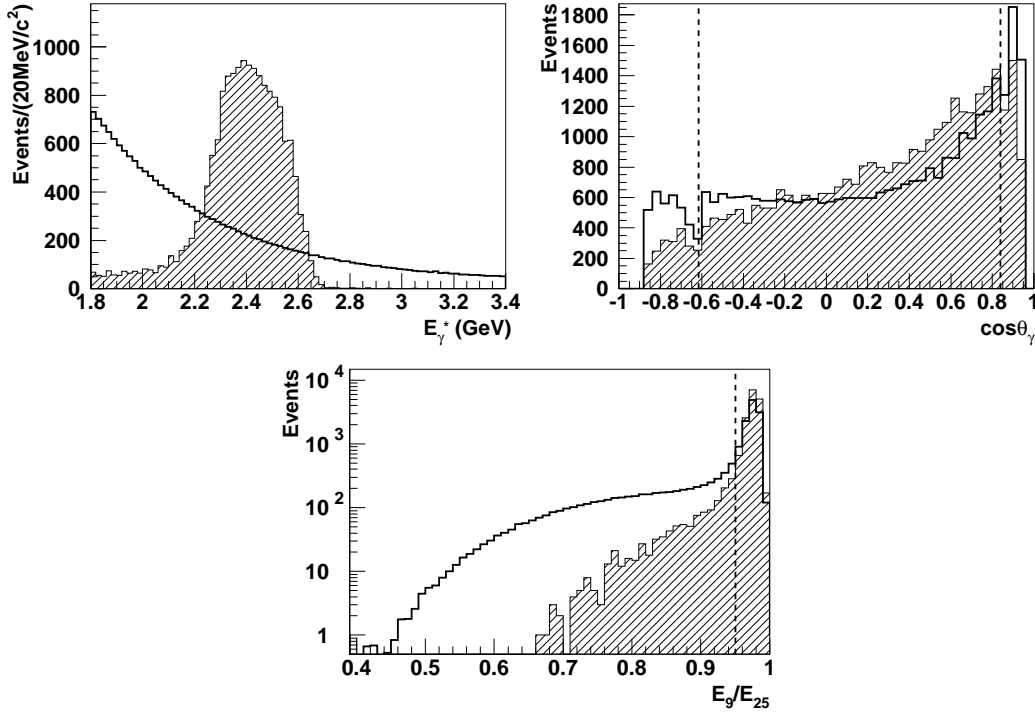


Figure 3.1: Distributions for (a) E_{γ}^* , (b) $\cos\theta_{\gamma}$ and (c) E_9/E_{25} . (Histograms (Signal-hatched, plain-qq) are normalized to histogram for signal)

π^0 mass constraint. We require the energy of each photon be greater than 50 (100) MeV in the barrel (endcap) ECL. We also require the cosine of the laboratory frame angle between two photons ($\cos\theta_{\gamma\gamma}$) be greater than 0.7. This is almost equivalent to, but more effective than, a requirement on π^0 momentum or photon energy asymmetry.

3.1.5 Charged pion reconstruction

Charged pions and kaons are reconstructed as tracks in the CDC and SVD. Each track is required to have a transverse momentum above 100 MeV/ c and distance of closest approach to the interaction point of less than 0.5 cm in the $x - y$ plane and ± 3 cm along the z axis.

We do not use the track to form the signal candidate if, when combined with any other track, it forms a K_S^0 candidate with an invariant mass within $\pm 30 \text{ MeV}/c^2$ of the nominal K_S^0 mass and a displaced vertex that is consistent with a K_S^0 . We determine the pion (L_π) and kaon (L_K) likelihoods from ACC, CDC and TOF information, and form a likelihood ratio $L_\pi/(L_\pi + L_K)$ to separate pions from kaons. In the $B^- \rightarrow \rho^- \gamma$, $\bar{B}^0 \rightarrow \rho^0 \gamma$ and $\bar{B}^0 \rightarrow \omega \gamma$ modes, tracks are identified as pion if this likelihood exceeds 0.8, 0.85 and 0.6, respectively; otherwise they are called kaons. We do not veto electrons, muons nor protons. The corresponding signal efficiencies are 83%, 81% and 91%, respectively. With these criteria, 5.8% and 6.3% of kaons are misidentified as pions in the $B^- \rightarrow \rho^- \gamma$ and $\bar{B}^0 \rightarrow \rho^0 \gamma$ modes, respectively; therefore, the contribution of the misidentified $\bar{B} \rightarrow \bar{K}^* \gamma$ background in both modes has to be evaluated. For this evaluation, we form a $\bar{B} \rightarrow \bar{K}^* \gamma$ enriched sample where in a track is identified as a kaon if $L_K/(L_\pi + L_K) > 0.4$; this has an efficiency of 90% for $\bar{B} \rightarrow \bar{K}^* \gamma$.

3.1.6 Reconstruction of ρ , ω and K^*

Invariant masses for the ρ , ω and K^* candidates from identified pions and/or kaons are required to be within windows of $\pm 150 \text{ MeV}/c^2$, $\pm 30 \text{ MeV}/c^2$ and $\pm 75 \text{ MeV}/c^2$ respectively, around their nominal masses. We calculate the helicity angle (θ_{hel}) of their decay products, and require that $|\cos \theta_{\text{hel}}|$ be smaller than 0.75, 0.70 or 0.80 for $B^- \rightarrow \rho^- \gamma$, $\bar{B}^0 \rightarrow \rho^0 \gamma$ or $\bar{B}^0 \rightarrow \omega \gamma$, respectively.

3.1.7 Reconstruction of B candidate

B candidates are reconstructed by combining a ρ , ω or K^* candidate and the primary photon using two variables: the energy difference $\Delta E = E_B^* - E_{\text{beam}}^*$ and the beam-energy constrained mass

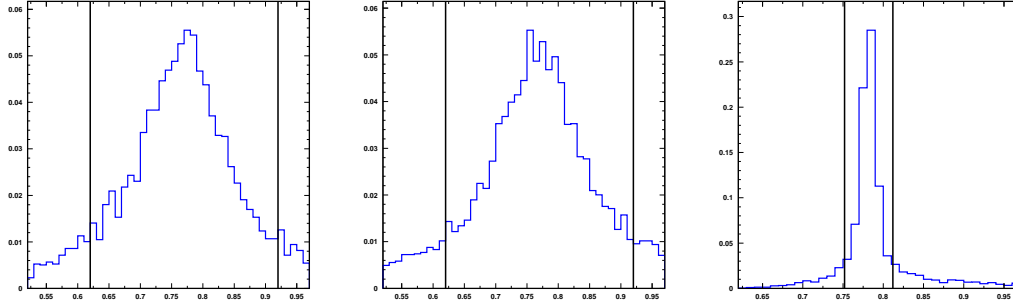


Figure 3.2: Distributions for invariant masses of ρ^- , ρ^0 and ω mesons. The vertical lines define windows of accepted candidates.

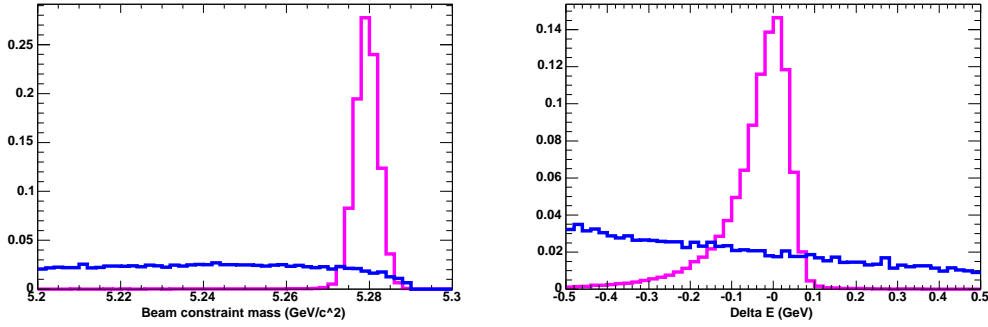


Figure 3.3: Distributions for beam constraint mass (M_{bc}) and Energy difference (ΔE).

$$M_{bc} = \sqrt{(E_{\text{beam}}^*/c^2)^2 - |\vec{p}_B^*/c|^2}, \quad \vec{p}_B^* = \vec{p}_{\rho,\omega,K^*}^* + \frac{\vec{p}_\gamma^*}{|\vec{p}_\gamma^*|} \times (E_{\text{beam}}^* - E_{\rho,\omega,K^*}^*) \quad (3.2)$$

Here, p_B^* and E_B^* are the CM momentum and energy of the B candidate and E_{beam}^* is the CM beam energy. The replacement of the magnitude of the photon momentum by $(E_{\text{beam}}^* - E_{\rho/\omega/K^*}^*)/c$ in \vec{p}_B^* is a standard technique in a radiative B decay analysis to reduce the tail and improve the resolution of the M_{bc} peak.

The signal region is defined as $-0.10 \text{ GeV} < \Delta E < 0.08 \text{ GeV}$ and $5.273 \text{ GeV}/c^2 <$

$M_{bc} < 5.285 \text{ GeV}/c^2$; the wide fit region is defined as $|\Delta E| < 0.5 \text{ GeV}$ and $M_{bc} > 5.2 \text{ GeV}/c^2$.

3.2 Background

The dominant background arises from continuum events ($e^+e^- \rightarrow q\bar{q}(\gamma)$), where the accidental combination of a ρ , ω or K^* candidate with a photon forms a B candidate. Since the branching fraction for $\bar{B} \rightarrow \rho\gamma$ and $\bar{B}^0 \rightarrow \omega\gamma$ modes are expected to be of order 10^{-6} , the contamination from other more frequent B decays is quite significant. This is in contrast with the analysis of the $\bar{B} \rightarrow \bar{K}^*\gamma$ control sample ($BF \sim \mathcal{O}(10^{-4})$) in which the contamination from other B decays is rather small.

In this section, we discuss the backgrounds and the suppression techniques that we exploit in this analysis. For the backgrounds from other B decays, we rely on the MC simulation; the MC samples used for the signal and background description are summarized in Table 3.1.

3.2.1 Continuum Background

We use the standard Belle technique to reduce the continuum events based on an event-shape likelihood ratio. Using the daughter particles of the signal B candidate and all the other particles in the event (which are assumed to originate from another “tagging” B meson), we calculate the following variables: the event shape variable, the cosine of the signal B meson direction in the CM frame ($\cos\theta_B^*$), the flavor tagging quality $q \cdot r$ of the tagging B meson, and, for the $\bar{B}^0 \rightarrow \rho^0\gamma$, $\bar{B}^0 \rightarrow \omega\gamma$ and $\bar{B}^0 \rightarrow \bar{K}^{*0}\gamma$ modes, the axial distance Δz between the vertex of the signal B candidate and that of the tagging B meson. We do not use other variables such as the helicity angle or invariant mass of ρ , ω and K^*

candidates.

Event shape variable

We use topology to distinguish such continuum events from $e^+e^- \rightarrow \Upsilon(4S) \rightarrow B\bar{B}$ events. In the CM frame, the $q\bar{q}$ events tend to emerge as back-to-back jets, whereas the $B\bar{B}$ events have their final state particles distributed isotropically. The event topology is characterized numerically by a Fisher discriminant \mathcal{F} [43] that incorporates modified Fox-Wolfram event shape moments [44] with accommodation for missing momentum in the event as well as the correlation of jet charge between the tracks of the signal B candidate and those of the tagging B meson.

The Fox-Wolfram moments [44] are defined in the center of mass frame by

$$H_\ell = \frac{1}{s} \sum_i \sum_j |\vec{p}_i| |\vec{p}_j| P_\ell(\cos \theta_{ij}) \quad (3.3)$$

where s is the square of the center of mass energy, $P_\ell(x)$ is the Legendre polynomial of order ℓ , and each sum is over all of the reconstructed particles in an event. These moments are used to characterize the shape of the event. Note that $H_0 = 1$ if all particles are reconstructed and are treated as massless, but is typically somewhat smaller; $H_1 = 0$ if momentum is balanced; and $H_\ell \approx 1$ (0) if ℓ is even (odd) in two-jet events. One common tactic normalizes these moments by defining the ratios

$$R_\ell = \frac{H_\ell}{H_0} = \frac{\sum_i \sum_j |\vec{p}_i| |\vec{p}_j| P_\ell(\cos \theta_{ij})}{\sum_i \sum_j |\vec{p}_i| |\vec{p}_j|}. \quad (3.4)$$

The quantity R_2 , for example, tends to discriminate quite well between continuum (jet-like) and $B\bar{B}$ (spherical) events at the $\Upsilon(4S)$ resonance. A Fisher discriminant \mathcal{F}'' can be constructed from the first few ratios:

$$\mathcal{F}'' = \alpha_1 R_1 + \alpha_2 R_2 + \alpha_3 R_3 + \alpha_4 R_4 + \dots, \quad (3.5)$$

with the α_j chosen to provide the optimum separation between continuum and $B\bar{B}$ events.

R. Enomoto [46] found that the continuum– $B\bar{B}$ separation is improved if the reconstructed tracks are classified according to the hypothesis that certain ones belong to the “signal” B meson and the remainder belong to the “opposite” (i.e, tagging) B meson. With this classification, the modified Super Fox-Wolfram submoments are defined separately for “signal–opposite” (also known as “major”) and “opposite–opposite” (aka “minor”) combinations as

$$H_\ell^{so} = \frac{1}{s} \sum_i \sum_j |\vec{p}_i| |\vec{p}_j| P_\ell(\cos \theta_{ij}) \quad (3.6)$$

$$H_\ell^{oo} = \frac{1}{s} \sum_j \sum_k |\vec{p}_j| |\vec{p}_k| P_\ell(\cos \theta_{jk}) \quad (3.7)$$

where i runs over all signal particles, and j and k run over all opposite particles. The scaled submoments are given by

$$R_\ell^{so} = \frac{H_\ell^{so}}{H_0^{so}} = \frac{\sum_i \sum_j |\vec{p}_i| |\vec{p}_j| P_\ell(\cos \theta_{ij})}{\sum_i \sum_j |\vec{p}_i| |\vec{p}_j|} \quad (3.8)$$

$$R_\ell^{oo} = \frac{H_\ell^{oo}}{H_0^{oo}} = \frac{\sum_j \sum_k |\vec{p}_j| |\vec{p}_k| P_\ell(\cos \theta_{jk})}{\sum_j \sum_k |\vec{p}_j| |\vec{p}_k|} \quad (3.9)$$

where index i (j and k) runs over all signal (opposite) particles. A modified Fisher discriminant \mathcal{F}' can be constructed from these:

$$\mathcal{F}' = \alpha_0^{so} R_0^{so} + \alpha_0^{oo} R_0^{oo} + \alpha_1^{so} R_1^{so} + \alpha^{oo} R_1^{oo} + \alpha_2^{so} R_2^{so} + \alpha_3^{oo} R_2^{oo} + \dots \quad (3.10)$$

with the α_ℓ^{so} and α_ℓ^{oo} chosen to provide the optimum separation between continuum and $B\bar{B}$ events.

H. Kakuno observed that the continuum– $B\bar{B}$ separation using \mathcal{F}' is best if all (or nearly all) of the particles are reconstructed, but is quite poor if there are many missing and/or unobserved particles. He proposed

- defining a pseudo-particle that has the event’s missing energy E_{miss} , momentum \vec{p}_{miss} , and squared mass M_{miss}^2
- forming three signal–opposite submoments of each moment: one for the “opposite” charged particles, one for the “opposite” neutral particles, and one for the missing pseudo-particle (with the π^\pm daughters of a K_s meson removed from the charged list and the neutral K_s added instead to the neutral list)
- forming the modified Fox-Wolfram moments relative to $2(E_{\text{beam}} - \Delta E)$ rather than E_{beam} , to account for mismeasurement of the “signal” B meson’s energy and momentum
- using the newly defined submoments, rather than the scaled submoments, to calculate the modified Fisher discriminant
- adding an extra term to the Fisher discriminant—the scalar sum of all observed transverse momenta—to compensate for the weak discrimination between B -decay events and continuum when there is substantial missing energy/momentum.

The signal–opposite submoments for the opposite’s charged particles are:

$$H_\ell^{\text{soc}} = \frac{1}{2(E_{\text{beam}} - \Delta E)} \begin{cases} \sum_i \sum_j |\vec{p}_j| P_\ell(\cos \theta_{ij}) & \text{if } \ell \text{ is even} \\ \sum_i \sum_j Q_i Q_j |\vec{p}_j| P_\ell(\cos \theta_{ij}) & \text{if } \ell \text{ is odd and } Q_j = \pm 1 \end{cases} \quad (3.11)$$

where i runs over all signal particles and j runs over all charged opposite particles. The signal–opposite submoments for the opposite’s neutral particles are:

$$H_\ell^{son} = \frac{1}{2(E_{\text{beam}} - \Delta E)} \begin{cases} \sum_i \sum_j |\vec{p}_j| P_\ell(\cos \theta_{ij}) & \text{if } \ell \text{ is even} \\ 0 & \text{if } \ell \text{ is odd} \end{cases} \quad (3.12)$$

where i runs over all signal particles and j runs over all neutral opposite particles. The submoments for the pseudo-particle are:

$$H_\ell^{sm} = \frac{1}{2(E_{\text{beam}} - \Delta E)} \begin{cases} \sum_i |\vec{p}_i| P_\ell(\cos \theta_{iM}) & \text{if } \ell \text{ is even} \\ 0 & \text{if } \ell \text{ is odd} \end{cases} \quad (3.13)$$

where i runs over all signal particles, and θ_{iM} is the opening angle between \vec{p}_i and \vec{p}_{miss} .

The opposite–opposite submoments are:

$$H_\ell^{oo} = \frac{1}{4(E_{\text{beam}} - \Delta E)^2} \begin{cases} \sum_j \sum_k |\vec{p}_j| |\vec{p}_k| P_\ell(\cos \theta_{jk}) & \text{if } \ell \text{ is even} \\ \sum_j \sum_k Q_j Q_k |\vec{p}_j| |\vec{p}_k| P_\ell(\cos \theta_{jk}) & \text{if } \ell \text{ is odd} \end{cases} \quad (3.14)$$

where j and k run over all opposite particles.

From the first five scaled submoments of each category plus the sum of the scalar transverse momenta $\sum_j |\vec{p}_{\perp j}|$, seven modified Fisher discriminants \mathcal{F}_j are constructed, one for each of the following ranges of squared missing mass [in units of GeV^2/c^4]: $(-\infty, -0.5)$, $(-0.5, 0.3)$, $(0.3, 1.0)$, $(1.0, 2.0)$, $(2.0, 3.5)$, $(3.5, 6.0)$, and $(6.0, \infty)$:

$$\mathcal{F} = \sum_{\ell=0}^4 \left(\alpha_\ell^{soc} R_\ell^{soc} + \alpha_\ell^{son} R_\ell^{son} + \alpha_\ell^{sm} R_\ell^{sm} + \alpha_\ell^{oo} R_\ell^{oo} \right) + \beta \sum_j |\vec{p}_{\perp j}| \quad (3.15)$$

with the α_ℓ and β chosen to provide the optimum separation between continuum and $B\bar{B}$ events within the selected squared-missing-mass range. The distribution of this quantity for signal and continuum events is shown in Fig. 3.4(a).

***B* flight direction**

The polar angle θ_B^* in the center of mass frame of the B meson candidate is an independent discriminator between signal and continuum background since true B mesons, being spinless daughters arising from a spin-1 $\Upsilon(4S)$ parent, follow a $\sin^2 \theta_B^*$ distribution. In contrast, the false B meson candidates formed as random combinations in continuum events emerge uniformly in solid angle. The distributions of $\cos \theta_B^*$ for signal and continuum events are shown in Fig. 3.4(b).

Vertex position

In about 80% of the neutral events, a fit can be performed successfully to determine the decay vertex along the z axis of the signal B^0 candidate as well as the origin of the tagging B meson. These two points will coincide for continuum events but will be separated somewhat in the lab frame along the z axis for true $B\bar{B}$ events since the B and \bar{B} mesons do not decay simultaneously. The distributions of Δz for B^0 -decay and continuum events are shown in Fig. 3.4(c); note that the Δz resolutions for SVD1 and SVD2 differ somewhat. We do not distinguish the two cases with Δz because the background discrimination power of Δz is smaller than that of the \mathcal{F} and hence the $L_{S(B)}$ distributions are rather similar, and the fraction of the events without Δz in the $\bar{B}^0 \rightarrow \rho^0 \gamma$, $\bar{B}^0 \rightarrow \omega \gamma$ and $\bar{B}^0 \rightarrow \bar{K}^{*0} \gamma$ signal events is only about 20%.

Likelihood Ratio

For each of the \mathcal{F} , $\cos \theta_B^*$ and Δz variables, we calculate the one-dimensional likelihood to be the signal or background. For \mathcal{F} and $\cos \theta_B^*$, we use the signal (continuum) MC samples to construct the signal (background) probability density functions (PDF). For the

background Δz distribution, we use the sideband data ($5.2 \text{ GeV}/c^2 < M_{bc} < 5.24$ and $-0.1 \text{ GeV} < \Delta E < +0.5 \text{ GeV}$) to determine the PDFs separately for the SVD1 and SVD2 datasets. For the signal Δz distribution, we use signal MC sample to determine the mode specific PDF separately for SVD1 and SVD2 datasets.

The independent likelihoods are combined into a product L_S (or L_B) of the three if the Δz information is available and satisfies $|\Delta z| < 0.2 \text{ cm}$, or otherwise of the first two:

$$L_S = \begin{cases} L'_S(\mathcal{F}) \times L''_S(\cos \theta_B^*) \times L_S^{SVD1}(\Delta z) & \text{(if } \Delta z \text{ is available for SVD1),} \\ L'_S(\mathcal{F}) \times L''_S(\cos \theta_B^*) \times L_S^{SVD2}(\Delta z) & \text{(if } \Delta z \text{ is available for SVD2),} \\ L'_S(\mathcal{F}) \times L''_S(\cos \theta_B^*) & \text{(otherwise)} \end{cases} \quad (3.16)$$

with L_B defined in a corresponding fashion.

Using the signal and background likelihoods, we calculate the likelihood ratio for the event,

$$\mathcal{R} = \frac{L_S}{L_S + L_B}. \quad (3.17)$$

We classify the events into six bins of flavor quality $q \cdot r$ (using the Belle standard flavor tagging procedure) and determine the requirement of \mathcal{R} in each bin in the optimization procedure (section 3.3). The quality factor r lies between 0 (for an event where the B -tag flavor cannot be determined reliably) and 1 (for an event where B -tag is known); the flavor is given by $q = +1$ (if the signal and tagging b mesons appear to have the same flavor (i.e., both contain a b quark)) or $q = -1$ otherwise. For the \bar{B}^0 modes, we classify the events into the standard set of six bins of the r value, that has two equal size bins between 0 and 0.5 and four equal size bins between 0.5 and 1. For the B^- modes, we classify into the same six r bins if $q = -1$ (“opposite flavor B mesons”), or into the bin with the smallest r if $q = +1$ (“same flavor B mesons”).

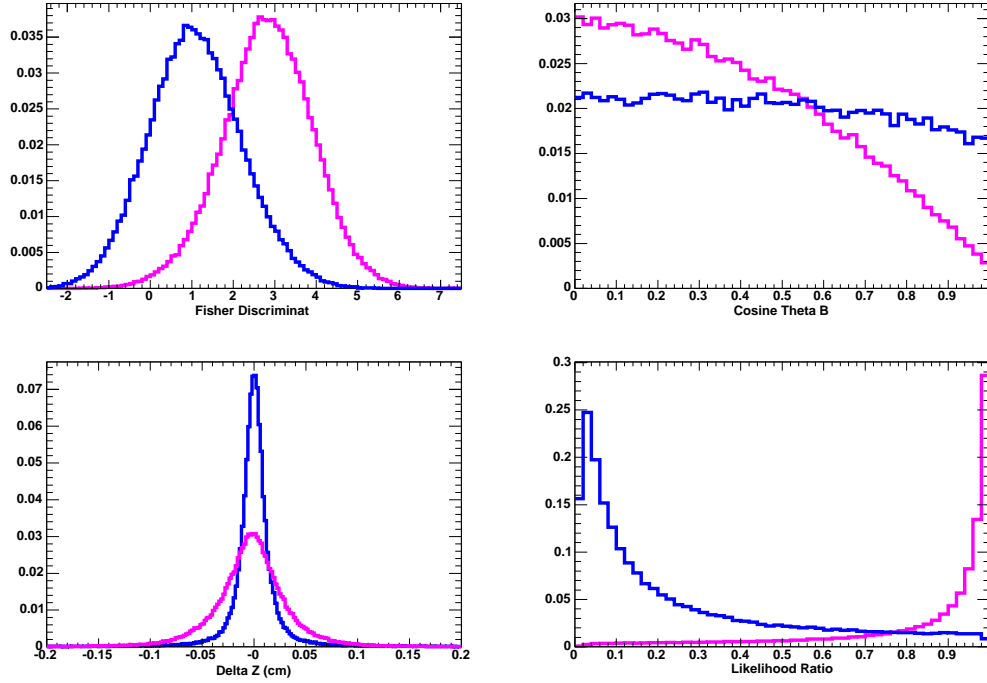


Figure 3.4: Distributions for (a) Event-shape (\mathcal{F}), (b) $\cos\theta_B$, vertex separation ΔZ and Likelihood Ratio (Labels: signal- purple and continuum background- blue)

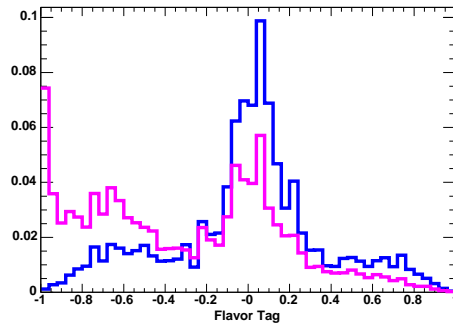


Figure 3.5: Quality of B flavor tag "q.r" (Labels: signal- purple and continuum background- blue)

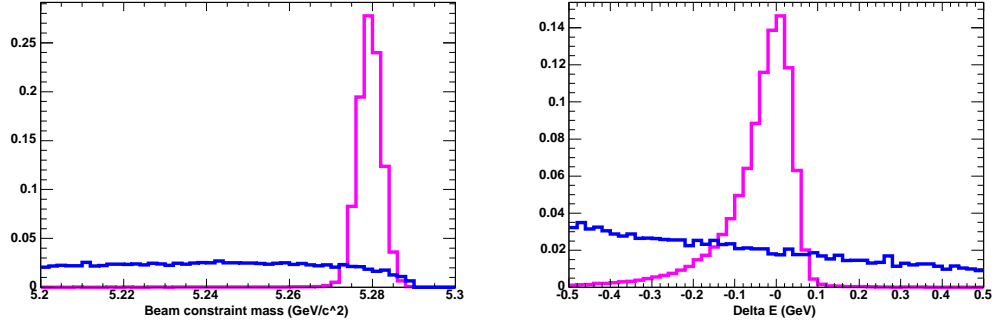


Figure 3.6: Distributions for (a) M_{bc} (b) ΔE (Labels: signal- purple and Continuum background- blue)

Residual Continuum Background

The remaining continuum background contribution is extracted from the fit to the data in the M_{bc} and ΔE plane. The continuum background distribution is modeled as the product of an ARGUS function [47] for M_{bc} with a first order polynomial for ΔE . Each function has one parameter to determine the characteristics: the shape parameter of the ARGUS function and the slope of the straight line. We allow both of them to float in the final fit as we do not have a good control sample to fix their values. (For example, they are correlated with \mathcal{R} , so we cannot determine them from a continuum enriched sample with a flipped- \mathcal{R} requirement.)

3.2.2 $\bar{B} \rightarrow \bar{K}^* \gamma$ Background

When the charged kaon is misidentified as a charged pion, the more copious $B^- \rightarrow K^{*-} \gamma$ and $\bar{B}^0 \rightarrow \bar{K}^{*0} \gamma$ become a serious background source to the rare modes $B^- \rightarrow \rho^- \gamma$ and $\bar{B}^0 \rightarrow \rho^0 \gamma$, respectively. A large fraction of these background events can be removed by rejecting the events when the “ K ” π mass is consistent with K^* , although at a rather high cost of signal efficiency. (The “ K ” π mass is the invariant mass when the kaon mass is assigned

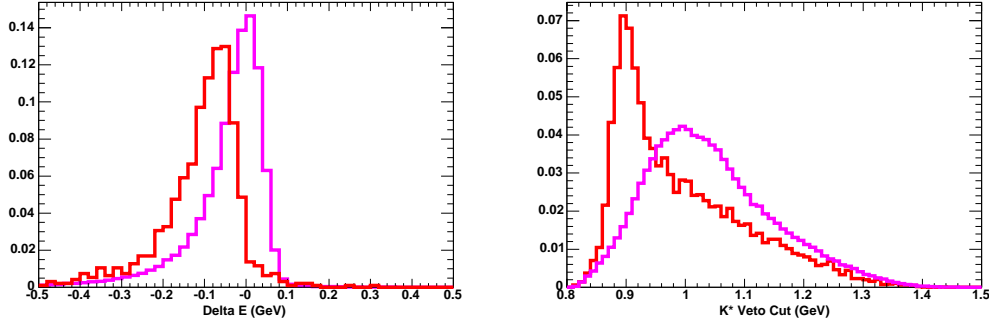


Figure 3.7: Distributions for (a) ΔE and, (b) K_π Mass (Labels: signal- purple and $B \rightarrow K^*\gamma$ background- blue)

to one of the two pion candidates.) $\bar{B}^0 \rightarrow \rho^0\gamma$ is more affected than $B^- \rightarrow \rho^-\gamma$ since the relative branching fraction is smaller and there are two charged pions, either of which might have been misidentified. For $\bar{B}^0 \rightarrow \omega\gamma$, the lower tail of $\bar{K}^{*0} \rightarrow K_S^0\pi^0 \rightarrow \pi^+\pi^-\pi^0$ has an overlap with the ω mass; by rejecting the $K_S^0 \rightarrow \pi^+\pi^-$ tracks, this background is significantly reduced. Finally, there are broken $\bar{B} \rightarrow \bar{K}^*\gamma$ signals where a pion is selected incorrectly from the rest of the event in place of the kaon. This happens regardless the charge of the source and the analysis mode. To model the remaining $\bar{B} \rightarrow \bar{K}^*\gamma$ background, we use a 50×50 two-dimensional MC histogram in the M_{bc} - ΔE plane, scaled to the expected number of events based on the observed $\bar{B} \rightarrow \bar{K}^*\gamma$ branching fraction and the measured kaon-to-pion misidentification rate. The dominant part has a distribution similar to that of the $\bar{B} \rightarrow \rho\gamma$ signal but with a shifted ΔE and a modified M_{bc} tail. Contributions from $B^- \rightarrow K^{*-}\gamma$ to $\bar{B}^0 \rightarrow \rho^0\gamma$ and $\bar{B}^0 \rightarrow \omega\gamma$, and from $\bar{B}^0 \rightarrow \bar{K}^{*0}\gamma$ to $B^- \rightarrow \rho^-\gamma$, are included in the other rare B decays.

3.2.3 Other $B \rightarrow X_s \gamma$ background

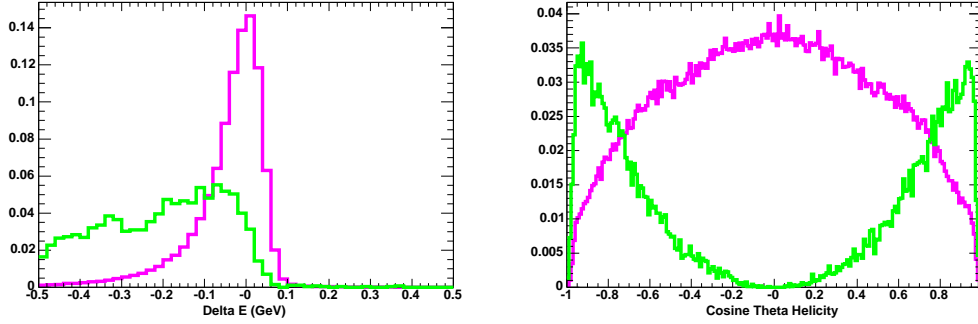
Similarly to the broken $\bar{B} \rightarrow \bar{K}^* \gamma$ signals, other inclusive $B \rightarrow X_s \gamma$ events have a high energy photon: and it is then possible to combine pions to form a false ρ or ω meson. To model this background's distribution in the $M_{bc} - \Delta E$ plane, we remove the $\bar{B} \rightarrow \bar{K}^* \gamma$ component from an inclusive $B \rightarrow X_s \gamma$ sample of MC events. The scale is normalized to the PDG inclusive $B \rightarrow X_s \gamma$ branching fraction (where $\bar{B} \rightarrow \bar{K}^* \gamma$ contribution is subtracted).

3.2.4 $B \rightarrow V \pi^0$ and $B \rightarrow V \eta$

The $B \rightarrow V \pi^0$ and $B \rightarrow V \eta$ modes, where V stands for either ρ^- , ρ^0 or ω , are serious background sources to the corresponding $B \rightarrow V \gamma$ signal modes when the π^0 or η meson is misidentified as a single photon. This occurs when one of the photons in $\pi^0 \rightarrow \gamma \gamma$ or $\eta \rightarrow \gamma \gamma$ is unobserved or too soft to be rejected by the π^0/η veto condition 3.1.3. Since the helicity angle of the V has a $\cos^2 \theta_{\text{hel}}$ distribution in these backgrounds in contrast to $(1 - \cos^2 \theta_{\text{hel}})$ for the signal, these backgrounds are suppressed by a helicity angle requirement. Furthermore, the ΔE peak is shifted to the lower values due to the missing photon. Each background is modeled as a two-dimensional histogram and normalized to the HFAG [52] branching fractions (or upper limits). Contributions from $B^- \rightarrow V^- \pi^0$ and $B^- \rightarrow V^- \eta$ to $\bar{B}^0 \rightarrow \rho^0 \gamma$ and $\bar{B}^0 \rightarrow \omega \gamma$, and from $\bar{B}^0 \rightarrow V^0 \pi^0$ and $\bar{B}^0 \rightarrow V^0 \eta$ to $B^- \rightarrow \rho^- \gamma$, are included in the other rare B decays 3.2.5.

3.2.5 Other Rare B Decays

The contribution of other B rare decays to the final event sample are small. To model this background for each of the signal modes, we form a 50×50 two-dimensional histogram from the rare B MC sample, from which all aforementioned decay modes are excluded. The scale



[Distributions for ΔE and $\cos\theta_{\text{hel}}$ for $B \rightarrow V\pi^0$ background] Distributions for (a) ΔE and, (b) $\cos\theta_{\text{hel}}$ for $B \rightarrow V\pi^0$ background (Labels: signal- purple and $B \rightarrow V\pi^0$ background- green)

is normalized to PDG branching fractions.

3.2.6 Generic B Decays

Within the generic ($b \rightarrow c$) MC sample (three times larger than our dataset), we found only a handful of events in any modes within the fit region of $M_{bc} - \Delta E$ plane before imposition of the \mathcal{R} and $q \cdot r$ requirements. Therefore, we neglect this component.

3.2.7 Other $b \rightarrow d\gamma$ Component

In principle, there could be a non-resonant $\pi\pi(\pi^0)$ component under the $\rho(\omega)$ resonance. We consider such events as the part of the signal, even though, technically, they are not the exclusive B decay modes that we seek to identify: they still originate from the $b \rightarrow d\gamma$ process.

3.2.8 Off-timing Bhabha Overlaid with Another Event

A candidate event might, in rare occasions, contain a fragment of an off-time $e^+e^- \rightarrow e^+e^-$ (Bhabha Scattering) event in the form of an energetic ECL cluster but without CDC track hits. This ECL cluster of the off-time Bhabha event mimics a high energy photon and cannot be suppressed by any of the previously described cuts. We have examined 100 fb⁻¹ data set corresponding to experiments 39 and 41, where additional event timing information was recorded to permit such event overlap. About 2% of our candidate events are off-timing for $B^- \rightarrow \rho^- \gamma$ and $\bar{B}^0 \rightarrow \omega \gamma$ (but none are off-timing for $\bar{B}^0 \rightarrow \rho^0 \gamma$). Since this contamination exhibits no structure in the M_{bc} and ΔE , we conclude that it does not affect the $b \rightarrow d \gamma$ analysis.

3.3 Analysis Optimization

Some of the requirements in Table 3.3 on the photon (E_9/E_{25} , polar angle and E_γ), charged tracks (dr , dz , p_T , K_S^0 veto) and π^0 candidates (E_γ) are fixed at the early stage of the analysis (as Belle standards or deliberately chosen as very loose).

We choose other selection criteria in Table 3.3 to roughly maximize the value of $N_S/\sqrt{N_B}$ for each of the $\bar{B} \rightarrow \rho \gamma$ and $\bar{B}^0 \rightarrow \omega \gamma$ modes. (We do not optimize for the combined fit result.) Here, N_S is the MC signal yield, using the SM branching fractions in Ref. [8], in the signal region after all the requirements are applied, and N_B is the MC background yield. (Here, both yields are obtained by counting rather than fitting.) For the background yield, we use the sum of the identified background sources: continuum, $\bar{B} \rightarrow \bar{K}^* \gamma$, $B \rightarrow V \pi^0$, $B \rightarrow V \eta$ and other rare B decays. Since the number of background MC events is small in the signal region and subject to statistical fluctuations, we count the number of background events in the wider fit region, and then scale by a factor corresponding to the fraction of

events in the signal region versus the fit region. This scale factor is calculated with no requirement on \mathcal{R} and $q \cdot r$.

For the $\bar{B} \rightarrow \bar{K}^* \gamma$ enriched modes, we use the requirements for the corresponding $\bar{B} \rightarrow \rho \gamma$ modes, except that we select a kaon instead of the pion, and we require that $M(K\pi)$ is within the K^* resonance instead of outside.

Table 3.1: Summary of the MC samples for signal and background.

Mode	Events ($\times 10^6$)	\mathcal{B} ($\times 10^{-6}$)	Expected events			Relative size
			$\rho^- \gamma$	$\rho^0 \gamma$	$\omega \gamma$	
$B^- \rightarrow \rho^- \gamma$	0.4	0.90 (SM)				$\times 1150$
$\bar{B}^0 \rightarrow \rho^0 \gamma$	0.4	0.49 (SM)				$\times 2100$
$\bar{B}^0 \rightarrow \omega \gamma$	0.4	0.49 (SM)				$\times 2100$
$B^- \rightarrow K^{*-} \gamma$	0.4	40.3 ± 2.6				$\times 25.7$
$\bar{B}^0 \rightarrow \bar{K}^{*0} \gamma$	0.4	40.1 ± 2.0				$\times 25.9$
$B \rightarrow X_s \gamma$	0.85	339^{+30}_{-27}	58.9	23.5	14.9	$\times 3.7$
$B^- \rightarrow K^{*-} \pi^0$	0.4	12 ± 2	8.5	—	—	$\times 86.4$
$\bar{B}^0 \rightarrow \bar{K}^{*0} \pi^0$	0.4	1.8 ± 0.6	—	1.0	—	$\times 576$
$B^- \rightarrow K^{*-} \eta$	0.4	8.4 ± 1.7	6.0	—	—	$\times 123$
$\bar{B}^0 \rightarrow \bar{K}^{*0} \eta$	0.4	< 1.5 (0.75 ± 0.75)	—	0.4	—	$\times 1380$
$B^- \rightarrow \rho^- \pi^0$	0.4	12 ± 2	8.5	—	—	$\times 86.4$
$\bar{B}^0 \rightarrow \rho^0 \pi^0$	0.4	1.8 ± 0.6	—	1.0	—	$\times 576$
$\bar{B}^0 \rightarrow \omega \pi^0$	0.4	< 1.2 (0.6 ± 0.6)	—	—	0.4	$\times 1730$
$B^- \rightarrow \rho^- \eta$	0.4	8.4 ± 1.7	6.0	—	—	$\times 123$
$\bar{B}^0 \rightarrow \rho^0 \eta$	0.4	< 1.5 (0.75 ± 0.75)	—	0.4	—	$\times 1380$
$\bar{B}^0 \rightarrow \omega \eta$	0.4	< 1.9 (0.95 ± 0.95)	—	—	0.5	$\times 1090$
Other rare B			13.7	10.7	4.0	$\times 3$

Table 3.2: Requirement on \mathcal{R} for each $q \cdot r$ bin.

$q \cdot r$ (or $ q \cdot r $)	$B^- \rightarrow \rho^- \gamma$	$\bar{B}^0 \rightarrow \rho^0 \gamma$	$\bar{B}^0 \rightarrow \omega \gamma$
-1 (0) — 0.250	0.995	0.990	0.995
$0.250 < q \cdot r \leq 0.500$	0.985	0.985	0.990
$0.500 < q \cdot r \leq 0.625$	0.975	0.975	0.990
$0.625 < q \cdot r \leq 0.750$	0.970	0.985	0.985
$0.750 < q \cdot r \leq 0.875$	0.950	0.955	0.980
$0.875 < q \cdot r \leq 1.000$	0.840	0.900	0.940
Maximum $ \cos \theta_{\text{hel}} $	0.75	0.70	0.80
Minimum $M(\text{"K"}\pi)$	0.92	0.95	
$N_S/\sqrt{N_B}$	2.55	2.21	2.99
signal efficiency	0.188	0.153	0.195
continuum efficiency	0.00090	0.00098	0.00078
total background efficiency	0.00188	0.00172	0.00132

Table 3.3: Summary of particle selection criteria.

Particle	Requirement
Photon	$1.8 \text{ GeV} < E_\gamma < 3.4 \text{ GeV}$ and $33^\circ < \theta_\gamma < 128^\circ$ (Barrel ECL) $L_{\pi^0}/(L_{\pi^0} + L_\gamma) < 0.4$ (“ π^0 veto”) and $L_\eta/(L_\eta + L_\gamma) < 0.5$ (“ η veto”) $E_9/E_{25} > 0.95$ (cluster transverse shape)
Charged tracks	$dr < 0.5 \text{ cm}$, $dz < 3 \text{ cm}$ and $p_T > 100 \text{ MeV}/c$ $L_\pi/(L_\pi + L_K) > 0.8$ for π^- from ρ^- $L_\pi/(L_\pi + L_K) > 0.85$ for π^\pm from ρ^0 and K^{*0} $L_\pi/(L_\pi + L_K) > 0.6$ for π^\pm from ω $L_\pi/(L_\pi + L_K) < 0.6$ for K^\pm remove tracks that form a good K_S via $K_S \rightarrow \pi^+\pi^-$ (“ K_S veto”) no electron ID and muon ID requirement
π^0	$E_\gamma > 50(100) \text{ MeV}$ for each photon in barrel(endcap) ECL $\cos\theta(\gamma\gamma) > 0.7$ $ M(\gamma\gamma) - m_{\pi^0} < 16 \text{ MeV}/c^2$
ρ^-	$0.62 \text{ GeV}/c^2 < M(\pi^-\pi^0) < 0.92 \text{ GeV}/c^2$ and $ \cos\theta_{\text{hel}} < 0.75$ $M(\text{“K”}\pi^0) > 0.92 \text{ GeV}/c^2$
ρ^0	$0.62 \text{ GeV}/c^2 < M(\pi^-\pi^0) < 0.92 \text{ GeV}/c^2$ and $ \cos\theta_{\text{hel}} < 0.70$ $M(\text{“K”}\pi^\pm) > 0.95 \text{ GeV}/c^2$
ω	$0.752 \text{ GeV}/c^2 < M(\pi^-\pi^+\pi^0) < 0.812 \text{ GeV}/c^2$ and $ \cos\theta_{\text{hel}} < 0.80$
K^{*-}	$0.817 \text{ GeV}/c^2 < M(K^-\pi^0) < 0.967 \text{ GeV}/c^2$ and $ \cos\theta_{\text{hel}} < 0.75$
\bar{K}^{*0}	$0.821 \text{ GeV}/c^2 < M(K^-\pi^+) < 0.971 \text{ GeV}/c^2$ and $ \cos\theta_{\text{hel}} < 0.70$
B fit region	$5.2 \text{ GeV}/c^2 < M_{\text{bc}}$ and $ \Delta E < 0.5 \text{ GeV}$
B signal region	$5.273 \text{ GeV}/c^2 < M_{\text{bc}} < 5.285 \text{ GeV}/c^2$ and $-0.08 \text{ GeV} < \Delta E < 0.1 \text{ GeV}$

Chapter 4

Fit Results and Systematic Errors

4.1 Signal Modeling

For each of the modes $B^- \rightarrow \rho^- \gamma$, $\bar{B}^0 \rightarrow \rho^0 \gamma$ and $\bar{B}^0 \rightarrow \omega \gamma$, we model the signal component as the product of an M_{bc} function and a ΔE function over the M_{bc} - ΔE fit region. The ΔE distribution is modeled with a Crystal Ball function [48] for all modes. For $\bar{B}^0 \rightarrow \rho^0 \gamma$, we use a Gaussian function $f_G(x) = 1/\sqrt{2\pi\sigma} \exp[-\frac{1}{2}(x - \mu)^2/\sigma^2]$ to model M_{bc} ; for the other two modes with a π^0 meson in the final state, we use a Crystal Ball function to model M_{bc} in order to accomodate tail on the lower-mass side of the peak.

The Crystal Ball function has the following form,

$$f_{CB}(x) = \begin{cases} A \exp\left[-\frac{1}{2} \frac{(x - \mu)^2}{\sigma^2}\right] & (\text{if } x \geq \mu + \alpha\sigma) \\ A e^{-\frac{\alpha^2}{2}} \left[1 - \frac{\alpha^2}{n} \left(1 - \frac{x - \mu}{\alpha\sigma}\right)\right]^{-n} & (\text{if } x < \mu + \alpha\sigma) \end{cases} \quad (4.1)$$

where σ and μ correspond to the width and mean of a Gaussian function that is used to model the lower side, and α and n are empirical parameters to model the higher side.

It is in general not so straightforward to obtain an optimal set of values for the α and

n parameters of the Crystal Ball function because many distinct choices give a very similar function shape. We use a fit to the $\bar{B}^0 \rightarrow \bar{K}^{*0}\gamma$ and $B^- \rightarrow K^{*-}\gamma$ data samples, despite their limited statistics and the existence of backgrounds. We consider three different sets of Crystal Ball function parameters, $(n_E, \alpha_E, \sigma_E, \mu_E)$ for ΔE of $\bar{B}^0 \rightarrow \bar{K}^{*0}\gamma$, $(n_{E0}, \alpha_{E0}, \sigma_{E0}, \mu_{E0})$ ΔE of $B^- \rightarrow K^{*-}\gamma$, and $(n_{M0}, \alpha_{M0}, \sigma_{M0}, \mu_{M0})$ for M_{bc} of $B^- \rightarrow K^{*-}\gamma$, extracted from the fit except for α_{M0} , which is set by hand. We extract the Gaussian parameters (σ_M, μ_M) for M_{bc} from the $\bar{B}^0 \rightarrow \bar{K}^{*0}\gamma$ sample. We use these shape parameters obtained from the $\bar{B}^0 \rightarrow \bar{K}^{*0}\gamma$ sample to model $\bar{B}^0 \rightarrow \rho^0\gamma$, and those from the $B^- \rightarrow K^{*-}\gamma$ sample to model $B^- \rightarrow \rho^-\gamma$ and $\bar{B}^0 \rightarrow \omega\gamma$.

4.2 Signal Efficiency

We use the above functional forms to fit the MC events and thereby evaluate the signal efficiency. Two issues arise here. The first is a poor fit quality — especially for the modes with a π^0 meson—when using the $K^*\gamma$ parameter values for the fitting functions, due to the Crystal Ball function not adequately modeling a distribution with multiple photons with different energies. (The Crystal Ball function is intended to model incomplete energy containment of a single photon in a calorimeter.) The second is the difference between the ΔE shapes of $B^- \rightarrow K^{*-}\gamma$ and $B^- \rightarrow \rho^-\gamma$ MC samples. We surmise that this is an artifact of the small number of events (10^4) of the $B^- \rightarrow K^{*-}\gamma$ MC sample, which is sufficient to obtain the efficiency with a one percent error but not enough to determine a unique set of parameters for the Crystal Ball function. Therefore, we allow α , σ and μ to float in all MC fits for the signal efficiency instead of fixing them from the $K^*\gamma$ fit. The fit results are given in Table 4.1. If we fix the shape from the $K^*\gamma$ sample, the χ^2/ndf value becomes much larger (and fit result looks very poor), but the efficiency changes by at most 1% for

the $\rho^-\gamma$ mode. We therefore include $\pm 1\%$ error in the MC efficiency error. We choose to float α instead of n or both since n tends to diverge to a very large value. We also add the continuum background MC events and off-resonance events of *all* five modes together, and add a continuum background component in the fit function. We do not include other B decay background components.

The entire fitting procedure is described in section 4.3 (p. 72). The fit results are summarized in Table 4.2, and shown in Figs. 4.1–4.2.

From this fit to the MC data, we extract the signal efficiency, taking into account all of the sub-decay branching fractions.

Systematic errors for this efficiency are taken from the standard Belle numbers as summarized in Table 4.3.

The combined systematic error on the π^0/η veto condition and flavor-tagging dependent likelihood ratio criteria is evaluated separately for the B^- mode ($B^- \rightarrow \rho^-\gamma$) and the \bar{B}^0 modes ($\bar{B}^0 \rightarrow \rho^0\gamma$ and $\bar{B}^0 \rightarrow \omega\gamma$). These variables are calculated from the properties of the decay products of the tagging B meson, and hence could be different for B^0 (tagging side of \bar{B}^0) vs B^+ (tagging side of B^-). We use the $B^- \rightarrow D^0\pi^-$ and $\bar{B}^0 \rightarrow D^+\pi^-$ data samples for the B^- and \bar{B}^0 modes, respectively. We analyze the data and MC events taken from the full-reconstruction sample and extract the signal yields from M_{bc} fits for the events with and without the set of requirements to calculate efficiencies. For each case, we calculate the ratio of data to MC efficiencies and take the quadratic sum of the deviation from unity and its statistical error as the systematic error of the combined requirements.

For the particle identification, we use Belle’s particle identification and misidentification efficiency table. Since we know that the PID efficiencies in data clearly deviate from those in MC, we make corrections to the total reconstruction efficiency. The results are summarized in Table 4.4.

We find the total signal efficiencies are between 3% and 5%. Note that the $\bar{B}^0 \rightarrow \rho^0\gamma$ efficiency is not much higher than that of $B^- \rightarrow \rho^-\gamma$ since we impose a tighter condition on $\bar{B}^0 \rightarrow \bar{K}^{*0}\gamma$ to further suppress this background.

4.3 Fitting

The results of this analysis are obtained from the following five fits to data. The fit region in the $M_{bc} - \Delta E$ plane is defined in section 4.1.

1. Fit the $B^- \rightarrow \rho^-\gamma$ events to extract $\mathcal{B}(B^- \rightarrow \rho^-\gamma)$.
2. Fit the $\bar{B}^0 \rightarrow \rho^0\gamma$ events to extract $\mathcal{B}(\bar{B}^0 \rightarrow \rho^0\gamma)$.
3. Fit the $\bar{B}^0 \rightarrow \omega\gamma$ events to extract $\mathcal{B}(\bar{B}^0 \rightarrow \omega\gamma)$.
4. Simultaneous fit of the three signal modes and two $\bar{B} \rightarrow \bar{K}^*\gamma$ modes to extract combined branching fractions for $\bar{B} \rightarrow \bar{K}^*\gamma$ and $\bar{B} \rightarrow (\rho, \omega)\gamma$, assuming isospin relation.
5. Simultaneous fit to the events to the same five modes to extract ratio of branching fractions $\mathcal{B}(\bar{B} \rightarrow (\rho, \omega)\gamma)/\mathcal{B}(\bar{B} \rightarrow \bar{K}^*\gamma)$, assuming isospin relation.

For the $K^*\gamma$ events, the fit is performed with the signal, continuum, and rare B decay background components. For the $\rho\gamma$ and $\omega\gamma$ events, the fit incorporates the signal, continuum, and five B decay background components ($K^*\gamma$, other $X_s\gamma$, $V\pi^0$, $V\eta$, and other rare B). The continuum background shape and scale are allowed to float independently for each mode. The shape of the $K^*\gamma$ background component in $\bar{B} \rightarrow (\rho, \omega)\gamma$ fits is always fixed according to the parameters obtained from the earlier fit to $K^*\gamma$ -enriched sample, and the scale is fixed in fits 1, 2 and 3 according to the branching fraction from the $K^*\gamma$ -enriched fit, or constrained in the simultaneous fits 4 and 5 according to the co-fitted size

of the $\bar{B} \rightarrow \bar{K}^* \gamma$ component. For the MC samples, we use only the signal and continuum components in a fit to a mixture of the signal and continuum MC events.

In simultaneous fits 4 and 5, we use the following isospin relations between charged and neutral B decays:

$$\mathcal{B}(\bar{B} \rightarrow \bar{K}^* \gamma) \equiv \mathcal{B}(B^- \rightarrow K^{*-} \gamma) = \frac{\tau_{B^+}}{\tau_{B^0}} \mathcal{B}(\bar{B}^0 \rightarrow \bar{K}^{*0} \gamma) \quad (4.2)$$

$$\mathcal{B}(\bar{B} \rightarrow (\rho, \omega) \gamma) \equiv \mathcal{B}(B^- \rightarrow \rho^- \gamma) = 2 \times \frac{\tau_{B^+}}{\tau_{B^0}} \mathcal{B}(\bar{B}^0 \rightarrow \rho^0 \gamma) = 2 \times \frac{\tau_{B^+}}{\tau_{B^0}} \mathcal{B}(\bar{B}^0 \rightarrow \omega \gamma) \quad (4.3)$$

where we use the lifetime ratio $\tau_{B^+}/\tau_{B^0} = 1.076 \pm 0.008$ from HFAG [52].

4.3.1 Fit parameters

In the fits, the following parameters are always fixed: number of B events (N_{BB}), efficiency correction factor (c), misidentification probability of background events as the $(\rho, \omega) \gamma$ events (c') and ARGUS function end-point (E_{beam}^*). The following parameters are always allowed to float: continuum ΔE slope (a), ARGUS shape parameter (ξ), and continuum background normalization N_{cont} . We perform extended unbinned maximum likelihood fits using the `roofit` [49, 50] program¹.

The fit functions (F) are defined as

$$\begin{aligned} F_{K^{*-}\gamma} = & N_{BB} \cdot [\mathcal{B}_{K^{*-}\gamma} \cdot \epsilon_{K^{*-}\gamma} \cdot c_\gamma \cdot c_{\text{trk}} \cdot c_{\pi^0} \cdot c_{\text{pid}} \cdot c_{\mathcal{R}} \cdot f_{\text{CB}}(\Delta E) \cdot f_{\text{CB}}(M_{\text{bc}}) \\ & + \sum \mathcal{B}_{\text{rare}} \cdot \epsilon'_{\text{rare}} \cdot f_{\text{rare}}(\Delta E, M_{\text{bc}})] + N_{\text{cont}} \cdot f_{\text{lin}}(\Delta E) \cdot f_{\text{ARGUS}}(M_{\text{bc}}) \end{aligned} \quad (4.4)$$

$$\begin{aligned} F_{\bar{K}^{*0}\gamma} = & N_{BB} \cdot [\mathcal{B}_{\bar{K}^{*0}\gamma} \cdot \epsilon_{\bar{K}^{*0}\gamma} \cdot c_\gamma \cdot c_{\text{trk}}^2 \cdot c_{\text{pid}} \cdot c_{\mathcal{R}} \cdot f_{\text{CB}}(\Delta E) \cdot f_{\text{G}}(M_{\text{bc}}) \\ & + \sum \mathcal{B}_{\text{rare}} \cdot \epsilon'_{\text{rare}} \cdot f_{\text{rare}}(\Delta E, M_{\text{bc}})] + N_{\text{cont}} \cdot f_{\text{lin}}(\Delta E) \cdot f_{\text{ARGUS}}(M_{\text{bc}}) \end{aligned} \quad (4.5)$$

¹The version 1.00.04 of `roofit` is used with version 3.10.01 of ROOT. We integrate the ARGUS function numerically since analytic integration fails for non-negative shape parameters.

$$\begin{aligned}
F_{\rho^- \gamma} = & N_{BB} \cdot \left[\mathcal{B}_{\rho^- \gamma} \cdot \epsilon_{\rho^- \gamma} \cdot c_{\gamma} \cdot c_{\text{trk}} \cdot c_{\pi^0} \cdot c_{\text{pid}} \cdot c_{\mathcal{R}} \cdot f_{\text{CB}}(\Delta E) \cdot f_{\text{CB}}(M_{\text{bc}}) \right. \\
& + \mathcal{B}_{K^{*-} \gamma} \cdot \epsilon'_{K^{*-} \gamma} \cdot c_{\text{misid}} \cdot f_{K^{*-} \gamma}(\Delta E, M_{\text{bc}}) \\
& + \mathcal{B}_{\rho^- \pi^0} \cdot \epsilon'_{\rho^- \pi^0} \cdot f_{\rho^- \pi^0}(\Delta E, M_{\text{bc}}) + \mathcal{B}_{\rho^- \eta} \cdot \epsilon'_{\rho^- \eta} \cdot f_{\rho^- \eta}(\Delta E, M_{\text{bc}}) \\
& \left. + \mathcal{B}_{X_s \gamma} \cdot \epsilon'_{X_s \gamma} \cdot f_{X_s \gamma}(\Delta E, M_{\text{bc}}) + \sum \mathcal{B}_{\text{rare}} \cdot \epsilon'_{\text{rare}} \cdot f_{\text{rare}}(\Delta E, M_{\text{bc}}) \right] \\
& + N_{\text{cont}} \cdot f_{\text{lin}}(\Delta E) \cdot f_{\text{ARGUS}}(M_{\text{bc}})
\end{aligned} \tag{4.6}$$

$$\begin{aligned}
F_{\rho^0 \gamma} = & N_{BB} \cdot \left[\mathcal{B}_{\rho^0 \gamma} \cdot \epsilon_{\rho^0 \gamma} \cdot c_{\gamma} \cdot c_{\text{trk}}^2 \cdot c_{\text{pid}} \cdot c_{\mathcal{R}} \cdot f_{\text{CB}}(\Delta E) \cdot f_G(M_{\text{bc}}) \right. \\
& + \mathcal{B}_{\bar{K}^{*0} \gamma} \cdot \epsilon'_{\bar{K}^{*0} \gamma} \cdot c_{\text{misid}} \cdot f_{\bar{K}^{*0} \gamma}(\Delta E, M_{\text{bc}}) \\
& + \mathcal{B}_{\rho^0 \pi^0} \cdot \epsilon'_{\rho^0 \pi^0} \cdot f_{\rho^0 \pi^0}(\Delta E, M_{\text{bc}}) + \mathcal{B}_{\rho^0 \eta} \cdot \epsilon'_{\rho^0 \eta} \cdot f_{\rho^0 \eta}(\Delta E, M_{\text{bc}}) \\
& \left. + \mathcal{B}_{X_s \gamma} \cdot \epsilon'_{X_s \gamma} \cdot f_{X_s \gamma}(\Delta E, M_{\text{bc}}) + \sum \mathcal{B}_{\text{rare}} \cdot \epsilon'_{\text{rare}} \cdot f_{\text{rare}}(\Delta E, M_{\text{bc}}) \right] \\
& + N_{\text{cont}} \cdot f_{\text{lin}}(\Delta E) \cdot f_{\text{ARGUS}}(M_{\text{bc}})
\end{aligned} \tag{4.7}$$

$$\begin{aligned}
F_{\omega \gamma} = & N_{BB} \cdot \left[\mathcal{B}_{\omega \gamma} \cdot \epsilon_{\omega \gamma} \cdot c_{\gamma} \cdot c_{\text{trk}}^2 \cdot c_{\pi^0} \cdot c_{\text{pid}} \cdot c_{\mathcal{R}} \cdot f_{\text{CB}}(\Delta E) \cdot f_{\text{CB}}(M_{\text{bc}}) \right. \\
& + \mathcal{B}_{K^{*-} \gamma} \cdot \epsilon'_{K^{*-} \gamma} \cdot c_{\text{misid}} \cdot f_{K^{*-} \gamma}(\Delta E, M_{\text{bc}}) \\
& + \mathcal{B}_{\omega \pi^0} \cdot \epsilon'_{\omega \pi^0} \cdot f_{\omega \pi^0}(\Delta E, M_{\text{bc}}) + \mathcal{B}_{\omega \eta} \cdot \epsilon'_{\omega \eta} \cdot f_{\omega \eta}(\Delta E, M_{\text{bc}}) \\
& \left. + \mathcal{B}_{X_s \gamma} \cdot \epsilon'_{X_s \gamma} \cdot f_{X_s \gamma}(\Delta E, M_{\text{bc}}) + \sum \mathcal{B}_{\text{rare}} \cdot \epsilon'_{\text{rare}} \cdot f_{\text{rare}}(\Delta E, M_{\text{bc}}) \right] \\
& + N_{\text{cont}} \cdot f_{\text{lin}}(\Delta E) \cdot f_{\text{ARGUS}}(M_{\text{bc}})
\end{aligned} \tag{4.8}$$

where $f_{\text{CB}}(\Delta E)$ and $f_G(M_{\text{bc}})$ are probability density functions (PDFs) for the signal component as defined in section 4.1, $f_{\text{lin}}(\Delta E)$ and $f_{\text{ARGUS}}(M_{\text{bc}})$ are PDFs for the continuum background component, and the other $f(\Delta E, M_{\text{bc}})$ functions are the PDFs for the corresponding background components that are modeled by using two-dimensional histograms. We include all fixed correction factors in the expression even if they are unity in order to vary them to calculate the systematic errors. In the expressions above, some of the mode-dependent labels are omitted for clarity: mode-dependent values are used for c_{pid} , c_{misid} ,

and each ϵ' ; two sets of n , α , σ and μ are used in the PDFs for the modes with and without a π^0 meson; two values of $c_{\mathcal{R}}$ are used for \bar{B}^0 and B^- modes.

In simultaneous fits 4 and 5, we replace the branching fractions as follows:

$$\begin{aligned}\mathcal{B}_{K^{*-}\gamma} &\rightarrow \mathcal{B}_{K^*\gamma}, & \mathcal{B}_{\bar{K}^{*0}\gamma} &\rightarrow \frac{1}{\tau_{B^0}/\tau_{B^+}} \mathcal{B}_{K^*\gamma}, \\ \mathcal{B}_{\rho^-\gamma} &\rightarrow \mathcal{B}_{(\rho,\omega)\gamma}, & \mathcal{B}_{\rho^0\gamma} &\rightarrow \frac{1}{2\tau_{B^0}/\tau_{B^+}} \mathcal{B}_{(\rho,\omega)\gamma}, \\ \mathcal{B}_{\omega\gamma} &\rightarrow \frac{1}{2\tau_{B^0}/\tau_{B^+}} \mathcal{B}_{(\rho,\omega)\gamma}.\end{aligned}\tag{4.9}$$

In the simultaneous fit 5, we further replace $\mathcal{B}_{(\rho,\omega)\gamma}$ with $r_{(\rho,\omega)\gamma} \times \mathcal{B}_{K^*\gamma}$. Common correction factors are used except for the mode-dependent c_{pid} and B charge dependent $c_{\mathcal{R}}$.

For fits 1, 2 and 3, the efficiency correction factors are multiplicative and are not varied when the systematic error is calculated. For simultaneous fits 4 and 5, we *do* vary them when the systematic error is calculated, since they are not linearly multiplicative in these fits.

4.4 Results

4.4.1 Fit results

Results are given in Fig. 4.3 for the signal slice (the projection on the M_{bc} axis for events in the narrow signal slice of ΔE , or vice versa) and in Fig. 4.4 for the entire fit region. Results for simultaneous fit 4 are given in Fig. 4.5 for the signal slices.

In order to evaluate the systematic errors due to the fixed parameters in the fit, we vary each of them by $\pm 1\sigma$ and repeat the fit, and take the deviation of the central value from the nominal one as the systematic error. We use the quadratic sum of all positive (negative) deviations as the total positive (negative) error.

From the individual fits, we obtain the following branching fractions:

$$\mathcal{B}(B^- \rightarrow K^{*-}\gamma) = (40.2^{+3.0}_{-2.9}) \times 10^{-6} \quad (4.10)$$

$$\mathcal{B}(\bar{B}^0 \rightarrow \bar{K}^{*0}\gamma) = (38.4^{+1.5}_{-1.4}) \times 10^{-6} \quad (4.11)$$

$$\mathcal{B}(B^- \rightarrow \rho^-\gamma) = (0.55^{+0.42+0.09}_{-0.36-0.08}) \times 10^{-6} \quad (1.6\sigma \text{ significance}) \quad (4.12)$$

$$\mathcal{B}(\bar{B}^0 \rightarrow \rho^0\gamma) = (1.25^{+0.37+0.07}_{-0.33-0.06}) \times 10^{-6} \quad (5.2\sigma \text{ significance}) \quad (4.13)$$

$$\mathcal{B}(\bar{B}^0 \rightarrow \omega\gamma) = (0.56^{+0.34+0.05}_{-0.27-0.10}) \times 10^{-6} \quad (2.3\sigma \text{ significance}) \quad (4.14)$$

where the first and second errors are statistical and systematic, respectively. The systematic error is a quadratic sum of the fitting systematic error and errors on the efficiencies and the number of $B\bar{B}$ events. We do not calculate the systematic errors for $\bar{B} \rightarrow \bar{K}^*\gamma$ modes since they have additional systematic error sources, and the $K^*\gamma$ systematic error is not needed for the $b \rightarrow d\gamma$ analysis. The fitted number of events for each component is listed in the upper part of Table 4.5.

From simultaneous fit 4, we obtain the following results:

$$\mathcal{B}(\bar{B} \rightarrow \bar{K}^*\gamma) = (41.1^{+1.4}_{-1.3}) \times 10^{-6} \quad (4.15)$$

$$\mathcal{B}(\bar{B} \rightarrow (\rho, \omega)\gamma) = (1.32^{+0.34+0.10}_{-0.31-0.09}) \times 10^{-6} \quad (5.2\sigma \text{ significance}) \quad (4.16)$$

The number of events for each component is listed in the lower part of Table 4.5. The branching fraction results appear in the lower part of the Table 4.6. Note that the central value of $\mathcal{B}(\bar{B} \rightarrow \bar{K}^*\gamma)$ here is larger than the central value of $\mathcal{B}(B^- \rightarrow K^{*-}\gamma)$ since the central value for the normal mode is multiplied by τ_{B^+}/τ_{B^0} .

The result of simultaneous fit 5 is

$$\mathcal{B}(\bar{B} \rightarrow (\rho, \omega)\gamma)/\mathcal{B}(\bar{B} \rightarrow \bar{K}^*\gamma) = 0.032 \pm 0.008 \pm 0.002. \quad (4.17)$$

We also measure the ratio of charged and neutral B decays separately to examine their statistical powers. At this moment, the separate results have little statistical meaning; however, they will be useful to evaluate isospin asymmetry in the future. The results are as follows:

$$\mathcal{B}(B^- \rightarrow \rho^- \gamma) / \mathcal{B}(B^- \rightarrow K^{*-} \gamma) = 0.014_{-0.009}^{+0.011} \pm 0.002 \quad (4.18)$$

$$\mathcal{B}(\bar{B}^0 \rightarrow \rho^0 \gamma) / \mathcal{B}(\bar{B}^0 \rightarrow \bar{K}^{*0} \gamma) = 0.033_{-0.009}^{+0.010} \pm 0.001. \quad (4.19)$$

4.4.2 Systematic errors

The systematic errors are given in Tables 4.7–4.9. The tables list the varied parameter, resulting shift in the branching fraction and the resulting significance. The total positive (negative) systematic error is the quadratic sum of the positive (negative) deviations.

In Table 4.7, systematic errors due to the signal shape model are listed. We list the parameters for the modes with and without π^0 separately. We do not list n_{M0} for M_{bc} , which is constrained to be equal to the value for ΔE . We do not list α_{E0} and μ_{E0} for the simultaneous fit, which are constrained to be equal to α_E and μ_E , respectively. In general, the errors for the parameters with a π^0 meson are larger than those without. The simultaneous fit error for σ_E is very small; we have not identified a particular reason for this.

In Table 4.8, the systematic errors due to the background components are listed. It seems the errors are rather small.

In Table 4.9, systematic errors due to the efficiency, an additional systematic error due to the ARGUS shape parameter for the $\omega\gamma$ mode, and the total systematic errors are listed. The largest error arises from the π^0 efficiency uncertainty. The ARGUS shape parameter systematic error is introduced by hand since the $\bar{B}^0 \rightarrow \omega\gamma$ fit result shows a rather steep

continuum M_{bc} shape with a positive ξ value. The value itself is 2σ away from zero and might be due to statistical fluctuation of the background distribution: from a test with MC samples, we see that the ARGUS function tends to become steeper and ξ can be positive with a tighter \mathcal{R} requirement. This is the largest error in the $\overline{B}^0 \rightarrow \omega\gamma$ fit; it is not the largest in the simultaneous fit, yet has a large impact in the significance there.

4.4.3 Significance calculation

The statistical significance is calculated as

$$\mathcal{S}_{\text{stat}} = \sqrt{2(\log \mathcal{L}_0 - \log \mathcal{L}_{\text{max}})}, \quad (4.20)$$

where \mathcal{L}_0 and \mathcal{L}_{max} are the likelihoods of the fit when the branching fraction is set to zero and likelihood is maximized, respectively. This expression is valid if the systematic error is neglected. The significance \mathcal{S} incorporates the systematic error. No well defined method is prescribed to incorporate the systematic error in the significance calculation. The following four methods have been used in past Belle analyses:

- “Lowest” — vary each fixed parameter, recalculate $\mathcal{S}_{\text{stat}}$ and take the lowest value.
- “All-change” — vary all fixed parameters together in the direction that lowers the significance, and take the resulting value of $\mathcal{S}_{\text{stat}}$.
- “Subtraction” — vary each fixed parameter, recalculate $\mathcal{S}'_{\text{stat}}$, calculate the quadratic sum of $\mathcal{S}'_{\text{stat}} - \mathcal{S}_{\text{stat}}$ if the significance is lower, and subtract this sum from the original $\mathcal{S}_{\text{stat}}$.
- “Inflation” — take $\sqrt{-2(\log \mathcal{L}(+1\sigma_{\text{syst}}) - \log \mathcal{L}_{\text{max}})}$

In this analysis, we introduce a new method that we call “convolution.” Here, we assume the systematic error follows a Gaussian distribution, and convolve it with the likelihood distribution $\mathcal{L}(x)$ from MINUIT [51] (exponential of the log-likelihood from MINUIT). Since one has to perform a fit to obtain the log-likelihood, we extract log-likelihood points and then interpolate the points in between. The convolution,

$$\mathcal{L}'(x) = \frac{1}{\sqrt{2\pi}\sigma} \int_{-\infty}^{+\infty} \mathcal{L}(t) e^{-(t-x)^2/(2\sigma^2)} dt, \quad (4.21)$$

where x is the branching fraction or the ratio for which the likelihood is evaluated and σ is the systematic error, is performed by a numerical integration, and then $\mathcal{L}'(0)$ and \mathcal{L}'_{\max} is calculated. This method is well defined and there is no assumption other than that the statistical and systematic errors are uncorrelated.

This method can be extended to any systematic error distribution. In fact, we use an asymmetric Gaussian distribution in this analysis to model the asymmetric systematic error. The likelihood curves are shown in Fig. 4.6, and a numerical comparison among these methods is given in Table 4.10.

As seen in the table, no two methods are equivalent. The convolution method gives the smallest shift for the $\rho^-\gamma$ and $\rho^0\gamma$ modes since the relative size of the systematic error is small. This is understandable since this method corresponds to a quadratic sum of the statistical and systematic errors while the others use, in general, a linear change. For the $\omega\gamma$ mode, the methods give similar results since one systematic error dominates. For the simultaneous fit, the “convolution” shift is larger than for the “lowest” method and smaller than the “all-change” method.

The significance values for the simultaneous fit for the branching fraction and the ratio are slightly different, since in the branching fraction measurement, we cannot simply disentangle some of the systematic error sources that should be irrelevant to the significance.

Therefore, we take the significance of the ratio for the nominal result.

4.4.4 Plots for mass and helicity angle

We examine the $\pi\pi(\pi)$ mass and helicity angle distributions for the events that remain in the signal box. We generate histograms of the signal, continuum and all B decay background MC samples for the wide region without the likelihood ratio requirement, normalize them to the yields in the signal box, and overlay each histogram to the data histogram. The distributions are given in Fig. 4.7 for individual fit results. All distributions are consistent with the sum of the signal and background components.

For the mass distribution, events are concentrated around the ρ and ω mass peaks as expected. The $\pi^+\pi^-$ distribution for $\rho^0\gamma$ (and to a lesser extent the $\pi^-\pi^0$ for $\rho^-\gamma$) is distorted due to the $M("K''\pi)$ requirement.

With the limited statistics, there seem to be no apparent inconsistencies in the distributions. The histograms entries are overshooting the sum of the components, because we find more events in the ΔE - M_{bc} signal box than the sum of the fit components.

Table 4.1: MC signal ΔE shape parameters.

	n	α	σ (MeV/ c^2)	μ (MeV/ c^2)
$B^- \rightarrow K^{*-} \gamma$	8.7 (fixed)	0.50 ± 4.37	38.0 ± 12.4	-3.2 ± 168.3
$\bar{B}^0 \rightarrow \bar{K}^{*0} \gamma$	8.7	0.50 ± 4.37	32.5 ± 8.1	3.6 ± 168.3
$B^- \rightarrow \rho^- \gamma$	8.7 (fixed)	0.50 ± 4.37	38.0 ± 12.4	-3.2 ± 168.3
$\bar{B}^0 \rightarrow \rho^0 \gamma$	8.7 (fixed)	0.50 ± 4.37	32.5 ± 8.1	3.6 ± 168.3
$\bar{B}^0 \rightarrow \omega \gamma$	8.7 (fixed)	0.50 ± 4.37	38.0 ± 12.4	-3.2 ± 168.3

Table 4.2: Summary of the signal shape parameters.

Mode	Variable	Data Value		MC Value			
$\overline{B}^0 \rightarrow \overline{K}^{*0}\gamma$	M_{bc}	μ	5279.8 ± 0.1	MeV/c^2	5279.4 ± 8.4	MeV/c^2	
		σ	2.70 ± 0.08	MeV/c^2	2.77 ± 0.82	MeV/c^2	
	ΔE	μ	7.9 ± 2.2	MeV	3.6 ± 168.3	MeV	
		σ	$39.4^{+1.7}_{-1.6}$	MeV	32.5 ± 8.1	MeV	
		α	0.65		0.50 ± 4.37		
		n	5.0		8.7		
	$B^- \rightarrow K^{*-}\gamma$	M_{bc}	μ	5279.0 ± 0.2	MeV/c^2	5279.1 ± 8.4	MeV/c^2
			σ	$3.09^{+0.21}_{-0.20}$	MeV/c^2	3.23 ± 1.24	MeV/c^2
		α	1.50	(fixed)	1.5	(fixed)	
		n	5.0	(fixed)	8.70	(fixed)	
ΔE		μ	$6.8^{+5.4}_{-5.5}$	MeV	-3.2 ± 168.3	MeV	
		σ	$49.4^{+4.2}_{-3.9}$	MeV	38.0 ± 12.4	MeV	
		α	0.65		0.50 ± 4.37		
		n	5.0	(fixed)	8.7	(fixed)	

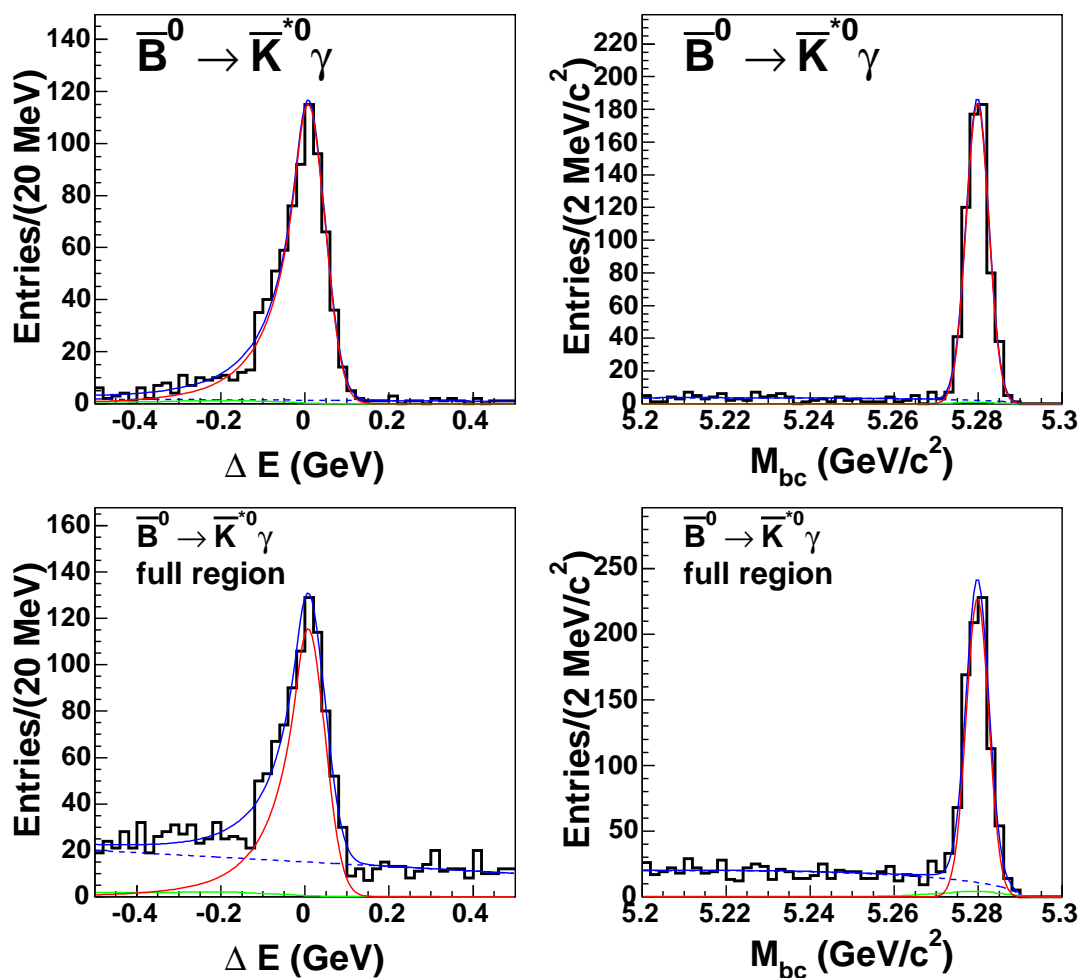


Figure 4.1: Fit results for $\bar{B}^0 \rightarrow \bar{K}^{*0} \gamma$. From top to bottom, projection to the signal slice, to the entire wide region are shown (Labels: $B \rightarrow K^* \gamma$ signal- red, rare B background- green and continuum background- blue (dotted)).

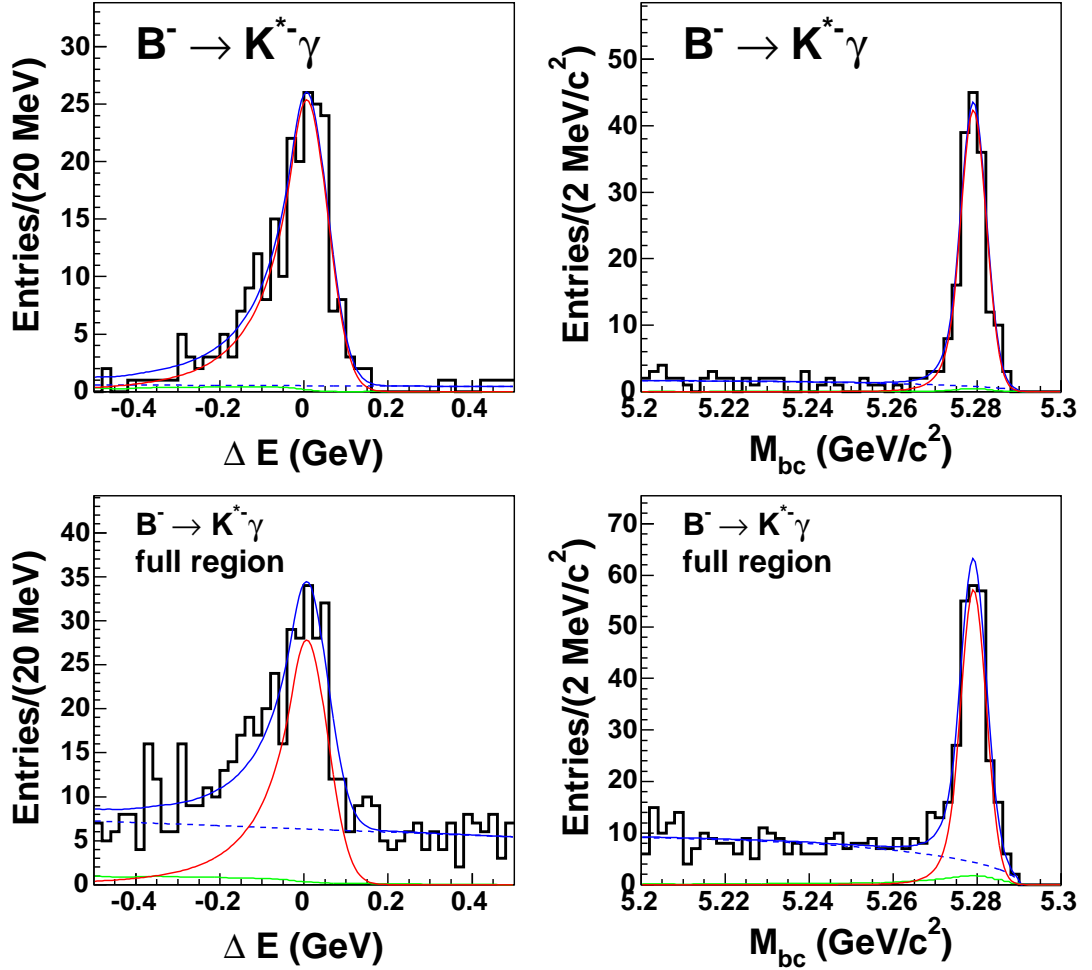


Figure 4.2: Fit results for $B^- \rightarrow K^{*-}\gamma$. From top to bottom, projection to the signal slice, to the entire wide region are shown (Labels: $B \rightarrow K^*\gamma$ signal- red, rare B background- green and continuum background- blue (dotted)).

Table 4.3: Summary of efficiency systematic errors.

Source	Relevant modes	Fractional error (%)	Ref.
Photon	all	2.2	Belle note 499 [59]
1-Track	$K^{*-}\gamma, \rho^-\gamma$	1.0	Belle note 621 [58]
2-Track	$\bar{K}^{*0}\gamma, \rho^0\gamma, \omega\gamma$	2.0	Belle note 621 [58]
π^0	$K^{*-}\gamma, \rho^-\gamma, \omega\gamma$	4.6	Belle note 645 [60]
Particle-id	all	(see Table 4.4)	
Likelihood etc.	$K^{*-}\gamma, \rho^-\gamma$	3.5	this analysis
	$\bar{K}^{*0}\gamma, \rho^0\gamma, \omega\gamma$	2.5	this analysis

Table 4.4: Summary of corrections on the particle identification efficiencies and total efficiencies including the systematic errors in Table 4.3.

Mode	corr. per track	total corr.	total eff.(%)
$B^- \rightarrow K^{*-}\gamma$ fake		1.128 ± 0.170	1.128 ± 0.170
$\bar{B}^0 \rightarrow \bar{K}^{*0}\gamma$ fake		1.133 ± 0.150	1.133 ± 0.150
$B^- \rightarrow K^{*-}\gamma$	0.9988 ± 0.0103 (K)	0.9988 ± 0.0103	1.47 ± 0.09
$\bar{B}^0 \rightarrow \bar{K}^{*0}\gamma$	0.9979 ± 0.0102 (K)	0.9558 ± 0.0166	5.20 ± 0.34
$B^- \rightarrow \rho^-\gamma$	0.9309 ± 0.0070 (π)	0.9309 ± 0.0070	3.86 ± 0.23
$\bar{B}^0 \rightarrow \rho^0\gamma$	0.9310 ± 0.0071 (π)	0.8668 ± 0.0131	4.30 ± 0.28
$\bar{B}^0 \rightarrow \omega\gamma$	0.9579 ± 0.0072 (π)	0.9175 ± 0.0123	2.61 ± 0.21

Table 4.5: Signal yields in the wide region (Numbers in the parenthesis are for the signal box) from the individual fits and the simultaneous fit.

From individual fits 1, 2 and 3							
	signal	cont.	$K^*\gamma$	$X_s\gamma$	$V\pi^0$	$V\eta$	rare B
$K^{*-}\gamma$	231 (156)	317 (5)					22.5 (2.0)
$\bar{K}^{*0}\gamma$	770 (621)	751 (12)					45.3 (3.7)
$\rho^-\gamma$	8.5 (5.7)	503 (6.6)	5.8 (1.7)	58.9 (1.2)	8.5 (1.6)	6.0 (0.5)	13.7 (0.3)
$\rho^0\gamma$	20.7 (16.7)	454 (6.0)	6.9 (2.1)	23.5 (0.6)	1.0 (0.3)	0.4 (0.0)	10.7 (0.3)
$\omega\gamma$	5.7 (3.9)	120 (1.0)	0.7 (0.1)	14.9 (0.6)	0.4 (0.1)	0.5 (0.1)	4.0 (0.1)
From the simultaneous fit 4 and 5							
	signal	cont.	$K^*\gamma$	$X_s\gamma$	$V\pi^0$	$V\eta$	rare B
$K^{*-}\gamma$	236 (159)	317 (5)					22.5 (2.0)
$\bar{K}^{*0}\gamma$	766 (617)	751 (12)					45.3 (3.7)
$\rho^-\gamma$	20.2 (13.7)	498 (6.4)	5.7 (1.7)	58.9 (1.2)	8.5 (1.6)	6.0 (0.5)	13.7 (0.3)
$\rho^0\gamma$	10.2 (8.2)	459 (6.2)	6.8 (2.0)	23.5 (0.6)	1.0 (0.3)	0.4 (0.0)	10.7 (0.3)
$\omega\gamma$	6.3 (4.2)	120 (1.0)	0.7 (0.1)	14.9 (0.6)	0.4 (0.1)	0.5 (0.1)	4.0 (0.1)

Table 4.6: Signal yields, efficiency, branching fraction and significance.

Mode	Signal Yield	efficiency (%)	\mathcal{B} ($\times 10^{-6}$)	signif.
$B^- \rightarrow K^{*-}\gamma$	231	1.47 ± 0.09	$40.2^{+3.0}_{-2.9}$	—
$B^0 \rightarrow K^{*0}\gamma$	770	5.20 ± 0.34	$38.4^{+1.5}_{-1.4}$	—
$B^- \rightarrow \rho^-\gamma$	8.5	3.86 ± 0.23	$0.55^{+0.42+0.09}_{-0.36-0.08}$	1.5
$\bar{B}^0 \rightarrow \rho^0\gamma$	20.7	4.30 ± 0.28	$1.25^{+0.37+0.07}_{-0.33-0.06}$	5.2
$\bar{B}^0 \rightarrow \omega\gamma$	5.7	2.61 ± 0.21	$0.56^{+0.34+0.05}_{-0.27-0.10}$	2.2
$\bar{B} \rightarrow \bar{K}^*\gamma$			$41.1^{+1.4}_{-1.3}$	
$\bar{B} \rightarrow (\rho, \omega)\gamma$			$1.32^{+0.34+0.10}_{-0.31-0.09}$	5.2

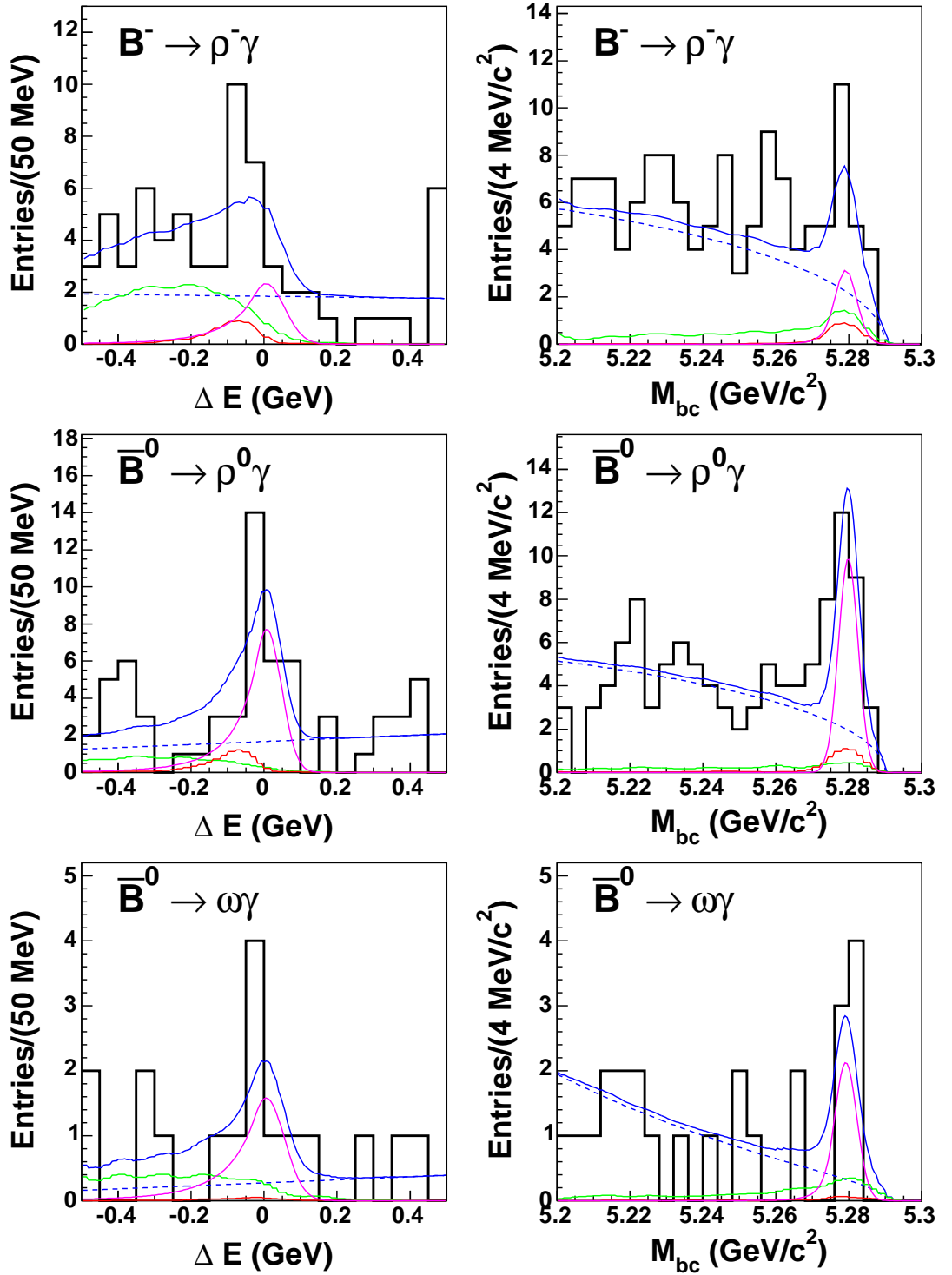


Figure 4.3: Projection to the signal slice of the individual fit results for the $B^- \rightarrow \rho^- \gamma$, $\bar{B}^0 \rightarrow \rho^0 \gamma$ and $\bar{B}^0 \rightarrow \omega \gamma$ modes (Labels: Signal- purple, $B \rightarrow K^* \gamma$ background- red, rare B background- green and continuum background- blue (dotted)).

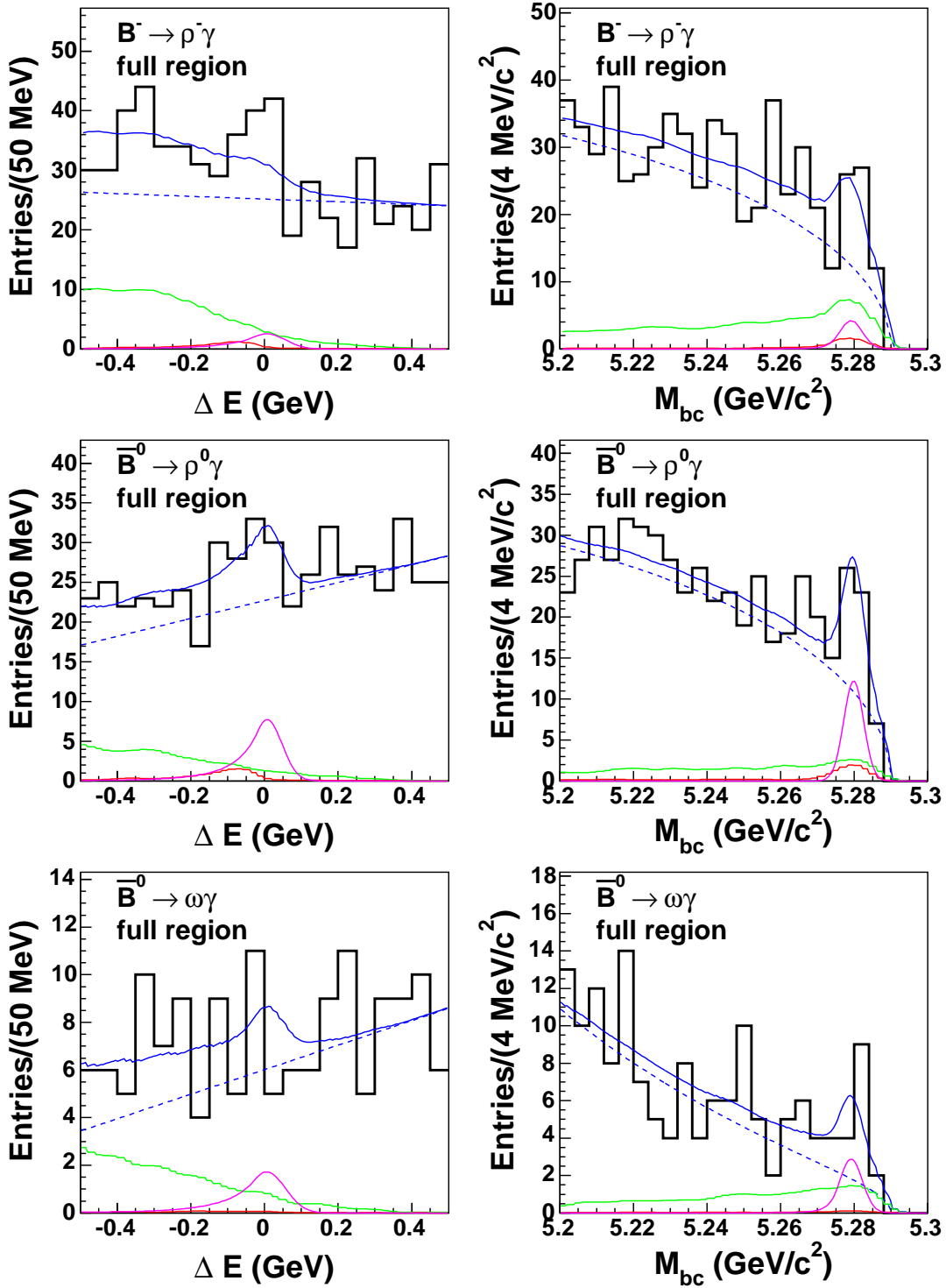


Figure 4.4: Projection to the fit region of the individual fit results for the $B^- \rightarrow \rho^- \gamma$, $\bar{B}^0 \rightarrow \rho^0 \gamma$ and $\bar{B}^0 \rightarrow \omega \gamma$ modes (Labels: Signal- purple, $B \rightarrow K^* \gamma$ background- red, rare B background- green and continuum background- blue (dotted)).

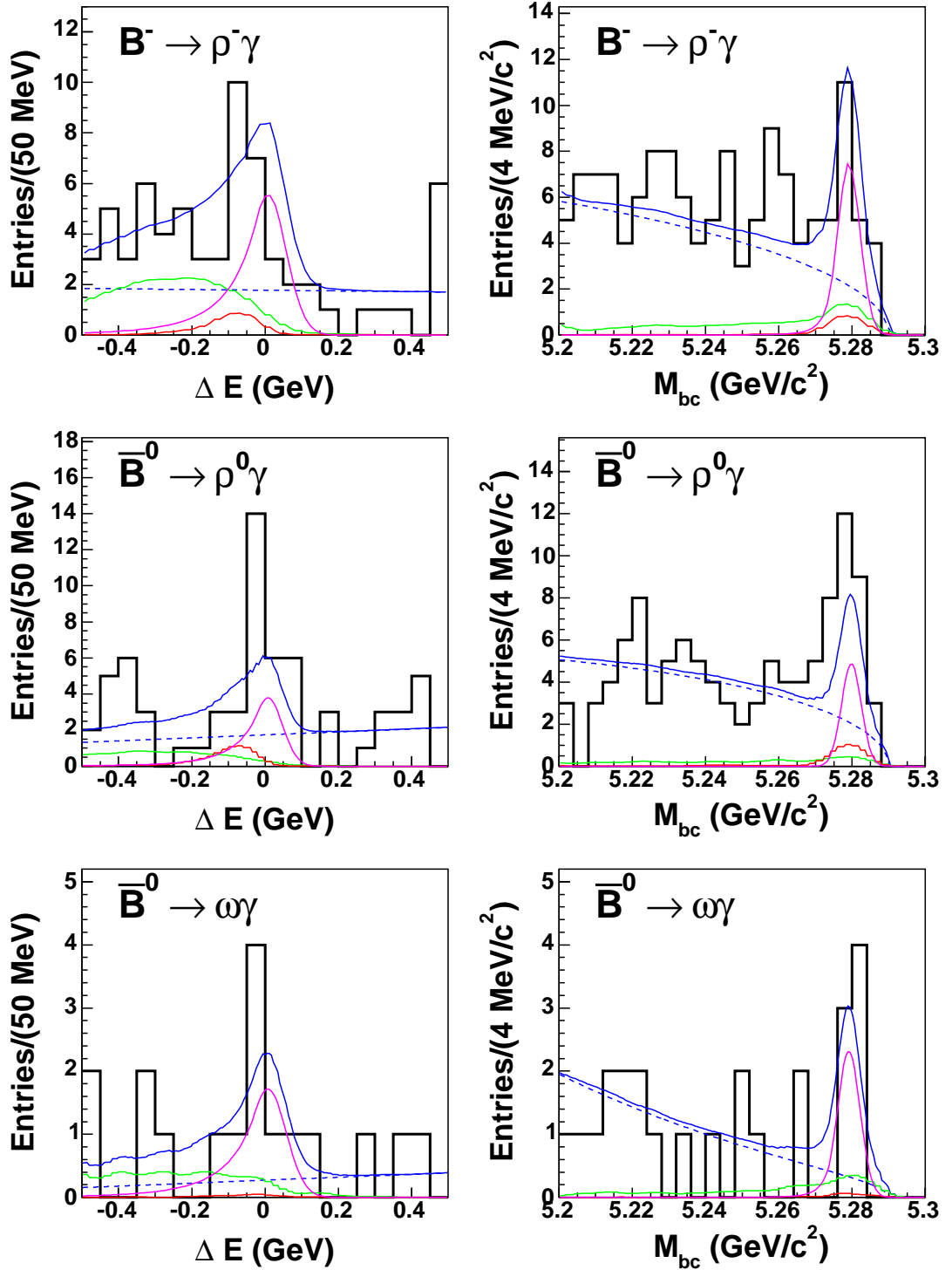


Figure 4.5: Projection to the signal slice of the simultaneous fit results to the five modes.

Table 4.7: Fitting systematic errors on ΔE and M_{bc} signal modeling.

Parameter	$\rho^- \gamma$		$\rho^0 \gamma$		$\omega \gamma$		simultaneous		
	$\delta\mathcal{B}(10^{-6})$	sig.	$\delta\mathcal{B}(10^{-6})$	sig.	$\delta\mathcal{B}(10^{-6})$	sig.	$\delta\mathcal{B}(10^{-6})$	sig.	
ΔE with π^0									
n_{E0}	+1 σ	-0.016	1.59	—	—	-0.008	2.65	—	—
n_{E0}	-1 σ	0.020	1.62	—	—	0.010	2.63	—	—
α_{E0}	+1 σ	-0.020	1.57	—	—	-0.005	2.65	—	—
α_{E0}	-1 σ	0.016	1.62	—	—	0.004	2.63	—	—
σ_{E0}	+1 σ	0.030	1.63	—	—	0.007	2.61	0.032	5.46
σ_{E0}	-1 σ	-0.027	1.56	—	—	-0.007	2.66	-0.025	5.40
μ_{E0}	+1 σ	-0.032	1.53	—	—	-0.006	2.62	—	—
μ_{E0}	-1 σ	0.029	1.67	—	—	0.004	2.65	—	—
M_{bc} with π^0									
α_{M0}	+1 σ	-0.020	1.59	—	—	-0.009	2.65	-0.025	5.41
α_{M0}	-1 σ	0.038	1.64	—	—	0.013	2.61	0.043	5.47
σ_{M0}	+1 σ	0.015	1.61	—	—	0.004	2.61	0.019	5.44
σ_{M0}	-1 σ	-0.017	1.60	—	—	-0.007	2.66	-0.019	5.42
μ_{M0}	+1 σ	0.009	1.63	—	—	0.013	2.70	0.010	5.48
μ_{M0}	-1 σ	-0.011	1.57	—	—	-0.013	2.57	-0.009	5.38
ΔE without π^0									
n_E	+1 σ	—	—	-0.013	5.25	—	—	-0.020	5.43
n_E	-1 σ	—	—	0.020	5.24	—	—	0.028	5.43
α_E	+1 σ	—	—	-0.008	5.27	—	—	-0.015	5.44
α_E	-1 σ	—	—	0.010	5.22	—	—	0.014	5.42
σ_E	+1 σ	—	—	0.010	5.22	—	—	0.001	5.40
σ_E	-1 σ	—	—	-0.009	5.26	—	—	0.001	5.46
μ_E	+1 σ	—	—	-0.001	5.23	—	—	-0.009	5.39
μ_E	-1 σ	—	—	0.003	5.26	—	—	0.012	5.47
M_{bc} without π^0									
σ_M	+1 σ	—	—	0.015	5.25	—	—	0.005	5.42
σ_M	-1 σ	—	—	-0.012	5.24	—	—	-0.002	5.44
μ_M	+1 σ	—	—	-0.002	5.23	—	—	-0.001	5.42
μ_M	-1 σ	—	—	0.005	5.26	—	—	0.004	5.44

Table 4.8: Fitting systematic errors on B backgrounds.

Parameter		$\rho^- \gamma$		$\rho^0 \gamma$		$\omega \gamma$		simultaneous		
		$\delta\mathcal{B}$	sig.	$\delta\mathcal{B}$	sig.	$\delta\mathcal{B}$	sig.	$\delta\mathcal{B}$	sig.	
B backgrounds										
$B^- \rightarrow K^{*-} \gamma$	$+1\sigma$	-0.001	1.60	—	—	—	—	—	—	
$B^- \rightarrow K^{*-} \gamma$	-1σ	-0.001	1.60	—	—	—	—	—	—	
$\bar{B}^0 \rightarrow \bar{K}^{*0} \gamma$	$+1\sigma$	—	—	0.002	5.25	0.000	2.64	—	—	
$\bar{B}^0 \rightarrow \bar{K}^{*0} \gamma$	-1σ	—	—	0.002	5.25	-0.000	2.64	—	—	
$K^{*-} \gamma$ fake	$+1\sigma$	-0.029	1.52	—	—	—	—	-0.010	5.39	
$K^{*-} \gamma$ fake	-1σ	0.030	1.69	—	—	—	—	0.014	5.48	
$\bar{K}^{*0} \gamma$ fake	$+1\sigma$	—	—	-0.012	5.18	—	—	-0.009	5.39	
$\bar{K}^{*0} \gamma$ fake	-1σ	—	—	0.016	5.32	—	—	0.012	5.48	
$B \rightarrow X_s \gamma$	$+1\sigma$	0.004	1.61	0.003	5.25	0.010	2.70	0.009	5.47	
$B \rightarrow X_s \gamma$	-1σ	-0.007	1.59	0.000	5.24	-0.014	2.56	-0.010	5.38	
$B^- \rightarrow \rho^- \pi^0$	$+1\sigma$	-0.033	1.51	—	—	—	—	-0.012	5.38	
$B^- \rightarrow \rho^- \pi^0$	-1σ	0.033	1.70	—	—	—	—	0.016	5.49	
$B^- \rightarrow \rho^- \eta$	$+1\sigma$	-0.013	1.57	—	—	—	—	-0.005	5.41	
$B^- \rightarrow \rho^- \eta$	-1σ	0.013	1.63	—	—	—	—	0.008	5.45	
$\bar{B}^0 \rightarrow \rho^0 \pi^0$	$+1\sigma$	—	—	-0.005	5.21	—	—	-0.004	5.41	
$\bar{B}^0 \rightarrow \rho^0 \pi^0$	-1σ	—	—	0.009	5.28	—	—	0.007	5.46	
$\bar{B}^0 \rightarrow \rho^0 \eta$	$+1\sigma$	—	—	-0.002	5.24	—	—	-0.000	5.43	
$\bar{B}^0 \rightarrow \rho^0 \eta$	-1σ	—	—	0.007	5.26	—	—	0.003	5.44	
$\bar{B}^0 \rightarrow \omega \pi^0$	$+1\sigma$	—	—	—	—	-0.016	2.55	-0.007	5.39	
$\bar{B}^0 \rightarrow \omega \pi^0$	$+1\sigma$	—	—	—	—	0.016	2.74	0.009	5.48	
$\bar{B}^0 \rightarrow \omega \eta$	$+1\sigma$	—	—	—	—	-0.011	2.60	-0.004	5.41	
$\bar{B}^0 \rightarrow \omega \eta$	$+1\sigma$	—	—	—	—	0.012	2.69	0.007	5.46	
Rare B	$+1\sigma$	0.004	1.61	0.005	5.24	0.013	2.69	0.010	5.45	
Rare B	-1σ	-0.014	1.57	-0.008	5.26	-0.033	2.51	-0.023	5.38	
$\frac{\tau_{B^+}}{\tau_{B^0}}$	$+1\sigma$	—	—	—	—	—	—	0.005	5.43	
$\frac{\tau_{B^+}}{\tau_{B^0}}$	-1σ	—	—	—	—	—	—	-0.001	5.44	

Table 4.9: Fitting systematic errors on efficiencies and the total systematic errors.

Parameter		$\rho^- \gamma$		$\rho^0 \gamma$		$\omega \gamma$		simultaneous	
		$\delta\mathcal{B}$	sig.	$\delta\mathcal{B}$	sig.	$\delta\mathcal{B}$	sig.	$\delta\mathcal{B}$	sig.
Photon	+1 σ	-0.012	—	-0.025	—	-0.012	—	—	—
Photon	-1 σ	0.012	—	0.030	—	0.013	—	—	—
Tracking	+1 σ	-0.005	—	-0.023	—	-0.011	—	-0.013	5.45
Tracking	-1 σ	0.004	—	0.027	—	0.012	—	0.017	5.41
π^0	+1 σ	-0.024	—	—	—	-0.025	—	-0.047	5.40
π^0	-1 σ	0.026	—	—	—	0.027	—	0.052	5.47
K/π id. (K^{*-})	+1 σ	—	—	—	—	—	—	0.003	5.43
K/π id. (K^{*-})	-1 σ	—	—	—	—	—	—	0.001	5.43
K/π id. (\bar{K}^{*0})	+1 σ	—	—	—	—	—	—	0.004	5.44
K/π id. (\bar{K}^{*0})	-1 σ	—	—	—	—	—	—	-0.001	5.42
K/π id. (ρ^-)	+1 σ	-0.004	—	—	—	—	—	-0.004	5.43
K/π id. (ρ^-)	-1 σ	0.003	—	—	—	—	—	0.007	5.44
K/π id. (ρ^0)	+1 σ	—	—	-0.017	—	—	—	-0.001	5.45
K/π id. (ρ^0)	-1 σ	—	—	0.021	—	—	—	0.004	5.42
K/π id. (ω)	+1 σ	—	—	—	—	-0.007	—	-0.003	5.43
K/π id. (ω)	-1 σ	—	—	—	—	-0.007	—	-0.003	5.43
$\mathcal{R}\text{-}q \cdot r$ (B^-)	+1 σ	-0.019	—	—	—	—	—	-0.024	5.41
$\mathcal{R}\text{-}q \cdot r$ (B^-)	-1 σ	0.020	—	—	—	—	—	0.027	5.46
$\mathcal{R}\text{-}q \cdot r$ (\bar{B}^0)	+1 σ	—	—	-0.029	—	-0.014	—	-0.008	5.47
$\mathcal{R}\text{-}q \cdot r$ (\bar{B}^0)	-1 σ	—	—	0.034	—	0.015	—	0.011	5.40
ϵ^{MC} ($K^{*-}\gamma$)	+1 σ	—	—	—	—	—	—	0.002	5.44
ϵ^{MC} ($K^{*-}\gamma$)	-1 σ	—	—	—	—	—	—	0.001	5.43
ϵ^{MC} ($\bar{K}^{*0}\gamma$)	+1 σ	—	—	—	—	—	—	0.003	5.44
ϵ^{MC} ($\bar{K}^{*0}\gamma$)	-1 σ	—	—	—	—	—	—	-0.001	5.43
ϵ^{MC} ($\rho^-\gamma$)	+1 σ	-0.005	—	—	—	—	—	-0.006	5.42
ϵ^{MC} ($\rho^-\gamma$)	-1 σ	0.004	—	—	—	—	—	0.009	5.44
ϵ^{MC} ($\rho^0\gamma$)	+1 σ	—	—	-0.010	—	—	—	-0.001	5.44
ϵ^{MC} ($\rho^0\gamma$)	-1 σ	—	—	0.013	—	—	—	0.003	5.42
ϵ^{MC} ($\omega\gamma$)	+1 σ	—	—	—	—	-0.006	—	-0.002	5.43
ϵ^{MC} ($\omega\gamma$)	-1 σ	—	—	—	—	0.006	—	0.004	5.43
ξ_{ARGUS} ($\omega\gamma$)	$\rightarrow 0$	—	—	—	—	-0.084	2.21	-0.037	5.22
Total	pos.	+0.09		+0.07		+0.05		+0.10	
	neg.	-0.08		-0.06		-0.10		-0.09	

Table 4.10: Significance calculations.

Method	$\rho^-\gamma$	$\rho^0\gamma$	$\omega\gamma$	sim.	ratio
No systematics	1.6	5.2	2.6	5.4	5.4
Lowest method	1.5	5.2	2.2	5.2	
All-changed method	1.3	5.1	2.2	4.8	
Subtraction method	1.4	5.2	2.2	5.2	
Inflation method	1.4	5.0	2.0	4.9	5.0
Convolution method	1.6	5.2	2.3	5.0	5.1

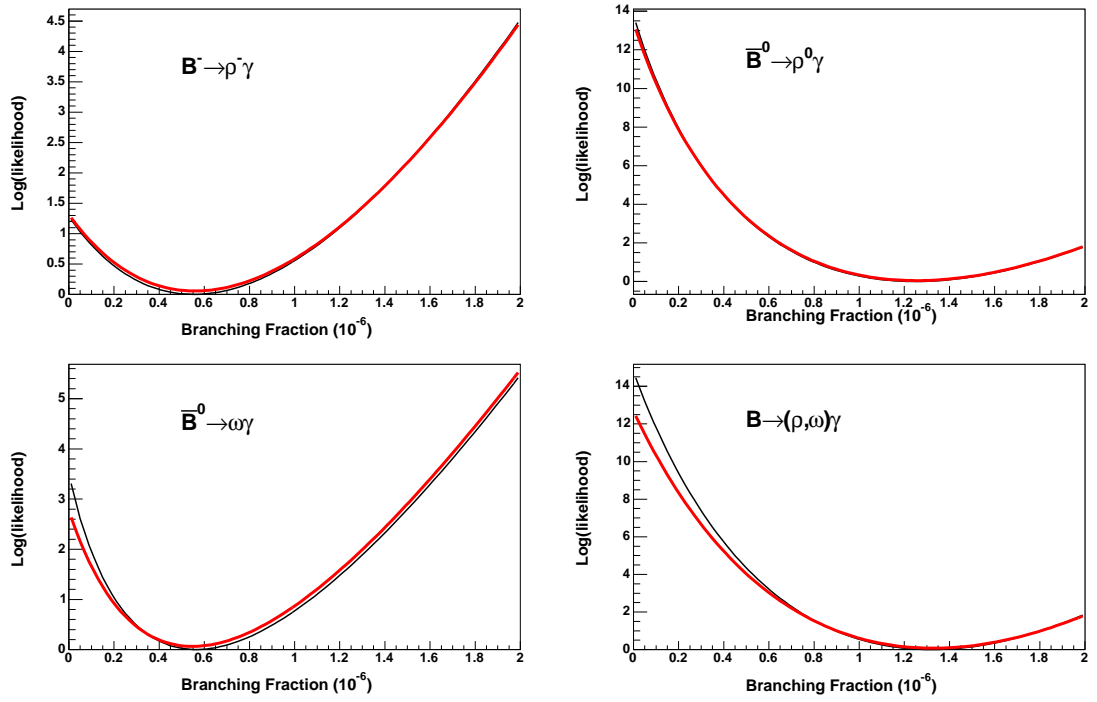


Figure 4.6: Likelihood distribution before (black-thin) and after (red-thick) convolution.

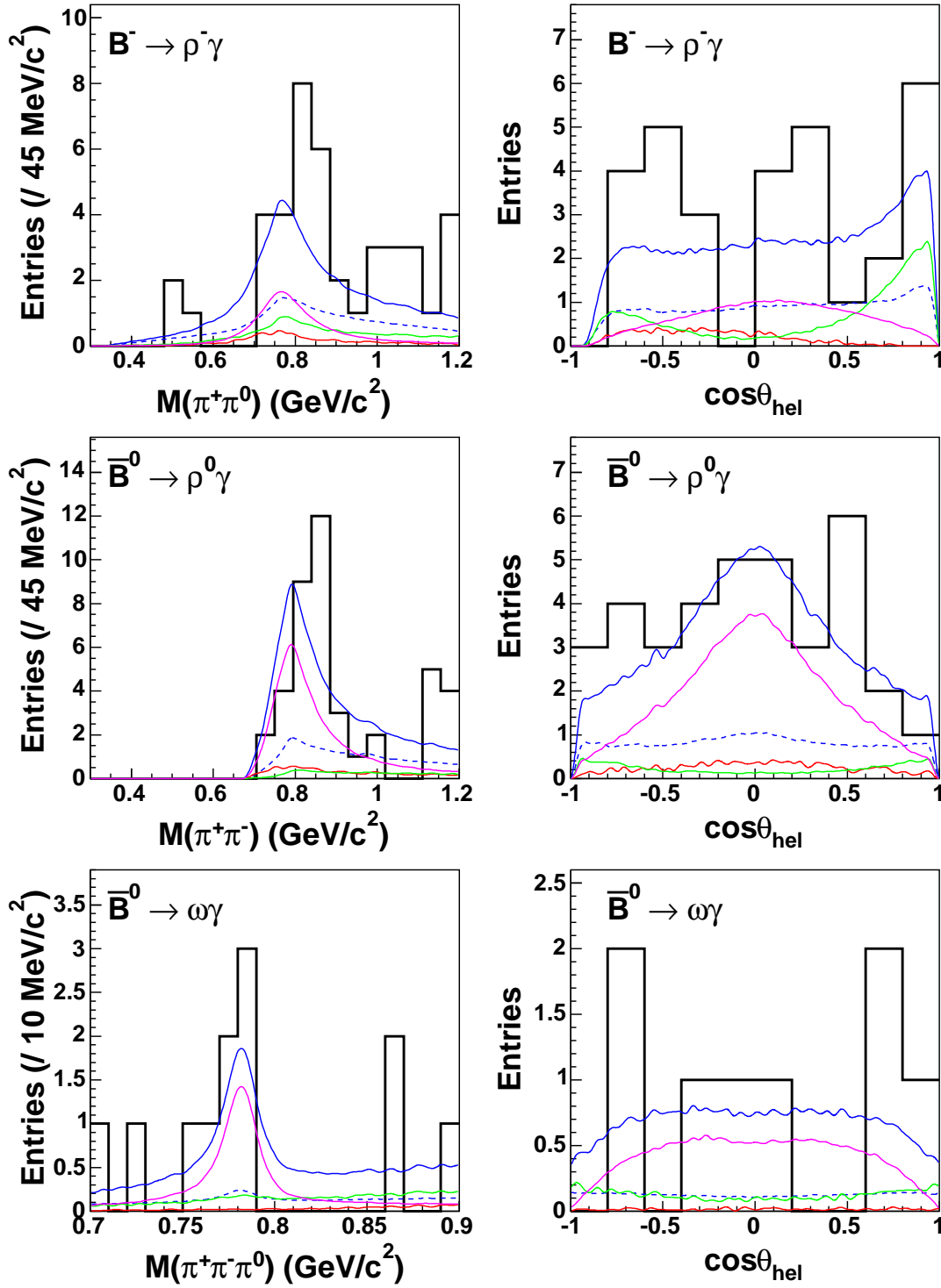


Figure 4.7: Mass and helicity angle distributions for the individual fit results to the $B^- \rightarrow \rho^- \gamma$, $\bar{B}^0 \rightarrow \rho^0 \gamma$ and $\bar{B}^0 \rightarrow \omega \gamma$ modes.

Chapter 5

Physics Results and Conclusion

5.1 Extraction of $|V_{td}/V_{ts}|$

We extract $|V_{td}/V_{ts}|$ using the prescription given in Ref. [8],

$$\frac{\mathcal{B}(\overline{B} \rightarrow (\rho, \omega)\gamma)}{\mathcal{B}(\overline{B} \rightarrow \overline{K}^*\gamma)} = \left| \frac{V_{td}}{V_{ts}} \right|^2 \frac{(1 - m_{(\rho, \omega)}^2/m_B^2)^3}{(1 - m_{K^*}^2/m_B^2)^3} \zeta^2 [1 + \Delta R] \quad (5.1)$$

or, inverting this,

$$\left| \frac{V_{td}}{V_{ts}} \right| = \sqrt{\frac{\mathcal{B}(\overline{B} \rightarrow (\rho, \omega)\gamma)}{\mathcal{B}(\overline{B} \rightarrow \overline{K}^*\gamma)} \frac{(1 - m_{K^*}^2/m_B^2)^{3/2}}{(1 - m_{(\rho, \omega)}^2/m_B^2)^{3/2}} \frac{1}{\zeta \sqrt{1 + \Delta R}}}. \quad (5.2)$$

where $\zeta = 0.85 \pm 0.10$ is the theoretical form factor ratio between $B \rightarrow (\rho, \omega)$ and $B \rightarrow K^*$, and $\Delta R = 0.1 \pm 0.1$ is the isospin violation factor.

The measured ratio of the branching fractions is taken from Eq. 4.17. The statistical and systematic errors are added in quadrature (denoted here as the experimental error) and assumed to follow an asymmetric Gaussian distribution. The theory parameters ζ and ΔR are assumed to follow a flat distribution.

The experimental and theoretical errors of $|V_{td}/V_{ts}|$ are calculated by a toy MC study in which the experimental ratio and theoretical parameters are randomly generated according

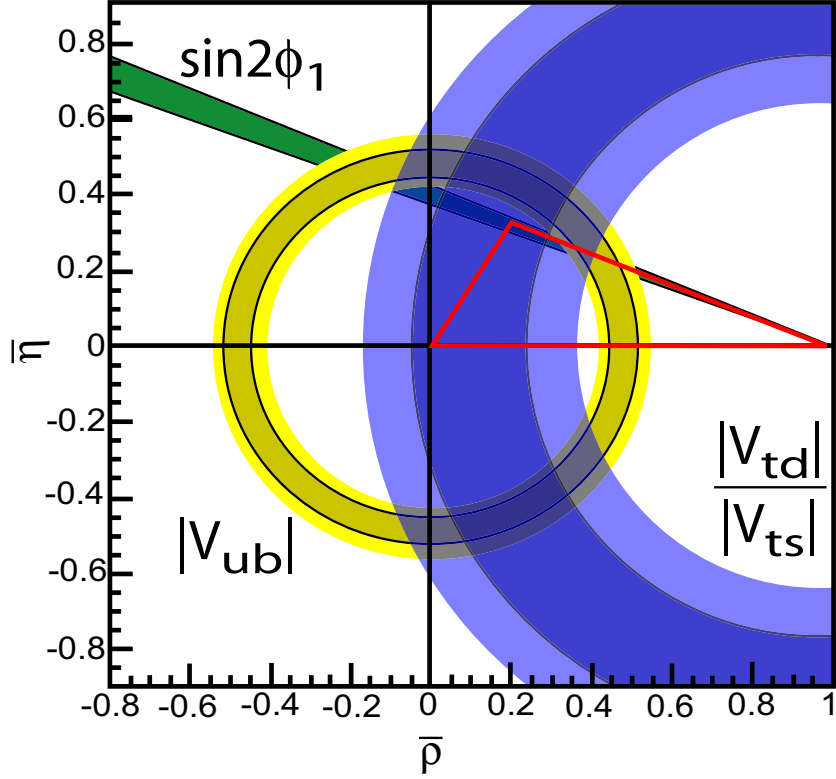


Figure 5.1: $\pm 1\sigma$ (inner contour) and 95% Confidence level (outer contour) limits on $\bar{\rho}$ and $\bar{\eta}$ from $\sin 2\phi_1$ (wedge), V_{ub} (circle centered on origin) and V_{td}/V_{ts} (circle centered off origin).

to their distribution. The $\pm 1\sigma$ (95% confidence level) interval on the extended $|V_{td}/V_{ts}|$ is taken as the range between the 16% and 84% (or 2.5% and 97.5%) of the integrated area of the $|V_{td}/V_{ts}|$ probability distribution.

The results are

$$|V_{td}/V_{ts}| = 0.199^{+0.026}_{-0.024}(\text{exp.})^{+0.018}_{-0.015}(\text{theo.}), \quad (5.3)$$

$$0.142 < |V_{td}/V_{ts}| < 0.259 \quad (95\% \text{ CL interval}). \quad (5.4)$$

For completeness, the fit results for the separate ratios from Eqs. 4.18 and 4.19 give

following values:

$$B^- \rightarrow \rho^- \gamma / B^- \rightarrow K^{*-} \gamma : |V_{td}/V_{ts}| = 0.133_{-0.047}^{+0.045}(\text{exp.})_{-0.010}^{+0.012}(\text{theo.}), \quad (5.5)$$

$$\bar{B}^0 \rightarrow \rho^0 \gamma / \bar{B}^0 \rightarrow \bar{K}^{*0} \gamma : |V_{td}/V_{ts}| = 0.400_{-0.054}^{+0.059}(\text{exp.})_{-0.030}^{+0.035}(\text{theo.}). \quad (5.6)$$

5.2 Conclusion

In conclusion, We observe the process $b \rightarrow d\gamma$ using the $B \rightarrow \rho\gamma$ and $\omega\gamma$ modes. The resulting branching fractions are consistent with SM predictions [8, 10, 11]. The ratio of the $\bar{B} \rightarrow (\rho, \omega)\gamma$ branching fraction to that for $\bar{B} \rightarrow \bar{K}^*\gamma$ is used to determine $|V_{td}/V_{ts}|$.

Appendix A

Isospin Violation

The isospin relation Eq. 4.3 (p. 73), which we assume in the simultaneous fit, is not an exact relation and is expected to be violated. The amount of the predicted isospin asymmetry between $B^- \rightarrow \rho^- \gamma$ and $\bar{B}^0 \rightarrow \rho^0 \gamma$ is $|\Delta_{-0}| < 0.1$ where $\Delta_{-0} \equiv \Gamma(B^- \rightarrow \rho^- \gamma) / [2\Gamma(\bar{B}^0 \rightarrow \rho^0 \gamma)] - 1$ and is far smaller than the current statistical sensitivities. The other isospin relation, $\Gamma(\bar{B}^0 \rightarrow \rho^0 \gamma) = \Gamma(\bar{B}^0 \rightarrow \omega \gamma)$ is more controversial and not much appears in the literature, but it is still a valid assumption according to private communications with theorists when the measurement error is $\mathcal{O}(30\%)$ or more.

A.0.1 Significance of the Isospin Violation

We parametrize the isospin violation effect with two variables β and γ :

$$(1 - \beta)[\Gamma(\bar{B}^0 \rightarrow \rho^0 \gamma) + \Gamma(\bar{B}^0 \rightarrow \omega \gamma)] = (1 + \beta)\Gamma(B^- \rightarrow \rho^- \gamma) \quad (\text{A.1})$$

$$(1 - \gamma)\Gamma(\bar{B}^0 \rightarrow \rho^0 \gamma) = (1 + \gamma)\Gamma(\bar{B}^0 \rightarrow \omega \gamma) \quad (\text{A.2})$$

where the nominal values from the isospin relation are $\beta = \gamma = 0$.

When the two parameters are allowed to float separately, we obtain the following results:

$$\begin{aligned}\beta &= 0.57^{+0.26}_{-0.25} & (2.3\sigma) \\ \gamma &= 0.45^{+0.27}_{-0.29} & (1.5\sigma)\end{aligned}\tag{A.3}$$

where the significance is calculated from the square root of the twice the difference of the log-likelihoods between the fit with the nominal value and the best fit. When both parameters are allowed to float, we obtain

$$\beta = 0.56^{+0.26}_{-0.25}, \quad \gamma = 0.36^{+0.25}_{-0.26} \quad (2.7\sigma).\tag{A.4}$$

Although both parameters are away from the nominal values by more than 1σ , we cannot claim there is an isospin violating effect, either, with less than 3σ significance.

A.0.2 Probability of the Isospin Violation from Toy MC Study

We have generated 10^7 sets of toy MC samples to estimate the probability of getting the isospin relations $\beta = 0.56$ and $\gamma = 0.36$ when the isospin relation perfectly holds and the true values are $\beta = \gamma = 0$.

Each toy MC set consists of three event samples for three $\bar{B} \rightarrow (\rho, \omega)\gamma$ modes. Each sample consists of the signal events, continuum events and five B decay background ($K^*\gamma$, $X_s\gamma$, $V\pi^0$, $V\eta$ and other rare B) events. The M_{bc} and ΔE values are generated to follow the modelled distribution from a random number; the number of events in each set is also a random number that follows a Poisson distribution whose mean is the number of events (for signal) calculated from the simultaneous fit result with the isospin relation, or (for continuum) obtained from or (for other backgrounds) assumed in the individual fit for the three modes.

For each set of samples, three individual fits are performed and the values of β and γ are calculated. These results are filled into a 120×120 meshed 2-dimensional histogram over

$(\pm 3.0) \times (\pm 3.0)$ space. The bin for the given β, γ has 1268 entries. The sum of the entries for the bins that have less number of entries divided by the total entries is $0.0487^{+0.0016}_{-0.0010}$, which corresponds to the probability of obtaining the observed values for the given assumption. In terms of σ , the result is 2.0σ away from the assumed value of $(0, 0)$. The contours of equal probability lines are drawn in Fig. A.3. We note that this probability (2.0σ) is somewhat different from the significance of the isospin violation from the fit (2.7σ).

A.0.3 Possible Bias in the Fitting Code

We have generated one thousand sets of similar toy MC samples of M_{bc} and ΔE values to test the fitting program. Each set consists of five event samples for two $\bar{B} \rightarrow \bar{K}^*\gamma$ modes and three $\bar{B} \rightarrow (\rho, \omega)\gamma$ modes. The components of the $\bar{B} \rightarrow (\rho, \omega)\gamma$ samples are the same; each $\bar{B} \rightarrow \bar{K}^*\gamma$ sample consists of the signal events, continuum events and other rare B background events.

By performing the fit to the 1000 sets of three $\bar{B} \rightarrow (\rho, \omega)\gamma$ modes, we find the mean of the individual fit results and the mean of their errors are more or less consistent with the input. Strictly speaking, we have to compare the asymmetric errors from time-consuming MINOS, which we did not attempt. We also try to perform the simultaneous fit to five modes with two 1000 sets of $\bar{B} \rightarrow \bar{K}^*\gamma$, expecting the results have the mean value which is consistent with the simultaneous fit result for data. However, what we obtained was significantly smaller combined branching fraction. The toy MC results are given in Table A.1, and their plots are given in Fig. A.1.

In order to understand the significant deviation in the simultaneous fit, we perform two more tests. The first test is to generate events according to the simultaneous fit result with the isospin relation to calculate the number of mean events for each mode. The result is given with the label “with isospin” in Table A.1. The mean branching fraction may still be

smaller, but not as significantly as the original test. The second test is to select the toy MC samples whose individual fit results match the input within 0.5 to 1% precision. We select 132 of such sets out of 8000 to perform the simultaneous fit. We find the results distribute with the mean of $(1.274 \pm 0.003) \times 10^{-6}$ and width of $(0.039 \pm 0.002) \times 10^{-6}$ (Fig. A.2). The mean is again smaller than the measured simultaneous fit value, which corresponds to 1.4σ higher than the mean where σ is the Gaussian width of the distribution. We conclude that the simultaneous fit result is a result of an upward fluctuation by 1.4σ for the given individual fit results, or some of the individual fit results may be downward fluctuated. The amount of the fluctuation (1.4σ) is within a reasonable range.

Table A.1: Summary of the toy MC results.

mode	input \mathcal{B} ($\times 10^{-6}$)	mean \mathcal{B} ($\times 10^{-6}$)	mean error ($\times 10^{-6}$)
$B^- \rightarrow \rho^- \gamma$	$0.55^{+0.42}_{-0.36}$	0.585 ± 0.011 (1.5σ)	0.362 ± 0.002
$\bar{B}^0 \rightarrow \rho^0 \gamma$	$1.25^{+0.37}_{-0.33}$	1.235 ± 0.012 (-0.5σ)	0.357 ± 0.001
$\bar{B}^0 \rightarrow \omega \gamma$	$0.56^{+0.34}_{-0.27}$	0.566 ± 0.011 (-1.4σ)	0.314 ± 0.002
$\bar{B} \rightarrow (\rho, \omega) \gamma$	$1.32^{+0.34}_{-0.31}$	1.269 ± 0.010 (-6.0σ)	0.317 ± 0.001
(with isospin)	$1.32^{+0.34}_{-0.31}$	1.302 ± 0.010 (-2.6σ)	0.319 ± 0.001

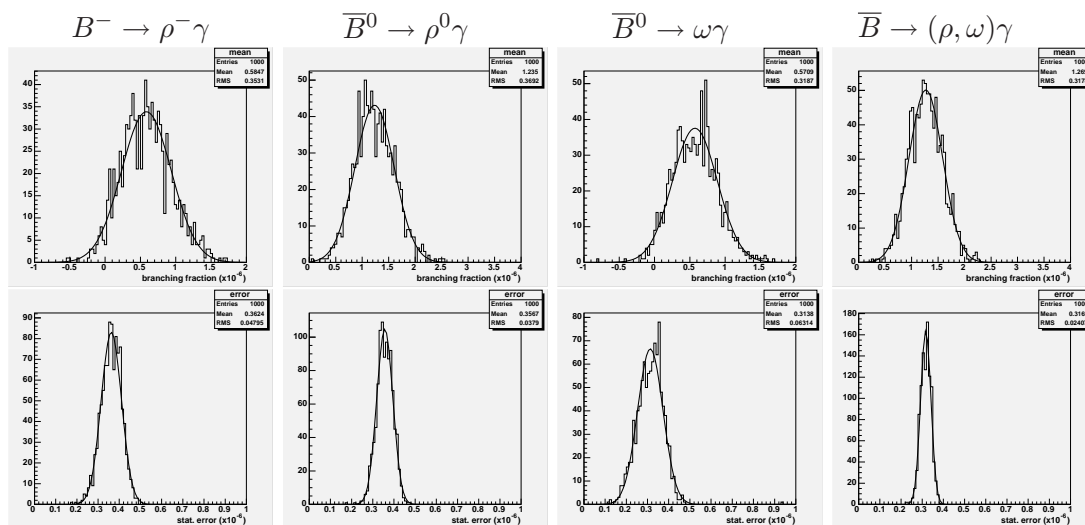


Figure A.1: Toy MC distribution of the fit results for the branching fraction (upper) and error (lower).

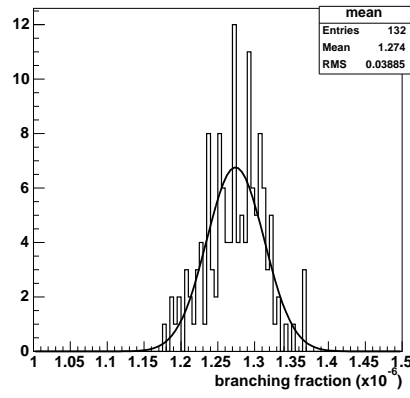


Figure A.2: Toy MC distribution of the simultaneous fit results for the samples selected from the individual fit results.

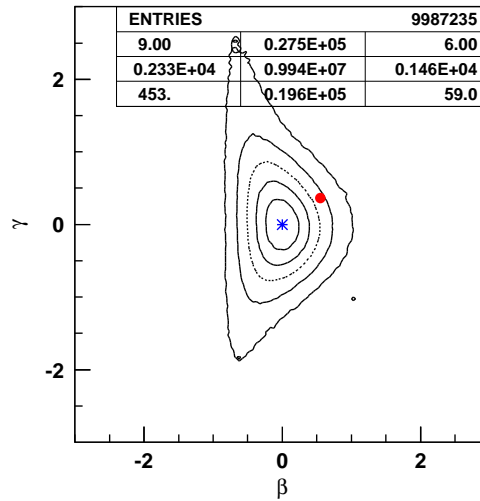


Figure A.3: Contours of equal probability points that are away from the nominal value (0, 0) by 0.5, 1, 1.5, 2 and 2.5 σ . Note that the PAW contour of 2 σ does not somehow directly go through the measured (β, γ) point (red point).

Bibliography

- [1] M. Kobayashi and T. Maskawa, Prog. Theor. Phys. **49**, 652 (1973); N. Cabibbo, Phys. Rev. Lett. **10**, 531 (1963).
- [2] L. Wolfenstein, Phys. Rev. Lett. **51**, 1945 (1983).
- [3] Particle Data Group, S. Eidelman *et al.*, Phys. Lett. B **592**, 1 (2004).
- [4] Belle Collaboration, D. Mohapatra *et al.*, Phys. Rev. Lett. **96**, 221601 (2006).
- [5] Belle Collaboration, D. Mohapatra *et al.*, Phys. Rev. D **72**, 011101 (2005).
- [6] BaBar Collaboration, B. Aubert *et al.*, Phys. Rev. Lett. **94**, 011801 (2005).
- [7] A. Ali, V. M. Braun and H. Simma, Z. Phys. C **63**, 437 (1994).
- [8] A. Ali and A. Parkhomenko, Eur. Phys. J. C **23**, 89 (2002).
- [9] A. Ali, E. Lunghi, A. Ya. Parkhomenko, Phys. Lett. B **595**, 323 (2004).
- [10] C.-D. Lu, M. Matsumori, A. I. Sanda and M.-Z. Yang, Phys. Rev. D **72**, 094005 (2005).
- [11] S. Bosch and G. Buchalla, Nucl. Phys. B **621**, 459 (2002).

- [12] T. Huang, Z. Li and H. Zhang, *J. Phys. G* **25**, 1179 (1999).
- [13] R. Fleischer and S. Recksiegel, *Phys. Rev. D* **71**, 051501 (2005).
- [14] For example, A. Arhrib, C.-K. Chua and W.-S. Hou, *Eur. Phys. J. C* **21**, 567 (2001);
A. Ali and E. Lunghi, *Eur. Phys. J. C* **26**, 195 (2002); Z.-J. Xiao and C. Zhuang, *Eur. Phys. J. C* **33**, 349 (2004).
- [15] S. Kurokawa and E. Kikutani, *Nucl. Instrum. Meth. A* **499**, 1 (2003); KEK B-Factory Design Report KEK-Report-95-7 (1995) (unpublished).
- [16] Belle Collaboration, A. Abashian *et al.*, *Nucl. Instrum. Meth. A* **479**, 117 (2002).
- [17] <http://www.lns.cornell.edu/public/CESR/>
- [18] DORIS (Doppel-Ring-Speicher, "double-ring storage") was DESY's second circular accelerator.
- [19] <http://lns.cornell.edu/public/CLEO/>; CLEO Collaboration, J. P. Alexander *et al.*, *Phys. Rev. Lett.* **86**, 2001 (2737-2741)
- [20] DELPHI Collaboration, V. Chabaud *et al.*, The DELPHI silicon strip microvertex detector with double sided readout, *Nucl. Instrum. Meth. A* **368**, 1996 (314332).
- [21] O. Toker, S. Masciocchi, E. Nygard, A. Rudge, and P. Weilhammer, VIKING: A CMOS low noise monolithic 128-channel front end for Si strip detector readout, *NIMA* **340**, 1994 (572579).
- [22] The VA1TA Chip. <http://www.ideas.no/> User Manual.
- [23] Belle Collaboration, M. e. a. Yokoyama, Radiation Hardness of VA1 with Submicron Process Technology, *IEEE Trans. Nucl. Sci.* Vol. 48 (2001) 440443.

- [24] R. Abe *et al.*, Status of the Belle SVD detector, Nucl. Instrum. Meth. A **478**, 2002 (296298); T. Kawasaki, The Belle silicon vertex detector, Nucl. Instrum. Meth. A **494**, 2002 (94101); BELLE Collaboration, G. Alimonti *et al.*, The BELLE silicon vertex detector, Nucl. Instrum. Meth. A **453**, 2000 (7177); M. Hazumi, Performance of the Belle silicon vertex detector, Nucl. Instrum. Meth. A **473**, 2001 (16).
- [25] Y. Ushiroda, Nucl. Instrum. Meth. A **511**, 6 (2003).
- [26] H. Hirano *et al.*, A high resolution cylindrical drift chamber for the KEK B- factory, Nucl. Instrum. Meth. A **455**, 2000 (294304).
- [27] T. Iijima *et al.*, Aerogel Cherenkov counter for the BELLE detector, Nucl. Instrum. Meth. A **453**, 2000 (321325); T. Iijima *et al.*, Aerogel Cerenkov counter for the BELLE experiment, Nucl. Instrum. Meth. A **379**, 1996 (457459).
- [28] H. Kichimi *et al.*, The BELLE TOF system, Nucl. Instrum. Meth. A **453**, 2000 (315320).
- [29] H. Ikeda *et al.*, A detailed test of the CsI(Tl) calorimeter for BELLE with photon beams of energy between 20-MeV and 5.4-GeV, Nucl. Instrum. Meth. A **441**, 2000 (401426).
- [30] Belle Collaboration, V. Zhilich, Online Luminosity Measurements with CSI Calorimeter at the Belle Detector, Belle Note 465 (2001). Belle internal paper.
- [31] Y. Ushiroda *et al.*, Development of the central trigger system for the BELLE detector at the KEK B-factory, Nucl. Instrum. Meth. A **438**, 1999 (460471)

- [32] BELLE Collaboration, M. Nakao, M. Yamauchi, S. Y. Suzuki, R. Itoh, and H. Fujii, Data acquisition system for the BELLE experiment, *IEEE Trans. Nucl. Sci.* 47 (2000) 5660.
- [33] M. Tomoto *et al.*, Z-trigger system with the BELLE central drift chamber, *Nucl. Instrum. Meth. A* **447**, 2000 (416423).
- [34] Belle Collaboration, S. e. a. Nishida, Trigger efficiency, Belle Notes 350, 381, 423, 459, 504, 520, 548, 584 (2000-2002). Belle internal paper.
- [35] S. Nishida, Radiative B decays into K pi gamma and K pi pi Final States,. PhD Thesis 2004/3.
- [36] Belle Collaboration, K. H. et al., Level 4 Software Trigger at Belle, Belle Note 299 (2000).
- [37] T. Sjostrand, High-energy physics event generation with PYTHIA 5.7 and JETSET 7.4, *Comput. Phys. Commun.* 82 (1994) 7490; T. Sjostrand, PYTHIA 5.7 and JETSET 7.4: Physics and manual, hep-ph/9508391.
- [38] B. Andersson, G. Gustafson, G. Ingelman, and T. Sjostrand, PARTON FRAGMENTATION AND STRING DYNAMICS, *Phys. Rept.* 97 (1983) 31.
- [39] <http://www.lns.cornell.edu/public/CLEO/soft/QQ/>
- [40] <http://www.slac.stanford.edu/lange/EvtGen/>
- [41] R. Brun et al., GEANT 3.21, CERN Report No. DD/EE/84-1 , 1987
- [42] <http://belle.kek.jp/secured/nbb/nbb.html>
- [43] R. A. Fisher, *Annals of Eugenics* **7**, 179 (1936)

- [44] G. C. Fox and S. Wolfram, Phys. Rev. Lett. **41**, 1581 (1978)
- [45] H. Kakuno *et al.*, Nucl. Instrum. Meth. A **533**, 516 (2004)
- [46] R. Enomoto, Belle lecture series (1999)
- [47] ARGUS Collaboration, H. Albrecht *et al.*, Phys. Lett. B **241**, 278 (1990)
- [48] Crystal Ball Collaboration, J. E. Gaiser *et al.*, Phys. Rev. D **34**, 711 (1986); T. Skwarnicki, Ph.D. Thesis, Institute for Nuclear Physics, Krakow 1986; DESY Internal Report, DESY F31-86-02 (1986)
- [49] <http://root.cern.ch/>
- [50] <http://roofit.sourceforge.net/>
- [51] <http://wwwasdoc.web.cern.ch/wwwasdoc/minuit/minmain.html>
- [52] Heavy Flavor Averaging Group, winter 2005 results, (<http://www.slac.stanford.edu/xorg/hfag/>).
- [53] Belle Collaboration, M. Nakao *et al.*, Phys. Rev. D **69**, 112001 (2004)
- [54] Belle Collaboration, J. Drajic, T. Gershon, *et al.*, Phys. Rev. Lett. **93**, 131802 (2004)
- [55] Belle Collaboration, J. Zhang *et al.*, Phys. Rev. Lett. **94**, 031801 (2005)
- [56] Belle Collaboration, S.H. Lee *et al.*, Phys. Rev. Lett. **91**, 261801 (2003).
- [57] P. Koppenburg, Belle Note 665, "An improved π^0 and η veto"
- [58] P. Koppenburg, Belle Note 621, "A Measurement of the Track Finding Efficiency Using Partially Reconstructed D^* Decays," (2003)

- [59] H-W. Kim, Belle Note 499, “Study of High Energy Photon Detection Efficiency Using Radiative Bhabha,” (2002)
- [60] S. W. Lin, P. Chang and H. C. Hwang, Belle Note 645, “Update of π^0 Systematics Using Inclusive η (78/fb),” (2003)